AD-A137 903 KINEMATIC AND DYNAMIC ANALYSIS OF HIGH-SPEED INTERMITTENT-MOTION MECHANIS..(U) RUTGERS - THE STATE UNIV PISCATAWAY NJ DEPT OF MECHANICAL AND.. T W LEE

UNCLASSIFIED 16 JAN 84 ARO-17731.3-EG DAAG29-81-K-0016 F/G 20/11 NL

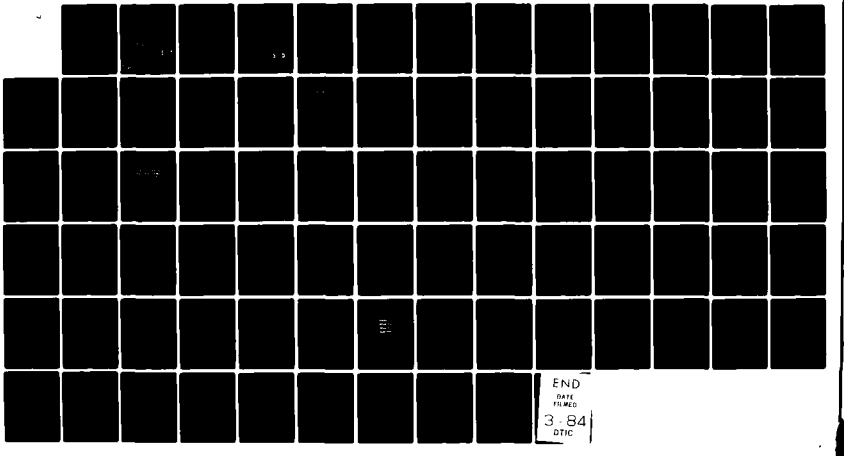

END
DATE FILMED
3-84
DTIC

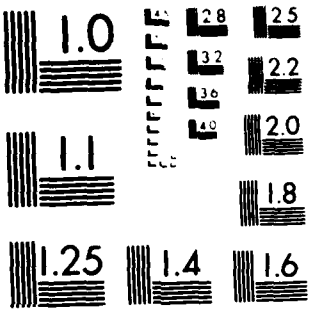

ARO 17731.3-EG

(2)

# KINEMATIC AND DYNAMIC ANALYSIS OF HIGH-SPEED INTERMITTENT-MOTION MECHANISMS

Final Report

Ting W. Lee

January 16, 1984

U.S. Army Research Office

Contract Number

DAAG29-81-K-0016

Mechanical & Aerospace Engineering
Rutgers University
P.O. Box 909, Piscataway, NJ 08854



84 02 14 140

SECURITY CLASSIFICATION OF THIS PAGE (When Data Entered)

| REPORT DOCUMENTATION PAGE | | READ INSTRUCTIONS BEFORE COMPLETING FORM |
|---|---|---|
| 1. REPORT NUMBER | 2. GOVT ACCESSION NO. AD-A137903 | 3. RECIPIENT'S CATALOG NUMBER |
| 4. TITLE (and Subtitle) Kinematic and Dynamic Analysis of High-Speed Intermittent-Motion Mechanisms | | 5. TYPE OF REPORT & PERIOD COVERED Final Report 12/1/80 - ~~11/30/83~~ |
| | | 6. PERFORMING ORG. REPORT NUMBER |
| 7. AUTHOR(s) Ting W. Lee | | 8. CONTRACT OR GRANT NUMBER(s) DAAG 29-81-K-0016 |
| 9. PERFORMING ORGANIZATION NAME AND ADDRESS Department of Mechanical & Aerospace Engineering, Rutgers University P.O. Box 909, Piscata Way, NJ 08854 | | 10. PROGRAM ELEMENT, PROJECT, TASK AREA & WORK UNIT NUMBERS |
| 11. CONTROLLING OFFICE NAME AND ADDRESS U. S. Army Research Office Post Office Box 12211 Research Triangle Park, NC 27709 | | 12. REPORT DATE January 16, 1984 |
| | | 13. NUMBER OF PAGES 76 |
| 14. MONITORING AGENCY NAME & ADDRESS(if different from Controlling Office) | | 15. SECURITY CLASS. (of this report) Unclassified |
| | | 15a. DECLASSIFICATION/DOWNGRADING SCHEDULE |

16. DISTRIBUTION STATEMENT (of this Report)

Approved for public release; distribution unlimited.

17. DISTRIBUTION STATEMENT (of the abstract entered in Block 20, if different from Report)

NA

18. SUPPLEMENTARY NOTES

THE VIEW, OPINIONS, AND OR FINDINGS CONTAINED IN THIS REPORT ARE THOSE OF THE AUTHOR(S) AND SHOULD NOT BE CONSTRUED AS AN OFFICIAL DEPARTMENT OF THE ARMY POSITION, POLICY, OR DECISION, UNLESS SO DESIGNATED BY OTHER DOCUMENTATION.

19. KEY WORDS (Continue on reverse side if necessary and identify by block number)

Kinematics
Kinematics and Dynamics of Mechanisms
Macnine Design
Computer-Aided Design (CAD)

20. ABSTRACT (Continue on reverse side if necessary and identify by block number)

This research concerns the development of theory and computational procedures for the kinematic and dynamic analyses of high-speed intermittent-motion mechanisms. In particular, it applies recent advances in kinematics, utilizing fundamental models of dynamics, coupled with experimental observations in order to develop methods capable of predicting the performance as well as motion characteristics of certain basic intermittent-motion mechanisms which are useful in industry and military

DD FORM 1 JAN 73 1473 EDITION OF 1 NOV 65 IS OBSOLETE

UNCLASSIFIED

SECURITY CLASSIFICATION OF THIS PAGE (When Data Entered)

applications. These methods have been applied to a selected group of mechanisms, such as Geneva, ratchets and escapements. This research has two parts. The analytical part involves: the investigation of the kinematic and dynamic performance characteristics of these selected mechanisms; the formulation of a dynamic model of impact; the determination of the dynamic response of this model under various operating conditions; and finally, the development of unit computational programs for analyzing the kinematic characteristics and dynamic response of these intermittent-motion mechanisms. The experimental part of the research involves measurements of the kinematic and dynamic response, and stresses of high-speed external Geneva mechanisms. The purpose of the measurements is to correlate with analysis and to verify the results of theoretical findings.

The theory developed in the high-speed intermittent-motion mechanisms has been extended to two related areas of mechanism design problems: namely, the momentary-dwell type of intermittent-motion mechanisms which have potential application to the high-speed automatic weapon system; and an investigation on the workspace of a robotic manipulator system.

The problems of this investigation belong to a selected group of unsolved or partially solved problems which are relevant and useful in industry as well as military applications. The results of this basic research, it is believed, will represent a significant contribution to the design of high-speed machinery and automated manufacturing systems.

TABLE OF CONTENTS

## 1. A Statement of the Problem Studied

The main objective of this research is to apply recent advances in kinematics, utilizing fundamental models of dynamics, coupled with experimental observations in order to develop methods capable of predicting the performance as well as motion characteristics of certain basic, finite-dwell type of intermittent-motion mechanisms including Geneva mechanisms, ratchets and escapements, which are useful in industry and military applications.

The contract was originally awarded for a two-year period. Later, it was awarded an additional year to extend the theory developed earlier under this contract to two related areas of mechanism design problems, namely, the momentary-dwell type of intermittent-motion mechanisms and an investigation on the workspace of a robotic manipulator system.

## 2. A Summary of Significant Accomplishment

As it was mentioned in the preceeding paragraph, the project involves an investigation of the dynamic as well as the kinematic characteristics of mechanisms of the following three types:

- Intermittent-motion mechanisms of the finite-dwell type
- Intermittent-motion mechanisms of the momentary-dwell type
- Robotic Manipulators

Results obtained from this project, which are believed to be new and significant pertaining to the above three catagories, are described next.

### (a) Kinematic and Dynamic Analysis of Intermittent-Motion Mechanisms of the Finite-Dwell type

A mathematical model of impact has been formulated for the intermittent-motion mechanism. The model, which includes clearance, damping, mechanism elasticity and material compliance is basic to the determination of the dynamical response such as force amplification, dynamic load and the stresses of mechanisms with intermittent-motion.

The theoretical model developed has been applied to several practical mechanisms, the Geneva mechanism, the ratchet and the escapement mechanism. These are popular indexing devices and have been widely used in many production machinery and automatic weapon systems. A computational procedure incorporating the dynamic model with the finite-element approach is developed for the Geneva mechanism. Dynamic load can be calculated and is subsequently used for the estimate of stresses. An automatic mesh generator for finite-element approach is presented for the Geneva wheel, although not simple, due to the complicated geometry of the wheel. The computer-aided procedure makes possible, for the first time, to accurately predict the performance as well as durability of an intermittent-motion mechanism with respect to its oprational speed.

In the theoretical development, a new approach in the modeling of system damping is presented. Instead of using damping ratio, which is difficult to estimate accurately, a new damping function is introduced, which characterizes the speed and load dependent nature of damping. Two types of damping functions are proposed and both of their corresponding damping forces satisfy the expected hysteresis boundary conditions. A comparative study of the present model with conventional dynamic models is performed. It demonstrates the characteristics of the proposed model and its usefulness for the study of the dynamics of intermittent-motion mechanism.

Experimental data on stresses of the Geneva mechanism under both dynamic and static loadings have been obtained using MTS machine on a 4.54" O.D. Geneva wheel (AISI 2340 Steel). Beam stresses at the tip and root are determined using strain gauges. The results check well with the theoretical prediction using finite-element methods.

The result of this part of the project has technological applications. Since most automatic weapon systems involve intermittent-motion mechanism as their main indexing device, the work represented here may be used to predict the dynamic response of the weapon system and, ultimately, used for a durability and life-cycle analysis of the system.

(b) Analysis and Synthesis of Intermittent-Motion Mechanisms of the Momentary-Dwell Type

A general approach for the kinematic synthesis of the momentary-dwell mechanism has been presented. The approach involves using the solution of first-order dwell criterion as an initial estimate and the development of a computer-aided procedure to subsequently readjust the mechanism proportions for a closer match to other dwell criteria by optimization. The proportions thus obtained provide an approximation of the high orders of dwell and, for most practical purposes, the solution is useful and acceptable. The approach has been illustrated by two examples, a six-bar linkage and a chain-and-coupler-link mechanism. These mechanisms are selected because they represent the general characteristics of most momentary-dwell mechanisms which are difficult to analyze and design. It has been shown in this investigation that on the design of these momentary-dwell mechanisms, analytical approach alone is not possible, and a joint consideration using a numerical optimization technique, therefore, becomes necessary.

(c) On the Kinematic Characteristics of Robotic Manipulators

This part of investigation concerns an analytical investigation of the kinematic characteristics of robotic manipulators. It includes two parts. The first part deals with the study of manipulators constructed with revolute joints in series and having open kinematic chain configuration. The second part treats the problem of a maneuverable platform mechanism with closed kinematic chain configuration.

In the first part, the kinematic relationship between consecutive revolute joints with both unlimited and limited rotatabilities are formulated, and subsequently, the manipulator workspace is analytically derived and represented by a set of recursive equations. Two of the basic characteristics on manipulator workspace, i.e., the existence of hole and void, are

investigated in great detail. Based on these theories, algorithms and computer program for quantitative evaluation of the volume of workspace and for outlining the boundary of the workspace are developed.

Furthermore, an important theorem on manipulator workspace is presented. It is found that for a given manipulator structure, the ratio of the volume of the workspace to the cube of its total link length is a constant. This theorem leads, therefore, to the introduction of an effective manipulator performance index. Based on this index, an algorithm on the optimization of manipulator workspace has been developed. It is shown that for a popular commercial robot configuration, an optimum structure can be found through both analytical and numerical means. An interesting comparative study with human arm proportions is also provided.

In the second part, the number synthesis of the n-SPS platform mechanism is first performed (S and P denote the spherical and prismatic joints, respectively). It is shown that the 6-SPS mechanism is the only platform structure which has six controllable degrees-of-freedom and can be used as a general manipulating device. Analytical formulation for the kinematic analysis, synthesis and control of the mechanism is presented. Cross-sections of the workspace on three primary planes are constructed. Consequently, several basic kinematic problems are investigated. These are: the analysis of a planar 4-bar with adjustable link lengths; the rotatability of a ball-and-socket joint; and the possible interference or locking phenomenon during the motion of the platform. An algorithm and a computer program to outline these cross-sections have been developed.

The results of this research, it is believed, have contributed toward a basic understanding of the kinematic characteristics and design of robotic manipulators.

## 3. A List of Publications and Technical Reports

### A. Journal Articles


*1. Yang, D.C.H. and Lee, T.W., "Optimization of Manipulator Workspace," Robotics Research and Advanced Applications, Ed. by W.J. Book, an ASME Publication, pp. 27-34, 1982.

*2. Lee, T.W. and Yang, D.C.H., "On the Evaluation of Manipulator Workspace," Journal of Mechanisms, Transmissions and Automation in Design, Trans. ASME, Vol. 105, No. 1, pp. 70-77, March 1983.

*3. Yang, D.C.H. and Lee, T.W., "On the Workspace of Mechanical Manipulators," Journal of Mechanisms, Transmissions and Automation in Design, Trans. ASME, Vol. 105, No. 1, pp. 62-69, March 1983.

*4. Yang, D.C.H., and Lee, T.W., "Feasibility Study of A Platform Type of Robotic Manipulators from A Kinematic Viewpoint," to appear in Journal of Mechanisms, Transmissions and Automation in Design, Trans. ASME, Vol. 106, No. 1, March 1984.

*5. Lee, T.W., "Automated Dynamic Analysis of Chain-Driven Mechanical Systems," Journal of Mechanisms, Transmissions and Automation in Design, Trans. ASME, Vol. 105, No. 3, pp. 362-370, September 1983.

*6. Lee, T.W. and Wang, A.C., "On the Dynamics of Intermittent-Motion Mechanisms, Part I: Dynamic Model and Response," Journal of Mechanisms, Transmissions and Automation in Design, Trans. ASME, Vol. 105, No. 3, pp. 534-540, September 1983.

*7. Wang, A.C. and Lee, T.W., "On the Dynamics of Intermittent-Motion Mechanisms, Part II: Geneva Mechanisms, Ratchets, and Escapements," Journal of Mechanisms, Transmissions and Automation in Design, Trans. ASME, Vol. 105, No. 3, pp. 541-551, September 1983.

B. Conference Articles

1. Lee, T.W., Wang, A.C. and Niederoest, G.R., "On the Dynamics and Stress Analysis of Intermittent-Motion Mechanisms," Transactions of the Twenty-Seventh Conference of Army Mathematicians, ARO Report 82-1, pp. 401-431, 1982.

2. Dahdough, F.D., Ma, C.H. and Lee, T.W., "Automated Dynamic Analysis of Cascaded Chain-Driven Mechanical Systems, - Chain Gun," Proceedings of the Third U.S. Army Symposium on Gun Dynamics, May 1982.

*3. Wang, A.C. and Lee, T.W., "On the Kinematic Synthesis of Dwell Mechanisms," Proceedings of the Sixth World Congress of the International Federation of Theory of Machines and Mechanisms, New Delhi, India, December 15-20, 1983, pp. 155-159.

---

Articles marked with an asterisk are included in the Appendices.

4. Scientific Personnel Supported By This Project And Degrees Awarded During This Reporting Period

A. Personnels

1. Dr. Ting W. Lee, Associate Professor, Project Director.

2. Dr. Albert C. Wang, worked on this project as research assistant on his doctoral dissertation.

3. Dr. D.C.H. Yang, worked on this project as his doctoral dissertation. He received no salary from this project.

4. Mr. Chin-Hsing Ma, worked on this project as his Master's degree dissertation. He received no salary from this project.

5. Mr. G.R. Niederoest, worked on this project as his Master's degree dissertation. He received no salary from this project.

6. Mr. Tyng Liu, a graduate student, worked on a problem associated with this project. He was partially supported by this project.

7. Mr. Martin Cwiakala, a graduate student, worked on a problem associated with this project. He received no salary from this project.

B. Dissertations

1. D.C.H. Yang: On the Kinematic Characteristics of Robotic Manipulators, 1982, Ph.D. Dissertation.

2. A.C. Wang: On the Kinematic and Dynamics of Intermittent-Motion Mechanisms, 1983, Ph.D. Dissertation.

3. Chin-Hsing Ma: Computer-Aided Dynamic Analysis of an Automatic Weapon System, 1981, Master's Degree Thesis.

4. G.R. Niederoest: Experimental Investigation and Finite-Element Analysis of Geneva Mechanisms, 1983, Master's Degree Thesis.

## APPENDIX A

### Articles Related to the Subject of High-Speed Intermittent-Motion Mechanisms

1. On the Dynamics of Intermittent-Motion Mechanisms, Part I: Dynamics Model and Response

2. On the Dynamics of Intermittent-Motion Mechanisms, Part II: Geneva Mechanisms, Ratchets, and Escapements

3. On the Kinematic Synthesis of Dwell Mechanisms

4. Automated Dynamic Analysis of Chain-Driven Mechanical Systems

# On The Dynamics of Intermittent-Motion Mechanisms

## Part I. Dynamic Model and Response

**Ting W. Lee**
Associate Professor
Mem. ASME

**A. C. Wang**
Research Assistant

Department of Mechanical and Aerospace Engineering
Rutgers University
New Brunswick, N.J. 08903

*This paper deals with a basic problem regarding intermittent-motion mechanisms, namely, how to formulate a predicative model for the study of the dynamics of these mechanisms. A mathematical model is developed in this investigation. The model, which includes clearance, damping, material compliance, and mechanism elasticity, is basic to the determination of the dynamical response such as force amplification and motion characteristics of mechanisms with intermittent motion. A new approach in the modeling of system damping is presented. Instead of using damping ratio, which is difficult to estimate accurately, a new damping function is introduced, which characterizes the speed and load dependent nature of damping. Two types of damping functions are proposed and both of their corresponding damping forces satisfy the expected hysteresis boundary conditions, i.e., zero damping force at zero and maximum displacement of contact. A comparative study of the present model with conventional dynamic models is performed. It demonstrates the characteristics and the usefulness of the proposed model for the study of the dynamics of intermittent-motion mechanisms.*

### 1 Introduction

Intermittent-motion mechanisms play an important role in modern technology and industry. They are the essential elements in many machinery and automatic weapon systems. A variety of intermittent-motion mechanisms have been described in the literature [1]. Basically, there are two types: One gives a finite dwell, such as the standard external Geneva mechanism [2], the other provides instantaneous or momentary dwell [3]. From the point of view of mechanism structure, intermittent-motion can be generated either from single or compound mechanisms. Geneva mechanisms, cam-follower systems, and linkage [4] are examples of the single type; compound Geneva mechanisms [5, 6] chained linkage [7], and geared linkages [3], belong to the compound intermittent-motion mechanisms.

Of particular interest and concern in this investigation is the study of the dynamics of high-speed intermittent-motion mechanisms of the finite-dwell and of the single type which are more difficult to analyze. There are many reasons attributing to this fact. First, the mechanism is characterized by inherent shock loading, that is, the presence of essentially discontinuous forces, masses, velocities and potential energies; and second, because of this special loading condition, as well as the inertia loading due to high speed operation, the effects of material compliance, mechanism elasticity, clearance and damping have to be taken into consideration. Damping which has an important role on the dynamics of the mechanism is especially difficult to model. It is generally known that damping depends upon load as well as speed. The conventional way of modeling requires an accurate estimate of the damping ratio which is difficult to attain. The problem is therefore complicated and needs special attention.

The purpose of this investigation is to develop methods capable of predicting the performance as well as the motion characteristics of certain basic mechanisms which generate intermittent-motion and are of general interest in practice. In particular, the objectives are: 1) to formulate an analytical model for a certain class of intermittent-motion mechanisms, and 2) to present a new damping function in the model, which characterizes system damping and which can be quantitatively estimated. The result of this investigation, it is hoped, will not only provide a predictive dynamic model and a computational package for the dynamics of intermittent-motion mechanisms, but also an added advantage - a deeper understanding of the dynamic load on intermittent-motion mechanisms and a physical insight to the dynamic characteristics of these mechanisms. Such an investigation is believed to be trustworthy, and to the authors' knowledge, has not been reported in the literature.

We begin by discussing the background of the dynamics of the intermittent-motion mechanism and its relationship with the well-investigated field of clearance in the mechanical joints. An analytical model suitable for intermittent-motion mechanisms is formulated and its solutions are derived. A comparative study of the proposed model, with the conventional dynamic models, is performed. The results, whenever possible, are illustrated by graphs which may offer

Contributed by the Mechanisms Committee and presented at the Design and Production Engineering Technical Conference, Washington, D.C., September 12-15, 1982, of THE AMERICAN SOCIETY OF MECHANICAL ENGINEERS. Manuscript received at ASME Headquarters, June 10, 1982. Paper No. 82-DET-64.

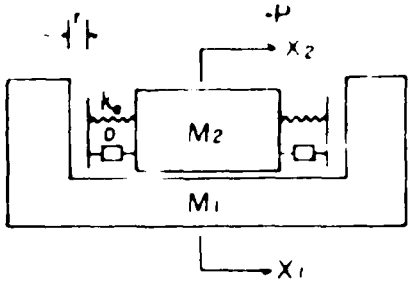


Fig. 1 The dynamic model for intermittent-motion mechanisms

some physical insight into the behavior of the intermittent-motion mechanism. Applications of the present model are extended to practical mechanisms such as Geneva mechanisms and ratchets, and the results are reported in Part II of this investigation. The result of this investigation, it is believed, will represent a contribution towards the more efficient and economical design and analysis of mechanical systems involving high-speed intermittent motion.

## 2 Mathematical Model

All intermittent-motion mechanisms share some common characteristics. First, there exists generally shock or impact loading which may be inherent in the mechanism, or as a result of external loading. In the dynamic analysis of the mechanisms, therefore, not only the kinematics but also the load and driving characteristics have to be taken into consideration. Secondly, clearance or backlash is unavoidable in any mechanical joint or connection which makes possible a loss of contact between the members. This may lead to subsequent impacts which would give rise to vibration. The study of the dynamic response of intermittent-motion mechanisms at high speed is therefore analogous to the investigation of the dynamics of mechanical systems with clearances – a field which has become important and active in the past decade.

Most of the investigations relating to mechanism clearance involve the formulation of mathematical models of impact as a basis of their study. Essentially simple systems of springs and dashpots with clearance are used to simulate the complex and nonlinear phenomena of mechanical connections. Some of the notable models were presented by Langer [8], Johnson [9], Kobrinskiy and Babitzky [10], Dubowsky and Freudenstein [11], Hunt and Crossley [12], Herbert and McWhannell [13], etc. A useful outline of the background to this field of investigation is given by Dubowsky and Gardner [14]. Recently Haines [15] gave a comprehensive review of the subject.

In this study a mathematical model has been formulated to investigate the dynamic response of the intermittent-motion mechanism. The physical model itself is basically taken from the one proposed by Dubowsky and Freudenstein [11] on their thoughtful study of clearance in the mechanical joints. The differences, however, lie on the mathematical modeling of the stiffness and damping of the system. These are mechanism elasticity and most importantly, a new approach which involves a damping function introduced in the modeling of system damping. Two types of damping functions are proposed and their corresponding damping forces both satisfy the expected hysteresis boundary conditions, i.e., zero damping force at zero and maximum relative displacement of contact.

The physical model used in this investigation is shown in Fig. 1. The constants $M_1$ and $M_2$ represent the equivalent masses of the driven and the driving elements, respectively. For instance, they may correspond to the Geneva wheel and pin on a Geneva mechanism. $K_c$ and $D$ represent the system stiffness and damping, respectively, and $c$ denotes the clearance. The external loading applied on the driving element is represented as $P$.

In this investigation the system stiffness, $K_c$, is modeled by two single springs in series. In addition to the surface compliance ($K_h$) which is included in Dubowsky's model [11], another spring represented by the mechanism elasticity ($K_m$) is considered. Following Dubowsky and Freudenstein [11], the surface compliance is modeled using the linearized expression of Hertz contact theory. For instance, in the case of a cylindrical pin contacting with a flat surface, we have the deflection,

$$\alpha = (K_1 + K_2)(P/a)\left[\ln \frac{8a^2b}{(K_1 + K_2)R_1} - \ln P\right], \quad 2 \tag{1}$$

where the subscripts 1 and 2 refer to the parameters associated with the elements 1 and 2, or the driven and driving members, respectively. Parameters $a$ and $b$ are the half length of the pin and the natural base. The linearized stiffness of Hertz contact, $K_h$, represents the slope on the load and deflection curve characterizing the contact phenomena. The system stiffness is therefore,

$$K_c = \frac{1}{\left(\frac{1}{K_h}\right) + \left(\frac{1}{K_m}\right)} \tag{2}$$

During contact stages the relationship, represented by equation (2), although it is nonlinear, is not too far away from linear. Therefore, the system stiffness has essentially a piecewise linear characteristic which may be used to model complicated nonlinear behavior of intermittent motion mechanism. On the other hand, equation (2) is simple enough to estimate and can be used to verify the response of the dynamic system with simple input, such as harmonic force.

The damping of this system is modeled through a new damping function introduced in this investigation, as $D$, and will represent the major content of our discussions in the next few sections. The equation of motion for the model, shown in Fig. 1, may be easily written as,

$$M\ddot{X}_r + D\dot{X}_r + K_c X_r = P(t) \tag{3}$$

where $M$ represents the equivalent mass of $M_1$ and $M_2$, $D$ and $K_c$ denote the damping function and equivalent system stiffness, respectively, and $X_r$ represents the relative displacement between $X_1$ and $X_2$. A simple numerical integration scheme, for instance, the Runge-Kutta scheme, can be used to yield the solution of equation (3).

In the modeling of damping, it is convenient to model it by viscous damping using a damping ratio which is generally known to be speed and load dependent. However, an accurate estimate of this ratio is difficult. This is apparent in many of the previous investigations on the study of the dynamics of a mechanical system, such as mechanical joints [11].

In this investigation, one of our purposes is to model damping in a way that some of the modeling parameters could be estimated from either empirical or published experimental data. This is done by introducing a damping function, rather than the damping ratio, and to express it in terms of the product of a damping factor and another function. The former can be derived from the coefficients of restitution which can be found experimentally and such data are available in the literature [16]. The latter depends, more or less, on a heuristic choice such that the resulting damping force would represent the required dynamic characteristics of the system, such as the boundary conditions on the hysteresis loop. Two types of damping functions are presented in this study. It will be shown later that the modified viscous

damping approach is preferred. We begin with the first damping function.

## 3 First Damping Function, $D_1$

Let $D_1$ represent the first damping function, we then define,

$$D_1 = C_1 \cdot T_1(X_r) \tag{4}$$

where $C_1$ represents a damping factor and $T_1(X_r)$ is a displacement function.

**3.1 Displacement Function, $T_1(X_r)$.** The displacement function is essentially a surface deflection function. Following the approach of Hunt and Crossley [12], instead of using a displacement function which is a power series, we simply choose a linear function, i.e.,

$$T_1(X_r) = X_r \tag{5}$$

The function, $T_1(X_r)$, represents the simplest form of a surface deflection function whose corresponding damping force can satisfy the expected boundary conditions of the zero damping force at $X_r = 0$ and $X_r = X_{r\max}$.

**3.2 The Damping Factor, $C_1$.** The damping factor, $C_1$, is derived from the coefficient of restitution, $b$. By representing $b$ as a polynomial in terms of the relative approaching velocity of two impact bodies obtained from the experimental data and equating it to the calculated value from the equation of motion, an expression of $C_1$ can be derived. The procedure is outlined in the following.

1) By correlating the data from a good account of many experiments [16] conducted with different initial velocities of impacting bodies, we can express $b$ by means of a least squares fit as:

$$b \doteq \alpha_0 - \sum_{k=1}^{s} \alpha_k V^k \tag{6}$$

Taking only the first term on the series, we then have,

$$b \doteq \alpha_0 - \alpha_1 V \tag{7}$$

where $V$ represents the relative approaching velocity of two impacting bodies and $\alpha_k$ denotes the coefficients of the approximating polynomial.

2) From the definition of classical mechanics the coefficient of restitution can be calculated,

$$b = -\dot{X}_r / V \tag{8}$$

where $\dot{X}_r$ represents the relative departing velocity, and it can be solved from the equation of motion.

The equation of motion, equation (3), can now be rewritten as,

$$M\ddot{X}_r + (C_1 X_r)\dot{X}_r + K_r X_r = P(t) \tag{9}$$

The analytical solution of equation (9) is difficult to obtain due to the nonlinear term associated with the damping. However, a homogeneous solution of equation (9) can be obtained using the polynomial approximation, i.e.,

$$X_r(t) \doteq V_r t - \frac{(C_1 V_r + K_r)}{6M} V_r t^3 + \frac{(4C_1 V_r + K_r)(C_1 V_r + K_r) V_r}{120M^2} t^5 + \dots \tag{10}$$

The relative velocity after impact may then be obtained as,

$$\dot{X}_r(t_c) \doteq V - \frac{(C_1 V_r + K_r)}{2M} V_r t_c^2 + \frac{(4C_1 V_r + K_r)(C_1 V_r + K_r) V_r}{24M^2} t_c^4 + \dots \tag{11}$$

where $t_c$ corresponds to the time at the moment that two bodies are separating. Rewriting equation (8), we obtain,

$$b = 1 + \left(1 - \frac{K_r t_c^2}{12M}\right)\frac{K_r t_c^2}{12M} + \left(1 - \frac{5K_r t_c^2}{12M}\right)\frac{C_1 t_c^2}{2M} + \frac{C_1 t_c^4}{6M^2} V_r^2 + \dots \tag{12}$$

Equating the coefficients of like powers of $V_r$ from equations (7) and (12), we obtain,

$$C_1 \doteq \frac{2\alpha_1 M}{\left(\frac{5K_r t_c^2}{12M} - 1\right) t_c^2} \doteq 0.75\alpha_1 K_r \tag{13}$$

Equation (13) shows that the damping factor, $C_1$, is proportional to surface stiffness, and the coefficient $\alpha_1$ which agrees with the findings reported by Hunt and Crossley [12] uses an energy balance based on an estimated dissipated energy of impact bodies.

The first damping function can therefore be represented as

$$D_1 \doteq (0.75\alpha_1 K_r) X_r \tag{14}$$

Because of the displacement function, the derived damping function, equation (14), will give a damping force satisfying the required hysteresis conditions.

## 4 Second Damping Function, $D2$

Viscous damping has been commonly used in the modeling of system damping, such as Dubowsky and Freudenstein's model [11]. This approach, although convenient mathematically, has certain limitations. First, it would lead to a damping force which is maximum at the beginning of the impact process because of the use of a constant damping coefficient, and second, this would give a negative sum of damping and spring forces during the return stoke of the hysteresis loop. In addition, the value would reach its peak when the relative displacement between two bodies vanishes (Fig. 3). These situations are not realistic and often make the viscous model ineffective. It is therefore desirable to develop a new approach which would satisfy the hysteresis conditions of impact as well as preserve the basic characteristics of viscous damping.

The proposed second damping function, $D_2$, is a modified viscous damping factor. It is the product of a damping factor and a smoothing function, or a transition function. Instead of treating the damping factor as a constant throughout the impact process, like the conventional approach, a function called the transition function, denoted as $T_2$, is introduced. It is essentially a smoothed step function. When it is multiplied by the damping factor, $C_2$, the resulting damping function would represent the behavior of system damping, especially in the initial impact period. The derivation of the damping factor, $D2$, follows a similar approach as the first damping factor, $D1$.

The transition function, shown in Fig. 2, is defined in a transition zone specified by the region $0 \le X_r \le \epsilon$ where the lower and upper bounds correspond to the initial and final stages of the impact process. There may be various ways to define the transition function, one way to represent is:

$$T_2(X_r) = \frac{X_r + |X_r|}{2X_r} \exp\left[|(X_r - \epsilon) - |X_r - \epsilon|](q/\epsilon)\right] \tag{15}$$

where the parameter $\epsilon$, which has a unit of displacement, defines the width of transition zone, and $q$ is a parameter specifying the curve path within the transition zone.

Figure 2 represents a graphical form of equation (15). The transition function is zero when $X_r \le 0.0$ and is one when

$X_c = \epsilon$. The value of $\epsilon$ may be arbitrarily chosen, but it must satisfy the following conditions:

$$0 < \epsilon < X_{c\max} \tag{16}$$

and

$$C_2 T_2(X_c)\dot{X}_c + K_c X_c \geq 0 \tag{17}$$

Equations (15) and (17) provide the conditions that guarantee the sum of the damping and spring forces to be positive, i.e., the hysteresis loop is within the first quadrant (Fig. 3).

**4.1 Damping Factor, $C_2$.** The second damping factor is supposed to have the same characteristics as a viscous damping coefficient, which can be calculated by knowing the homogenous solution of equation (3) with zero transition zone, and then following the same procedures as the calculation of the first damping factor. It gives

$$C_2 = 2M\omega_n \sqrt{\frac{(\ln b)^2}{(\ln b)^2 + \pi^2}} \tag{18}$$

Equation (18) can be used to estimate the damping factor of impacting bodies due to translation. Larger coefficient of restitution means lower damping factor and stiffer surface compliance leads to a larger damping factor or a lower coefficient of restitution. The second damping function can be written as

$$D_2 = C_2 \cdot T_2(X_c) \tag{19}$$

The new damping function, $D_2$, gives a damping force similar to the one predicted by Dubowsky [11], except in the transition zone. The damping varies exponentially in the transition zone and it is invariant elsewhere. The corresponding damping force, therefore, is zero at the beginning and the end of impact; and it reaches maximum or minimum value at $X_c = \epsilon$ depending upon whether the damping process is in its working or returning stroke. With this approach, the resulting hysteresis boundary conditions are satisfied.

The major difference between the two proposed damping functions is that the first damping function is a nonviscous model while the second is a viscous model. Consequently, the damping force derived from the first function gives a much thinner hysteresis loop as compared to the second and it is particularly thin during the high speed zone. This is a drawback and will become obvious in our later discussions.

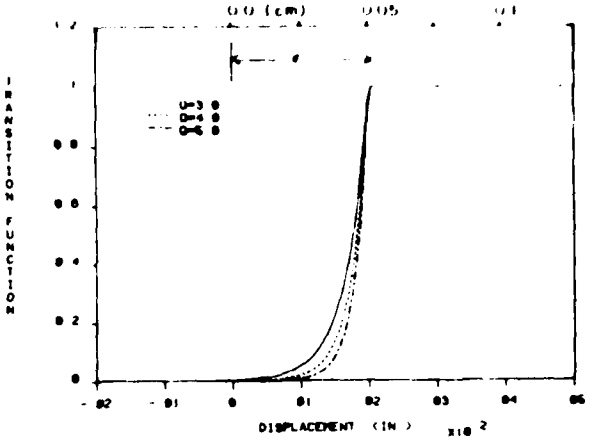


Fig. 2 The transition function

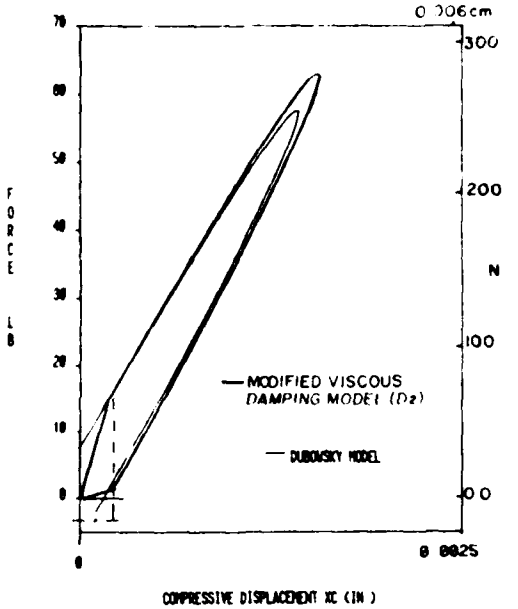


Fig. 3 Comparison of hysteresis loop of various viscous models

## 5 Dynamic Load

In the design of high-speed intermittent-motion mechanisms, stress distribution on machine parts as well as the contact stress between two impacting parts are of major concern. In order to evlauate these stresses, the load must be known, but the determination of this load is not simple. Due to the inherent shock loading of the intermittent-motion mechanism and other factors such as backlash, elastic deformations under load, imbalance, load and the inertias of mechanism components, the resulting action is a variable dynamic load. Not many investigations on the dynamic load of intermittent-motion mechanisms are on the record [17]. Lee [17] presented a simple dynamic model using the classical mechanics theory to predict the dynamic load of a Geneva mechanism, and showed that the effect of the dynamic load is significant, especially at higher speeds. It is therefore the primary concern in this investigation to apply the proposed model in order to predict the dynamic load of a general class of intermittent-motion mechanisms.

It is expected that the result would represent an improvement over Lee's [17] since most of the dynamic characteristics of intermittent-motion mechanisms have been considered in the present model. The result of that comparison will be presented in [18].

The dynamic load, $P_d$, is defined as,

$$P_d = K_c \cdot X_c \tag{20}$$

The spring deflection, $X_c$, is the solution of the equation of motion (equation (3)) and can be obtained numerically, depending on the geometrical parameters of the mechanism, the load condition $P(t)$, and the initial conditions, $X_c(0)$ and $\dot{X}_c(0)$. The spring deflection is also an implicit function of many factors such as clearance, equivalent mass, spring stiffness and damping, etc.

The dynamic load ratio is a useful parameter and is introduced and defined as follows:

$$\text{Pr} \equiv \frac{P_d}{P} \tag{21}$$

This parameter is dimensionless and is used to measure the dynamic effect of the mechanism. Almost similar in function to the classical "design acceleration factor" [8], which is a function of the weight of the part and its natural frequency of

vibration, the dynamic load ratio is derived based on the "starting velocity" concept which is considered to be more accurate in the modeling of high-impact shock problems. The model is assumed to be accelerated up to some finite velocity in a negligible length of time and then maintains that velocity during the initial and most important phase of the shock motion. The parameter, Pr, is useful in the design of intermittent-motion mechanisms.

## 6 Comparative Study

The model proposed in this investigation has certain characteristics which make it especially suitable for the dynamic study of intermittent-motion mechanisms. In this section a comparative study of the present model with some of the known conventional dynamic models is presented. The purpose is to demonstrate these characteristics.

Three types of models which are representative and well-known are chosen for comparative study. These are: Dubowsky and Freudenstein's impact pair model [11]; Hunt and Crossley's model [12] and Herbert and McWhannell's model [13]; and the classical model of Johnson [9]. Each of these selected models has its own characteristics and merits. Our investigation owes much to these previous investigators whose results have been an inspiration and have prompted this study.

Realizing the loading condition varies with different mechanisms, for comparison purposes a harmonic forcing function is assumed for all models. In addition, initial conditions are the same (zero initial displacement and an initial velocity of 25.4 cm/s). We are concerned essentially with the behavior of the following quantities which characterize a dynamic model. These are: the output motion characteristics; the hysteresis loop; and the dynamic load. We begin with the motion characteristics.

**6.1 Motion Characteristics.** Displacement curve of various models obtained numerically from the equation of motion are plotted in Fig. 4. They represent the solution of a complete cycle of a sinusoidal forcing function with same initial conditions. We have the following conclusions:

1. Because of the impact forcing function and the initial conditions, the displacement curves of various models have the following three different modes: (*a*) contact mode – this is found on the first half period of the driving force due to low initial velocity, and consequently, low kinetic energy, the mass, $M_2$, in this mode, generally making contacts with the mass, $M_1$. (*b*) free-flight mode – it occurs when the driving force changens its direction. In this mode, the mass $M_2$ loses contact with the mass $M_1$ and is ready to impact on the opposite side of the mass $M_1$. (c) impact mode – it occurs in the second half of the period. A characteristic of this mode is that the impact phenomena dominate and there are frequent impacts and bounces. This is due to the high kinetic energy resulting from the previous free-flight mode.

2. Besides having three modes, the displacement curve consists also of two components of frequency response. One component corresponds to the forcing frequency and the other, which is superimposed on the first, has a frequency relating on the surface compliance, the equivalent mass and the damping of the system.

3. A comparative study of various displacement curves, as shown in Fig. 4, demonstrates an interesting remark. The solution obtained from using the second damping function (i.e., the viscous model) is more stable than the ones obtained by nonviscous models, namely, the first damping function, and the models of Hunt [12] and Herbert [13]. This instability is primarily due to the displacement-dependent nature of the nonviscous models which predict a low damping force at or near the high speed region of the impact process, i.e., near

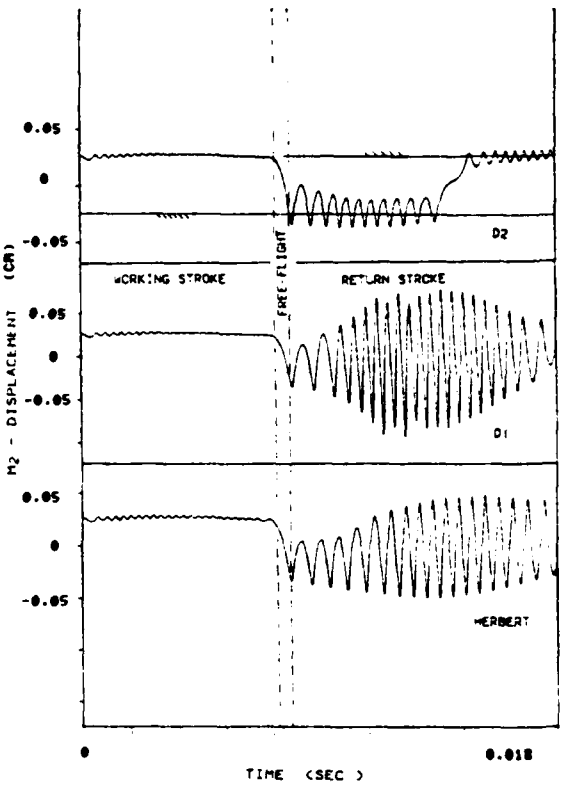


**Fig. 4 Motion characteristics of various models**

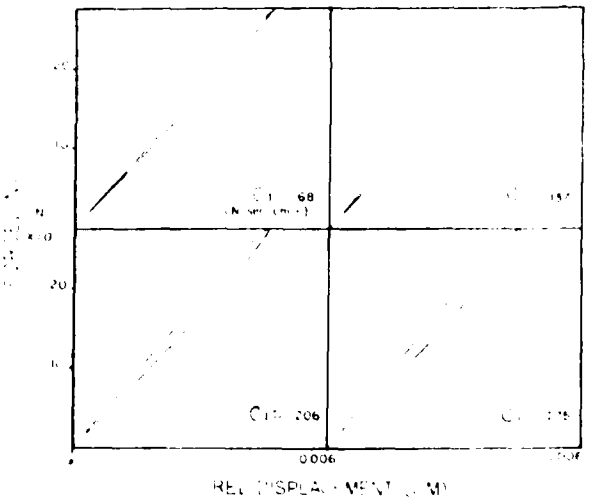


**Fig. 5 Hysteresis diagram using the first damping function with different damping factors**

$X_i = 0$. This shows that the second damping function is more realistic than the first damping function.

**6.2 Hysteresis Diagram.** A comparative study on hysteresis diagram is of importance since it demonstrates the damping characteristics of the dynamic model. The following are the conclusions drawn from this study:

1. The first damping function has certain characteristics: First, the hysteresis loop is generally thinner than the one predicted using the viscous model. This implies that lower dissipation energy is expected from the model. Second, the

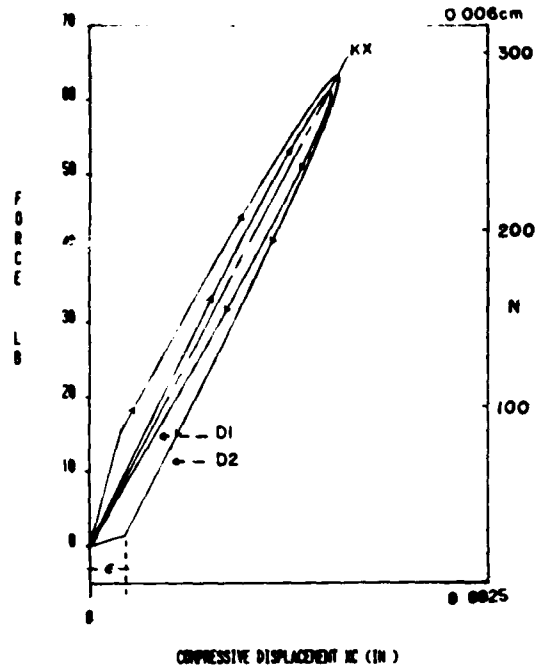


Fig. 6 Surface hysteresis loops predicted by different damping functions

hysteresis diagram is thinner in the high speed region of the impact process, i.e., near the origin, compared with elsewhere. It remains to be thin even with the increasing damping factor, as shown in Fig. 5. This is not realistic and may be considered to be a drawback of the first damping function, or the nonviscous model in general.

2. The second damping function is a viscous model which relates closely to Dubowsky's model except in the transition zone. The required boundary conditions are now satisfied, i.e., the calculated damping force vanishes at the origin.

3. The difference between the first and the second damping functions is apparent (Fig. 6). The former is not a viscous model and the dissipation energy predicted is always much lower than the one predicted using the second damping function.

Another way to see the difference between the two damping functions is to consider a special case when the clearance, $r$, vanishes in the physical model and ask what would happen to the hysteresis diagram. As $r$ approaches zero, the nonviscous model (the first damping function) would present a number of eight-shaped hysteresis diagrams while the second damping function would predict the expected elliptical shape (Fig. 7) which conforms to the classical Kelvin-Voigt model where there is no impact at all.

**6.3 Dynamic Load.** From the designer's point of view, information on the dynamic load is of ultimate concern which leads to the evaluation of stresses on machine parts. In the following a comparative study on dynamic load using various models is given and the comparison is on three areas: the dynamic load profile, the effect of initial conditions on the dynamic loads, and extreme values of the dynamic load. We first begin with the comparison of the dynamic load profile.

*6.3.1 Dynamic Load Profile.* The dynamic load profile will reveal much information regarding the dynamics of the impact, such as the maximum impact force or the dynamic load $F$, the compressive displacement ($X = K_v/F$), duration of contact, and the distribution of dynamic force during impact. A comparison of various dynamic load profiles is given in Fig. 8. The following conclusive remarks may be drawn:

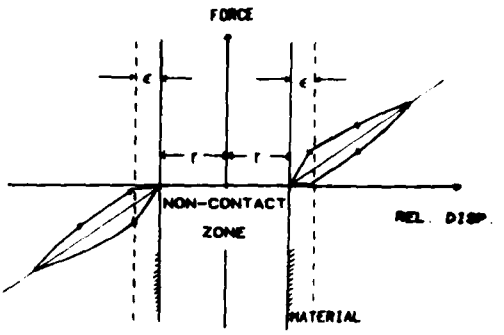


Fig. 7(a) with clearance

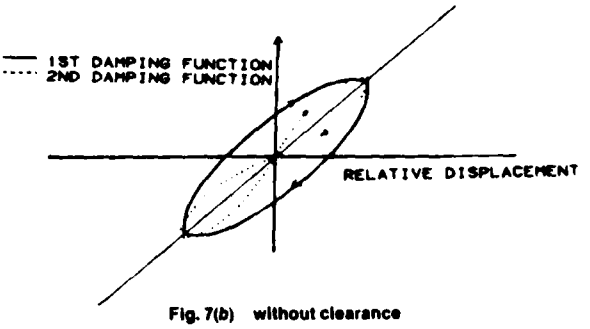


Fig. 7(b) without clearance

Fig. 7 Surface hysteresis diagrams of various models

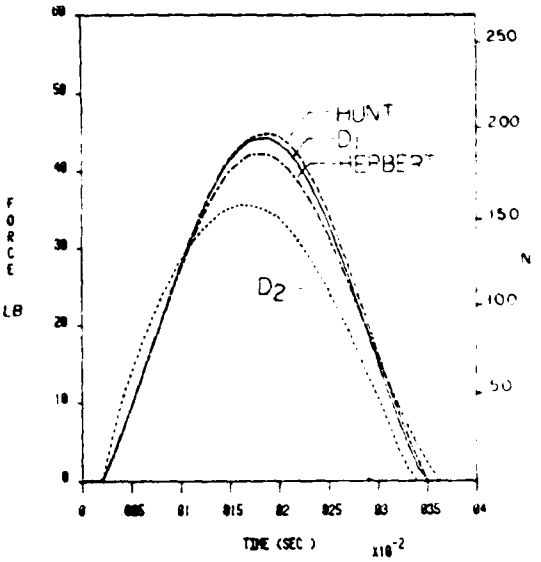


Fig. 8 Dynamic load profiles

1. Two groups of curves can be seen, one corresponds to the viscous model and the other belongs to the nonviscous model. It is shown that the first damping function gives a dynamic load profile between Hunt's [12] and Herbert's [13] models, and all give a larger dynamic force compared to the viscous model during most of the contact. This is due to the fact that less energy is dissipated and much is being used to contribute to impact.

2. The rate of change of the dynamic load is higher at the initial period of impact for the present model using the second damping function than for the nonviscous models.

3. The contact time for the second damping function is less

Table 1 Extreme values of the dynamic load obtained from various models

| | THIS INVESTIGATION | | JOHNSON | DUBOWSKY | HUNT | HERBERT |
|---|---|---|---|---|---|---|
| | $\zeta_1$ | $\zeta_2$ | | | | |
| INFINITE-MASS ASSUMPTION | 554 | 521 | 563 | 514 | 559 | 542 |
| FINITE-MASS ASSUMPTION | 549 | 515 | 557 | 509 | 554 | 538 |

INITIAL VELOCITY $v_1=0$, $v_2=51.3$ [illegible], $R_1=0.624$ KG (or $\infty$), $R_2=0.0622$ KG, AND $E=70050$ N/CM.

than the one predicted by the nonviscous models. This is because much of the energy is dissipated, and, therefore, the system has less energy to do work in order to maintain contact. Separation therefore occurs earlier.

4. The dynamic load profile of the second damping function approximates most closely a half sine except at the initial phase and the finishing stage of contact.

*6.3.2 Extreme Values of the Dynamic Load.* It is interesting to examine the dynamic load predicted by various models under an extreme condition, namely the condition that one of the impacting body, say, body 1, is considered to be fixed, i.e., $M_1 = \infty$. This is essentially the infinite-mass assumption used by Johnson [9]. The purpose is to give an estimate of the maximum possible dynamic load range. The following remarks can be made referring to Table 1:

1. Comparing all models, Johnson's model gives the highest maximum dynamic load range. This is due to the fact that his model does not consider damping.

2. The maximum dynamic loads predicted by the reset of the models fall into two distinct categories. On the category of viscous models, the value predicted by the second damping function is slightly higher than Dubowsky's model. However, both give much smaller predictions than the nonviscous models.

## 7 Summary of Conclusions

1. A dynamic model which is especially formulated for intermittent-motion mechanisms is presented. Dynamic characteristics of this model are demonstrated.

2. A new approach to model the system damping is presented by introducing a damping function rather than the conventional damping ratio used in the viscous model. Two types of damping functions are proposed: One represents a nonviscous model; the other represents a viscous model. There are many advantages of the present approach: First, both of these functions predict a damping force which satisfies the expected hysteresis boundary conditions. Second and more important, unlike the damping ratio which is difficult to estimate, these functions can be estimated systematically through a procedure outlined in this investigation. They are derived in terms of physical parameters, such as coefficient of restitution which can be obtained experimentally. As more experimental data become available, a predicative dynamic model can be established.

3. Out of the two proposed damping functions, the second damping function (viscous model) which involves a transition function is favored. It offers solutions which are more stable and realistic as compared to the first damping function or the nonviscous damping model in general. Moreover the second damping function would predict a hysteresis diagram which conforms with the classical Kelvin-Voigt model of nonimpact as the clearance vanishes. Basic theory and model presented here will be applied to three practical intermittent-motion mechanisms, i.e., Geneva mechanisms, ratchets, and escapements, the results of which are presented in Part II.

## Acknowledgments

The authors are grateful to the Army Research Office for the support of this research throught Contract DAAG29-81-K-0016 to Rutgers University.

## References

1 Bickford, J. H., *Mechanisms for Intermittent Motion*, Industrial Press, N. Y., 1972.

2 Tschwitz, O., "Mechanisms for Intermittent Motion, Part I," *Machine Design*, Dec. 1951, pp. 134–148.

3 Lee, T. W., and Shereshevsky, Y., "Kinematic Synthesis of Planar Two Gear Drives with Prescribed Dwell Characteristics," ASME *Journal of Mechanical Design*, Vol. 4, No. 4, pp. 687–698.

4 "Scanning the Field for Ideas," *Machine Design*, Dec. 8, 1966, p. 194; Ferguson Indexing Catalog No. 180, Ferguson Machine Company, St. Louis, Missouri.

5 Yang, A. T., and Hsia, T. M., "Multistage Geared Geneva Mechanism," ASME *Journal of Mechanical Design*, Vol. 101, No. 1, Jan. 1979, pp. 41–46.

6 Fenton, R. G., "Geneva Mechanisms Connected in Series," ASME *Journal of Engineering for Industry*, Vol. 97, No. 2, May 1975, pp. 603–608.

7 Crossley, F. R. E., Editor, *Proceedings of International Conference for Teachers of Mechanisms*, The Shoe String Pre, Inc., 1964, pp. 110–111.

8 Langer, B. F., "Design to Withstand High Impact Shock," *Machine Design*, Aug. 1955, pp. 193–197.

9 Johnson, R. C., "Impact Forces in Mechanisms," *Machine Design*, June 12, 1958, pp. 138–146.

10 Kobrinskiy, A. E., and Babitzky, V. I., "Periodic Movements of a Two-Mass Vibration System in a Cavity," (in Russian), *Trud. Mash. Mekh.*, Vol. 103, 1964, pp. 56–70.

11 Dubowsky, S., and Freudenstein, F., "Dynamic Analysis of Mechanical Systems with Clearances, Part I & II," ASME *Journal of Engineering for Industry*, Feb. 1971, pp. 305–316.

12 Hunt, K. H., and Crossley, F. R. E., "Coefficient of Restitution Interpreted as Damping in Vibroimpact," ASME *Journal of Applied Mechanics*, June 1975, pp. 440–445.

13 Herbert, R. G., and McWhannell, D. C., "Shape and Frequency Composition of Pulses from an Impact Pair," ASME *Journal of Engineering for Industry*, Aug. 1977, pp. 513–518.

14 Dubowsky, S. and Gardner, T. N., "Dynamic Interactions of Link Elasticity and Clearance Connections in Planar Mechanical Systems," ASME *Journal of Engineering for Industry*, May 1975, pp. 652–661.

15 Hanes, R. S., "Survey: 2-Dimensional Motion and Impact at Revolute Joints," *Mechanisms and Machine Theory*, Vol. 15, 1980, pp. 361–370.

16 Goldsmith, W., *Impact*, Edward Arnold Ltd., London, 1960.

17 Lee, T. W., "Optimization of Higher Speed Geneva Mechanism," ASME *Journal of Mechanical Design*, July 1981, Vol. 103, pp. 621–630.

18 Wang, A. C., and Lee, Ting W., "On the Dynamics of Intermittent Motion Mechanisms. Part 2: Geneva Mechanisms, Ratchets and Escapements," this issue ASME JOURNAL OF MECHANISMS, TRANSMISSIONS, AND AUTOMATION IN DESIGN, pp. 541–551.

# On the Dynamics of Intermittent-Motion Mechanisms.

## Part 2: Geneva Mechanisms, Ratchets, and Escapements

**A. C. Wang**
Research Assistant.

**T. W. Lee**
Assoc. Professor
Mem. ASME

Department of Mechanical and Aerospace Engineering, Rutgers University, New Brunswick, N.J. 08903

*The theory developed in Part 1 has been applied to the determination of the dynamic response of three typical types of intermittent-motion mechanisms, namely, Geneva mechanisms, ratchets, and escapements. Insight into the behavior of such mechanisms can be obtained by studying the characteristics of the mathematical model and by numerical experiments. The results, wherever possible, are illustrated by computer-plotted graphs. A comparative study with some limited current investigations on the same subject is provided.*

Possibly the most significant result of this investigation is that a dynamic model and its associated new approach on system damping, proposed in Part 1, will exhibit the complicated behavior common to intermittent-motion mechanisms. It is the purpose of this part of the investigation to demonstrate this finding. In the following, three intermittent-motion mechanisms - Geneva mechanisms, ratchets, and escapements which are believed to be representative and of practical interest, are chosen for study. In each of them, we are concerned with the motion and dynamic characteristics of its components as well as its dynamic load. Information such as this is essential for design. We begin first with the Geneva mechanism.

### Geneva Mechanism

**1 Introduction to Geneva Mechanism.** The Geneva mechanism is a popular indexing device. It converts a uniform rotary motion to an intermittent rotary motion. The main advantage of the mechanism lies in its simplicity. However, the Geneva mechanism has two undesirable characteristics: First, the output motion starts and ends with nonzero accelerations which usually induce shock loading and can produce vibration in the driven system; and secondly, there exists high contact stress between the drive pin and the wheel slot, which can cause pin wear and wheel breakage. Both of these factors adversely affect performance and life, and impose severe constraints on high-speed operation. Despite its inherent limitation, the Geneva mechanism continues to serve as a common and useful indexing device, even at high speed.

There are several reasons to choose this mechanism for study. First, it is a popular indexing device which has been widely used in industry. Second, there are not too many investigations of the dynamics of this mechanism on the record, except in a very few cases [1, 2]. The mechanism has been operated at high speeds regardless of its inherent dynamic limitations, and as a result, pin wear and wheel breakage has often occurred. It is, therefore, necessary to gain deeper understanding of the mechanism and to obtain some design guidelines. Consequently, the study of the dynamics of Geneva mechanisms for high-speed application is both of important and of practical interest.

The Geneva mechanism design has been the subject of investigation for many years [3]. Much of the work concerns, however, the kinematics of the mechanism. This is mainly due to the lack of a mathematical model which can adequately represent the difficult impact phenomena involved in intermittent-motion mechanisms. Recently Lee [4], using classic mechanics theory, presented a set of performance parameters and applied optimum design on Geneva mechanisms. A simple dynamic model, similar to the one used on gear dynamics, was first introduced to estimate the Geneva dynamic load. In this paper, the model developed in Part 1 is applied to provide a more predictive dynamic model on the dynamics of Geneva mechanisms.

**2 Dynamic Response of Geneva Mechanisms.** This section begins with a description of the kinematics and the dynamic modeling of the Geneva mechanism. Then, numerical experiments on the application of the dynamic model are presented and finally a discussion is given.

Figure 1 shows the motion graphs of a typical four-station Geneva mechanism. In the study of the dynamics of Geneva mechanisms, the model of Part 1 is used. Referring to the Fig. 1 of Part 1, the parameters $M_1$ and $M_2$ represent in this case the equivalent mass of the Geneva wheel and pin, respectively. The spring coefficient, $K_s$, denotes the equivalent stiffness of the material compliance and the mechanism elasticity. A simple cantilever beam approach which was employed by Lee [4] was adopted again to represent the Geneva mechanism

Contributed by the Mechanisms Committee and presented at the Design and Production Engineering Technical Conference, Washington, D.C., September 12-15, 1982 of THE AMERICAN SOCIETY OF MECHANICAL ENGINEERS. Manuscript received at ASME Headquarters June 10, 1982. Paper No. 82-DET-65.

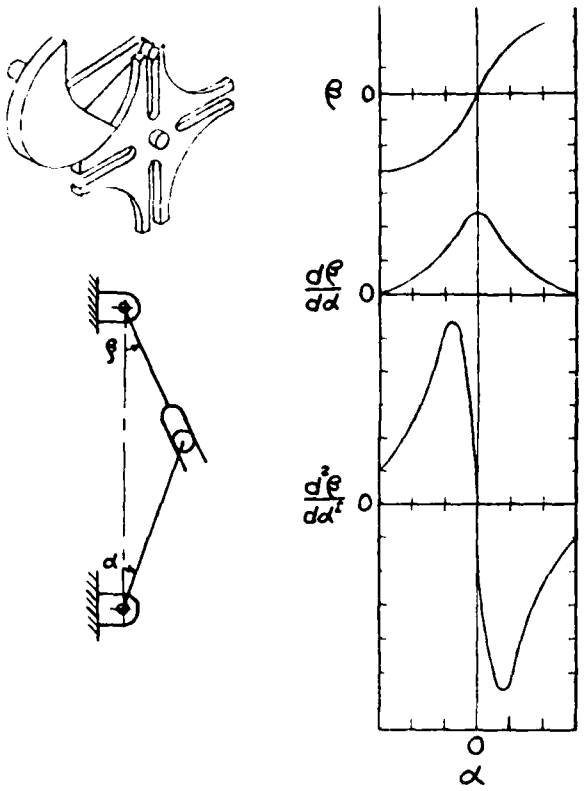


Fig. 1 The kinematics of the Geneva mechanism

elasticity. The modified viscous damping approach (i.e, $D_2$) presented in Part 1 is used for the system damping function, $D$. The forcing function $P$ refers to the applied load at the center of the Geneva pin. The clearance $r$ denotes the clearance between the Geneva pin and wheel.

In the numerical experiments of the dynamic model, the equation of motion is solved starting at the contact mode with a given pin initial velocity, say, 2.54 cm/s. The dynamics of the pin and Geneva wheel as well as the dynamic load ratio are obtained and given in the following.

*2.1 Pin Dynamics.* The pin dynamics can be illustrated from a time-displacement plot. Figure 2 shows the pin movement which consists of vibratory effect due to Geneva load. During the working stroke, the pin is usually in contact with the wheel surface. During the return stroke, however, there is an observable period of free-flight mode (i.e., noncontact). This is due to the high impact velocity introduced by the clearance and the Geneva static load.

Certain observations can be made from Figure 2.

1 The pin in general follows the behavior of the applied load, $P(t)$. The motion of the pin, as shown from the displacement plot, characterizes the superposition of two effects, namely, the applied load and the vibration which is due to stiffness and system damping.

2 The pin-displacement plots are characterized by a successive sequence of free-flight and contact modes at the beginning of both the working and the return strokes.

(*a*) The free-flight mode is caused by the bounce of the pin which depends on the impacting velocity and the static load applied upon it. During the free-flight mode, the pin is driven by the load $P$ only, therefore, the pin velocity increases with an increasing slope until it reaches a position where the load reaches maximum.

(*b*) At contact mode, the maximum relative displacement, $X_{c_{max}}$, occurs at the initial stage of either the working or return stroke.

3 The relative velocity curve shows that the velocity changes abruptly at the initial stage of both the working stroke and the return stroke, and is then followed by a stable region of contact mode.

*2.2 Wheel Dynamics.* The dynamics of the Geneva wheel are shown in Fig. 3. Dynamic effects can be seen from the figure, which cause certain distortions of the kinematic profiles of wheel displacement and velocity (Fig. 1). During the noncontact period, the wheel separates from the pin, and moves essentially at a constant velocity due to inertia. In the contact region, acceleration remains almost constant while the velocity of the wheel changes abruptly. Clearance has an influence on the separation of the pin and the wheel. Consequently, it has a dominating effect on the dynamics of the Geneva wheel.

*2.3 Geneva Dynamic Load Ratio.* In this section, the dynamic load ratio of the Geneva mechanism is investigated. The discussion includes: the effects of pin velocity, surface compliance, and clearance on the dynamic load ratio. The following gives a detailed discussion.

1 Using different initial pin velocities, the calculated dynamic loads are shown in Fig. 4(*a*). It shows that the dynamic load is affected by the initial pin velocity on the working stroke of the Geneva motion, while on the return stroke the effect is not apparent. This is because of the viscous damping function which can effectively absorb the impact. Therefore, the starting velocity of the working stroke has essentially no effect on the return stroke.

2 The effect of surface compliance is shown in Fig. 4(*b*). Two different values of stiffness are used, one using a surface compliance of $3502.5 \times 10^4$ N/m, the other using a surface compliance of $7005.0 \times 10^4$ N/m. The graph shows that the surface compliance has a dominant effect on the return stroke of Geneva motion. This implies that the dynamic load of a softer surface is generally lower than the dynamic load of the stiffer surface, and this is of course obvious from intuition.

3 Figure 4(*c*) shows the effect of clearance on the dynamic load ratio. It has an important influence on the return stroke of the motion, but has no effect on the working stroke, and this is reasonable. Moreover, it is of interest to note that in increasing clearance, the peak of the dynamic load not only increases, but also delays on the return stroke. This is because the clearance allows the pin to increase the kinetic energy. Therefore, the larger the clearance, the larger the dynamic load on the return stroke.

From the foregoing discussions, several conclusions can be made: 1) The dynamic load between the pin and the wheel is considered to be an important design factor, which depends on many variables such as initial conditions, surface compliances and clearance. 2) Clearance has a dominating role on the dynamic load. Therefore, both controlling clearance and using a material with lower surface compliance are advantageous.

*2.4 Phase-Plane Plot.* Figure 5 contains the phase-plane plot of the motion of the Geneva mechanism and is a result of numerical calculation. The phase-plane analysis presents a convenient manner of displaying and interpreting the transient behavior of the nonlinear system. The following observations can be made:

1 In the initial stage of the contact mode, the pin generally exhibits bouncing. The bouncing depends upon the initial velocity of impact and the driving load.

2 The driving load plays an important role on the dynamic responses of the Geneva mechanism. Referring to the phase-plane plot, the graph is unsymmetric with respect to the line of zero velocity and is shifted toward the direction of the driving

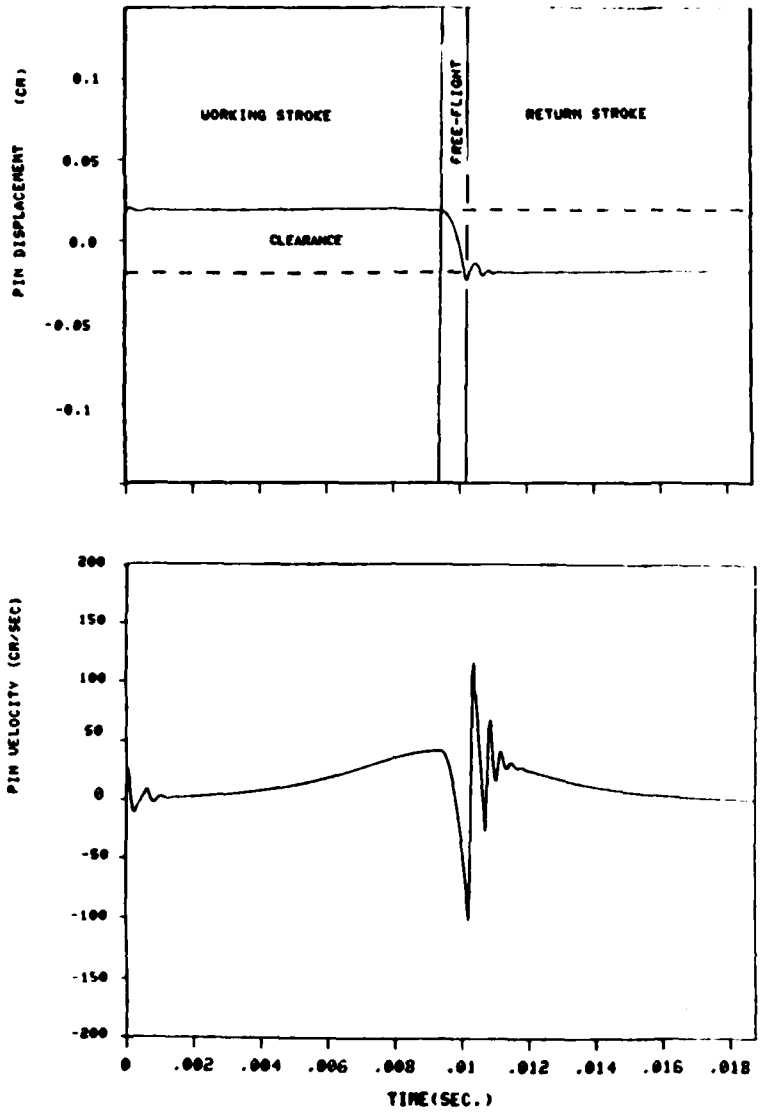


Fig. 2 The dynamics of the Geneva mechanism: pin displacement and velocity

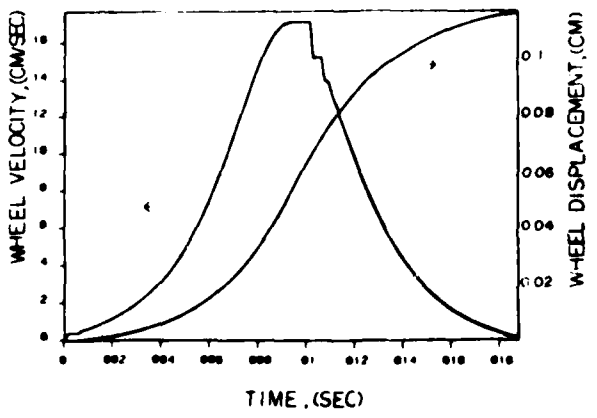


Fig. 3 The dynamics of the Geneva mechanism: wheel displacement and velocity

force. Furthermore, the slopes of the curve at the two boundary points $B$ and $C$ differ from each other. The phase-plane curve above the zero velocity line refers to the outward stage of contact, while the lower one refers to the inward stage of the contact. At the moment the pin impacts on the surface of the wheel (point $B$), its velocity reduces from 1.4 to 0 m/s. during the inward stage of contact, which converts the impact kinetic energy to potential energy. During the outward stage, the relative velocity increases from 0.0 to its maximum velocity of 0.75 m/s at point $C$, but decreases to 0.56 m/s at the boundary point $D$. This is due to the fact that the driving force acts in the opposite direction of the pin motion which is at the verge of bouncing off the surface.

3 There are two limit cycles of the phase plane plot due to the clearance. The size of the limit cycle depends on many factors, such as the impact velocity, driving force, clearance, and damping system, etc. It is of interest to see the limit cycle shown in Fig. 5. The graph shows a bounded, quickly damped limit cycle. This implies the Geneva mechanism, under proper design and operation, has small uncontrolled, but bounded vibrational characteristics between the pin and the wheel. This

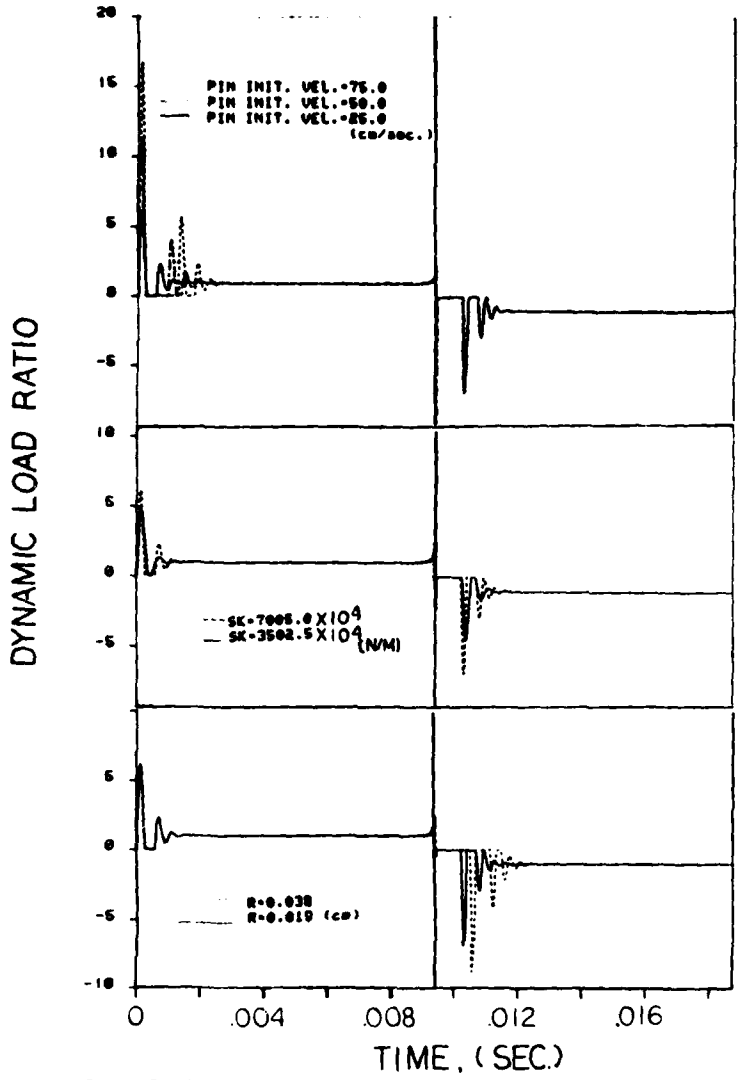


Fig. 4 The Geneva dynamic loads: (a) the effect of initial velocity; (b) the effect of surface compliance; and (c) the effect of clearance

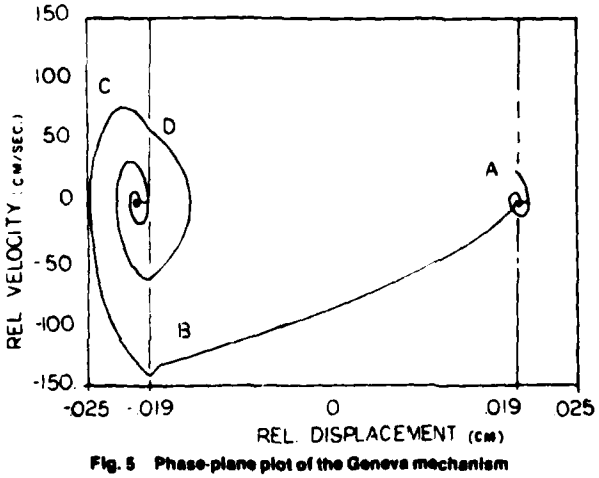


Fig. 5 Phase-plane plot of the Geneva mechanism

unstable vibration can be quickly stabilized after a few bounces. Therefore the system is a stable one globally.

## Ratchets

**3 Introduction to Ratchets.** The ratchet is a simple mechanism and is also a versatile device. A schematic diagram of a ratchet mechanism is shown in Fig. 6. The mechanism has many advantages, such as simplicity, low cost, and reliability, and it is also noted for its ability to carry a large load in relation to its size. But there are disadvantages also. It is mainly an impacting mechanism and therefore has very poor dynamic characteristics. Although there were ways to reduce the impacts in certain versions, impact will almost always be present to some extent, and this can lead to noise, wear, control, and stability problems unless the rest of the system is properly designed. A major problem lies in the fact that the forces resulting from impacts are amplified throughout various members of the mechanism, which may be well in excess of the subsequent drive forces. The dynamics of ratchets are therefore important and warrant our investigation. In this section, the model developed in Part I is applied to a ratchet in order to predict its performance and motion characteristics. To the authors' knowledge, a comprehensive study on the dynamics of ratchets has not been performed and

reported in literature, although some kinematics on ratchets are available [6]. This investigation, therefore, represents a first attempt to treat the dynamics of ratchets. We begin by discussing the basic kinematics of the ratchet mechanism using an analytical approach.

**4 The Kinematics of Ratchets.** The kinematic motion of a ratchet mechanism generally can be classified into two modes: (1) the free-flight mode, and (2) the contact mode. Each of these modes is discussed in the following.

*4.1 Free-Flight Mode.* The free-flight mode occurs when the pawl does not make contact with the ratchet wheel (Fig. 6(*b*)), and consequently does not drive the wheel. Using complex numbers, we can write the closure equation as

$$ce^{i\phi} + be^{i\alpha} + he^{i\beta} - ae^{i\psi} + d = 0 \tag{1}$$

with $h \le s$, and $\beta = \beta_o + \psi$ as the constraint conditions. Rewriting equation (1), we have,

$$\left.\begin{aligned} c\cos\phi + b\cos\alpha + h\cos\beta - a\cos\psi + d = 0 \\ c\sin\phi + b\sin\alpha + h\sin\beta - a\sin\psi = 0 \end{aligned}\right\} \tag{2}$$

Expressing in terms of $h$,

$$h^2 = a^2 + b^2 + c^2 + d^2 + 2bc\cos(\phi - \alpha) - 2ac\cos(\phi - \psi) - 2ab\cos(\psi - \alpha) + 2d[c\cos\phi + b\cos\alpha - a\cos\psi] \tag{3}$$

The parameter $h$ is a distance parameter which can be used to define the region of various modes.

Referring to Fig. 6(*b*) and equation (3), if the parameter $h$ equals zero, the contact mode starts. At this mode the wheel contacts with the pawl, and therefore drives the wheel. When $h$ is larger or equal to $S$, the pawl shifts to the next ratchet tooth.

*4.2 Contact Mode.* When the pawl comes into contact with the ratchet wheel, the contact mode starts. Referring to Fig. 6(*b*), the closure equation of this mode can be written as:

$$ce^{i\phi} + be^{i\alpha} - ae^{i\psi} + d = 0 \tag{4}$$

Rewriting equation (4) into scalar equations,

$$\left.\begin{aligned} c\cos\phi + b\cos\alpha - a\cos\psi + d = 0 \\ c\sin\phi + b\sin\alpha - a\sin\psi = 0 \end{aligned}\right\} \tag{5}$$

Rearranging equation (5), we obtain:

$$a^2 - b^2 + c^2 + d^2 - 2ac\cos(\phi - \psi) + 2d[\cos\phi - a\cos\psi] = 0 \tag{6}$$

The equation (6) is equivalent to the displacement equation of a planar four-bar linkage. However, instead of being a constant rotation, the input motion for ratchets undergoes mostly a nonuniform oscillating motion. Equations (1) and (4) or equations (3) and (6) represent the motion characteristics of the ratchet wheel. They are useful in our study.

**5 Various Models of Ratchet Mechanism.** *5.1 The Classic Model.* In this section, the dynamics of ratchets are studied using classic mechanics approach. It is based on the assumption that the high-order effect caused by the elasticity of individual members is neglected. Two types of modes are considered: the contact mode, and the free-flight mode.

*5.1.1 The Free-Flight Mode.* During the free-flight motion, the wheel moves independently of the pawl. Therefore as a constant torque $T$ acts on the wheel, the equation of motion of the wheel is,

$$\ddot{\psi} = T/I_w \tag{7}$$

where $I_w$ denotes the wheel inertia.

The applicable initial conditions are:

$$\dot{\psi}(t_o) = \dot{\psi}_o \tag{8}$$

and

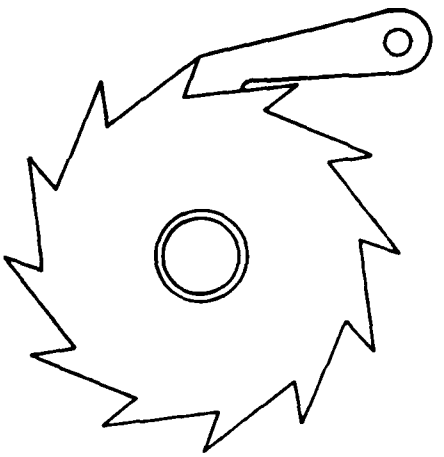

Fig. 6(*a*)

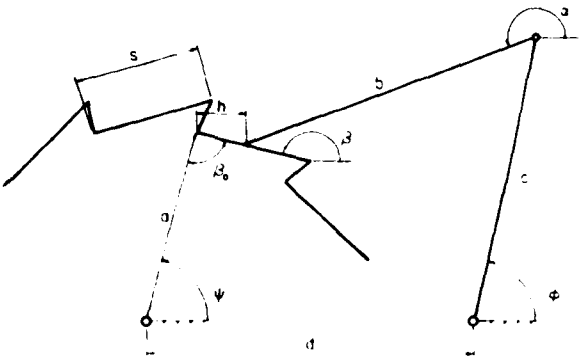


Fig. 6(*b*)

Fig. 6 The ratchet mechanism and its schematic

$$\psi(t_o) = \psi_o \tag{9}$$

Integrating equation (7) gives the angular displacement of the wheel.

$$\psi = \frac{T}{2I_w}(t - t_o)^2 + \dot{\psi}_o(t - t_o) + \psi_o \tag{10}$$

*5.1.2 The Contact Mode.* The equation of motion of the ratchet wheel can be expressed as

$$I_w\ddot{\psi}\mathbf{k} = \mathbf{a} \times P_n\mathbf{n} - (T_k) \tag{11}$$

where $\mathbf{n}$ and $\mathbf{k}$ are unit vectors and $\mathbf{a}$ represents the moment arm vector.

The pawl load, $P_n$, is the normal force which acts on the wheel and the tangential force is neglected. Equation (11) gives the equation of motion of the ratchet wheel, where the pawl force, $P_n$, is assumed to be known. The input force $P_n$ may be generally expressed in the following form:

$$P_n = K + \sum_{m=1}^{\infty}(f_m\sin mt + g_m\cos mt) \tag{12}$$

where $K$, $f_m$, and $g_m$ are Fourier series coefficients.

The solution of equation (11), may, therefore, be expressed as:

$$\psi = \frac{t^2}{2I_w}[aK - T] + C_1t + C_2 - \frac{a}{I_w}\sum_{m=1}^{\infty}\left(\frac{f_m}{m^2}\sin mt + \frac{g_m}{m^2}\cos mt\right)$$

where $C_1$ and $C_2$ are constants depending on the initial conditions.

Figure 7 shows the angular displacement (equation 13), and the plot of the angular velocity, $\dot{\psi}$, versus time.

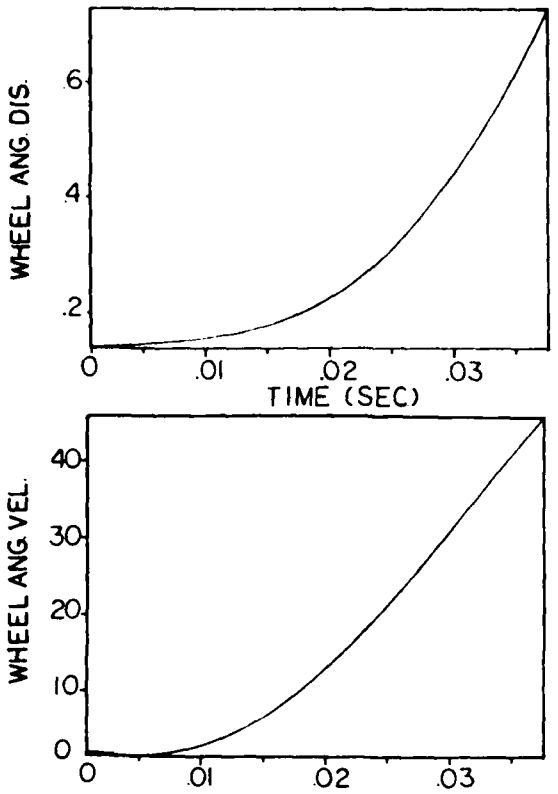


Fig. 7 Motion curves of the ratchet wheel from the classic model

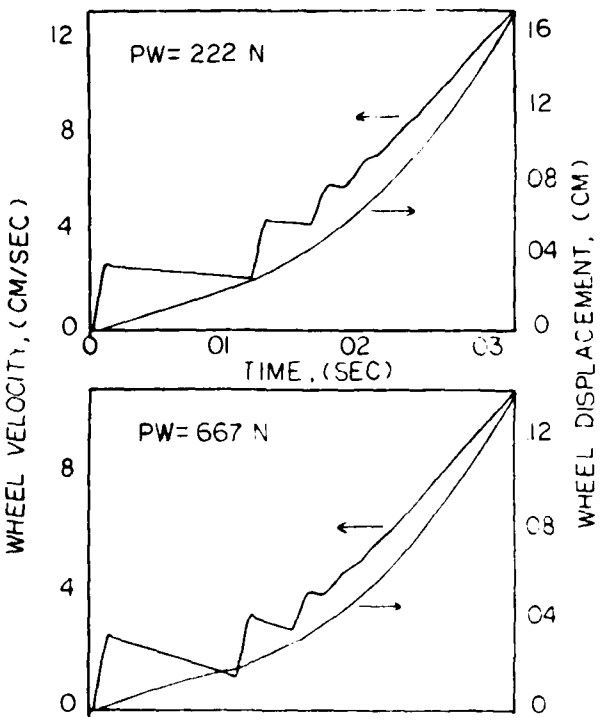


Fig. 8 Motion curves of the ratchet wheel under various loads

*5.2 The Dynamic Model.* The dynamic model presented in Part 1 is applied to ratchets. However, some physical components of the model need to be modified in order to fit the special requirement of ratchets. Again, Fig. 1 of Part 1 can be used as the ratchet model for this investigation. In this model, $M_1$ and $M_2$ represent the equivalent mass of the wheel and the pawl, respectively; $K_c$ represents the equivalent stiffness due to surface compliance and mechanism elasticity of the wheel and the pawl; $D$ represents the damping function which is used to model the system damping; $P_n$ denotes the driving force that the pawl exerts to the wheel, and the constant load, $P_w$, refers to the load applied on the wheel in order to maintain contact between the pawl and the wheel. The driving force, $P_n$ can be expressed as a Fourier series depending on the speciality of the ratchet. The equation of motion of the contact mode can therefore be expressed as

$$M\ddot{X}_c + DX_c + K_cX_c = \left[\frac{M_2}{M_1 + M_2}\right]P_w - \left[\frac{M_1}{M_1 + M_2}\right]P_n \quad (14)$$

where $X_c$ represents the relative displacement between the driving pawl and the wheel.

During the period of noncontact, the equation of motion can be expressed as:

$$\left.\begin{aligned} M_1\ddot{X}_1 &= P_w \\ M_2\ddot{X}_2 &= P_n \end{aligned}\right\} \quad (15)$$

A numerical integration scheme, such as the Runge-Kutta method can be used to yield solution. The following sections give a discussion of the dynamic responses of the ratchet.

**6 Dynamic Responses of Ratchets.** The motion curves of the ratchet wheel vary widely depending upon the means used to power the drive pawl. The input force to drive the wheel can be a spring, a solenoid, a cam or other pulse drive, and therefore each corresponding output motion of the wheel will be different. Some input forces may give a high impact force to the wheel and thus cause losing its control. Therefore, certain additional design refinements are required. In this section, output motions of the ratchet wheel predicted by the dynamic model are presented. The wheel dynamic load is also estimated.

*6.1 The Ratchet Wheel Output Motion.* For numerical experiments the following conditions are used: 1) A periodic forcing function, $P_n = 444.8\ (\sin(80.0t - 1.0) + 1.0)$, is used to drive the system; 2) a viscous damping function based on a given coefficient of restitution of 0.5 is used to represent the system damping; and 3) different wheel loads, $P_w$, are used to study their effects on the wheel output motion. Based on these conditions, the following observations can be made from Fig. 8 which provides the time-displacement and the time-velocity plots of the ratchet wheel.

1 The curves of the wheel displacement and velocity are piecewise nonlinear. This is due to the free-flight mode associated with the contact mode.

2 The dynamic effects of the model can be seen from the wheel displacement and velocity curves, which cause certain distortions of the kinematic profiles of the wheel displacement and velocity (Fig. 7).

3 The wheel velocity increases rapidly at the contact mode and decreases linearly at the free-flight mode referring to Fig. 9. Moreover, a small amount of velocity decrease is observed before the free-flight mode starts. This is due to the effect of the wheel load, $P_w$.

4 The wheel load, $P_w$, has certain effects on the duration of free-flight, the maximum wheel velocity during contact, and the slope of the wheel velocity during the free-flight.

5 The wheel tends to remain in contact with the pawl at the final stage of the working stroke. Therefore, this contributes to a stable increasing of wheel velocity.

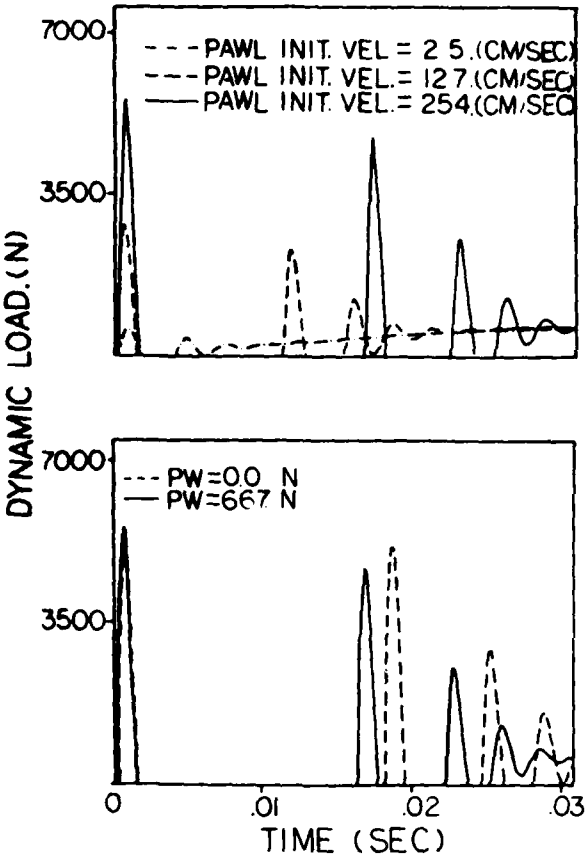


**Fig. 9 The ratchet dynamic loads: (a) the effect of pawl initial velocity; and (b) the effect of wheel load**

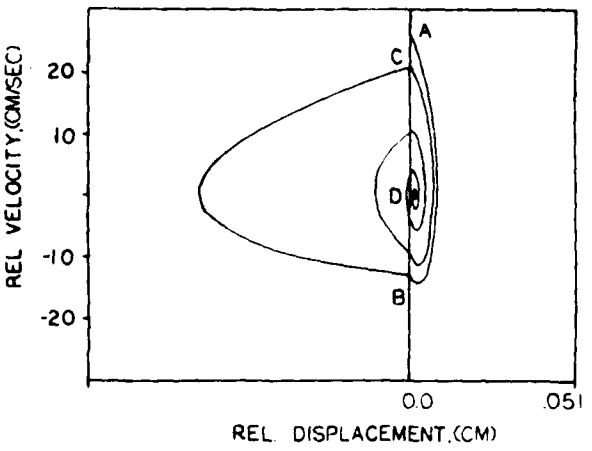


**Fig. 10 Phase-plane plot of the ratchet**

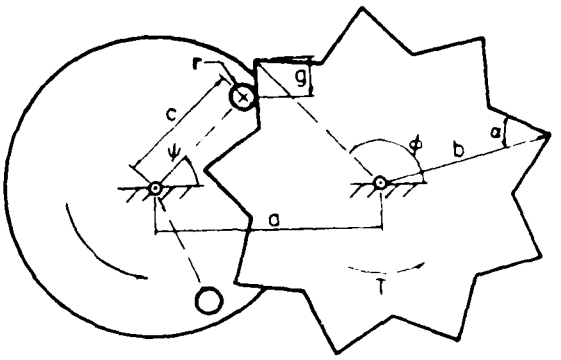


**Fig. 11 The pin pallet runaway escapement mechanism**

From the foregoing observations, it is found that the wheel motion is generally instable at the beginning stage of the working stage and is stable at the middle and final stages of the working stroke.

*6.2 Ratchet Wheel Dynamic Load.* The dynamic load of ratchet between wheel and pawl is important and is of practical concern. Our discussion here includes: 1) the effect of initial velocity on the dynamic load of ratchet mechanism, and 2) the effect of the wheel load, $P_w$, on the dynamic load of the ratchet mechanism. Each of these effects is discussed in the following.

1 Using different pawl initial velocities, the dynamic loads calculated numerically from equation (7) are shown in Fig. 9(*a*). It is found that the dynamic load is affected significantly by the pawl's initial velocity at the initial stage of the working stroke. The higher the pawl's initial velocity, the higher the dynamic load as well as the longer the duration of the free-flight mode. Therefore it may be advantageous if the initial velocity of the pawl is set low in order to minimize the dynamic load on the ratchet wheel.

2 The ratchet wheel dynamic loads predicted from different wheel loads, $P_w$, are plotted in Fig. 9(*b*). It is interesting to find that the higher the wheel load, $P_w$, the shorter the duration of the free-flight mode and there appears to be no increase on the dynamic load. Especially, at the end of the working stroke, the higher the wheel load, $P_w$, the shorter the duration of the free-flight mode and a lower dynamic load.

*6.3 The Phase-Plane Plot.* The phase-plane plot of the motion of the ratchet is given in Fig. 10. The plot starts from the point *A* of the contact mode with a pawl initial velocity 0.25 m/s. During the first contact stage, the pawl speed changes from 0.25 to −0.12 m/s. At point *B*, a free-flight mode is followed and impact then occurs at point *C*. Finally, the pawl reaches point *D*. From the phase-plane plot, certain conclusions can be made.

1 The classic definition of the coefficient of restitution may be quantitatively evaluated using the phase-plane plot. For instance, the relative velocity at points *A* and *B* are 0.25 m/s and −0.12 m/s, respectively. This, therefore, gives a coefficient of restitution of 0.5 for the impact of the ratchet.

2 The curvature of the phase-plane plot changes rapidly within the contact stage near point *B*. This is due to the wheel load, $P_w$, which extends the duration of contact. Consequently, the pawl speed is increased before the separation of pawl and wheel.

3 In the free-flight mode, the pawl speed starts from −0.12 m/s and increases up to 0.2 m/s at point *C*. The change of the pawl speed depends upon: 1) the speed at point *B*, and 2) the pawl force, $P_n$.

4 The relative velocity at the terminal position of the pin stroke, point *D*, reaches a value of approximately zero. This demonstrates that the damping function is effective and it therefore essentially stabilizes the vibration between the pawl and the wheel at the final stage of the working stroke.

## Escapement Mechanisms

**7 Introduction to Escapements.** Escapement is a mechanism or device which is designed to alternately grab and release a rotating shaft, wheel, slide, etc. [6]. In general, it can be classified into three types according to its functions and the manners of its operation. These types are: the watch

escapement, the machine escapement, and the inverse escapement. They usually belong to a class of mechanisms designed for particular purposes, e.g., a time keeper, or as a mechanical controller of a rotating shaft, or as a ratchet performing similar or better functions. Most of the escapements are very simple kinematically; they are low-cost, rugged, and reliable. The mechanism offers many uses [6, 7]. They are used in clocks and watches, bomb fuses, typewriter composer systems, counters, precision stepping drives, etc.

In the design of escapements, certain general functional requirements of these mechanisms must be considered. Some of the requirements are: 1) stability; the escapement has to be fast and capable of operating at high speeds. For instance the IBM selectric composer requires four thousandths of a second to reach its maximum displacement [8]. Besides being fast, it must be positive and reliable, and have minimum rebound at the end of an escapement cycle. 2) Minimum impact force; in order to design the parts for adequate strength, the extreme impact force must be determined; and 3) a predictable controlled escapement time.

Since the function of the escapement depends highly on the preciseness of its motion, usually involving high speed operation, therefore, an investigation of the dynamics of the escapement is necessary. There are, however, not many investigations on the record [8, 9]. Lowen and Tepper [9] did a thoughtful, and believed to be the first of its kind, investigation on the dynamics of the pin pallet runaway escapement. In their formulations, rigid body and momentum balance approaches are used. In addition, the classic coefficient of restitution was employed to formulate the impact phenomena. It is thought worthwhile, in this investigation to apply the general dynamic model of the intermittent-motion mechanism developed in Part 1 to the escapement mechanism. In our model, system damping and material compliance are included. A comparative study with the results reported in [9] on the dynamic responses and motion characteristics is performed.

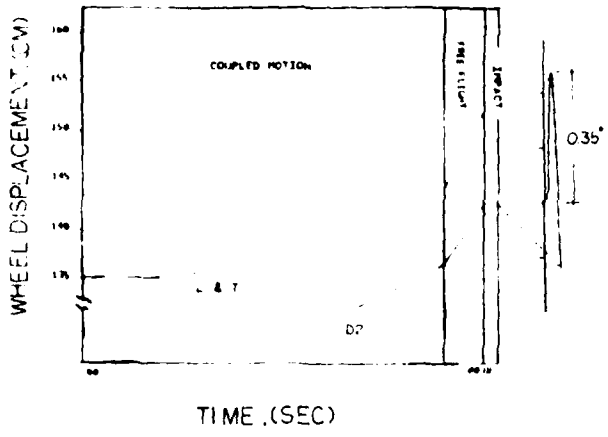


Fig. 12 Angular displacement of the escape wheel

**8 Dynamic Responses of the Escapement.** In this paper, a watch escapement shown in Fig. 11 is investigated. The kinematics of the mechanism and a useful computer program have been developed in [9].

The dynamics of the mechanism involves three stages. These are: 1) The coupled motion: In this phase, the escape wheel is driven by a constant torque in the positive direction of rotation. 2) The free motion: This stage follows the end of the coupled motion or when separation of contact occurs after

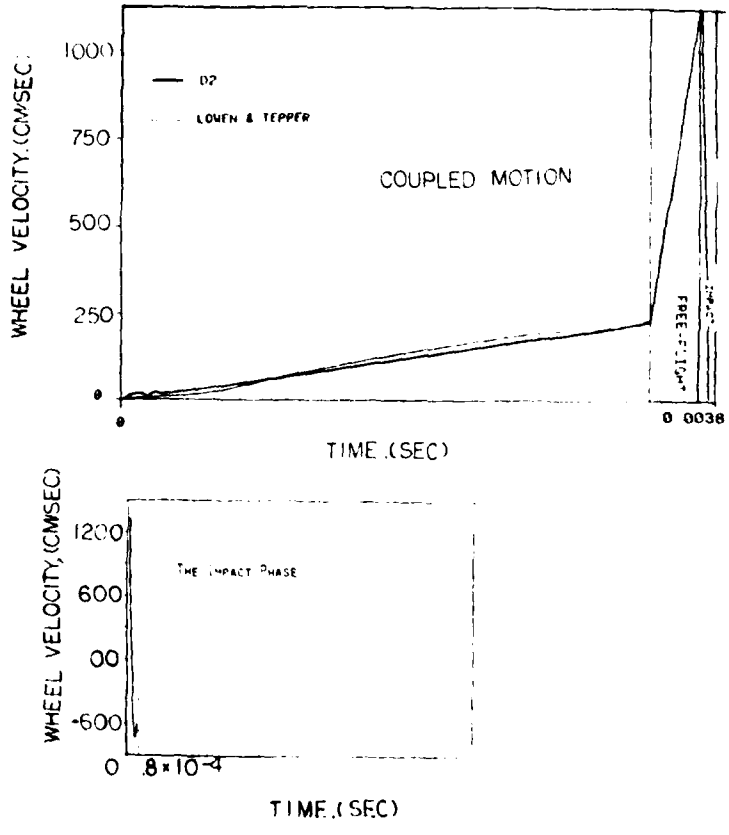


Fig. 13 Angular velocity of the escape wheel

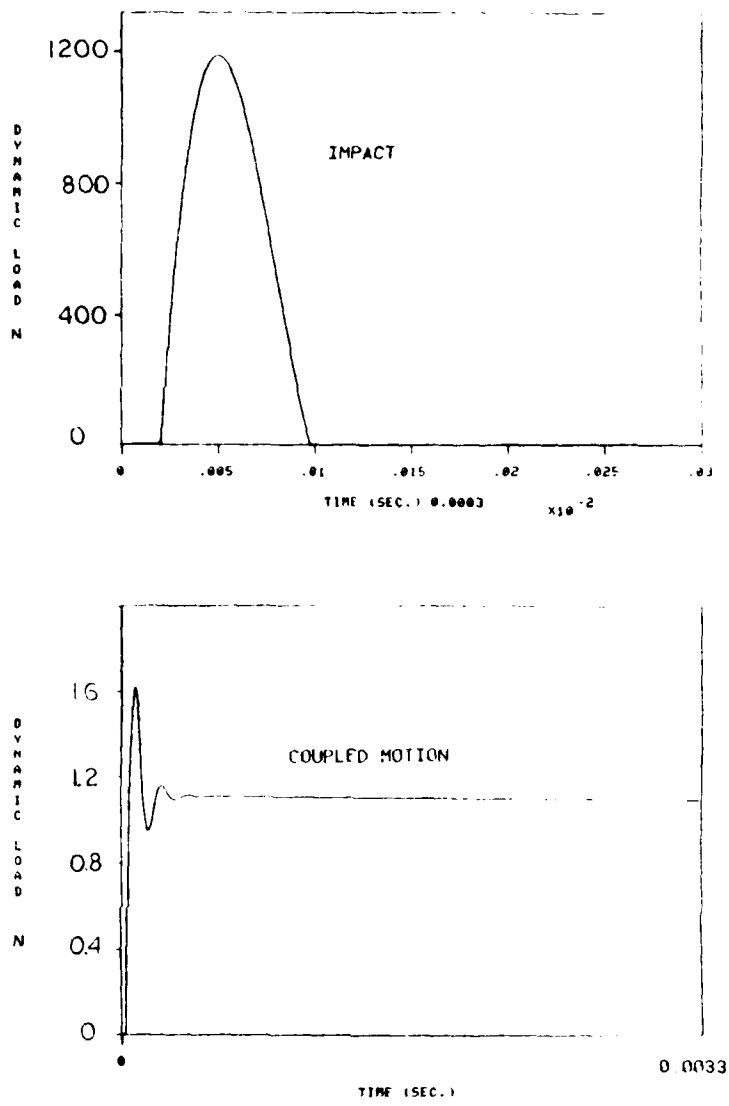


Fig. 14 Dynamic load of the escapement mechanism

the stage of impact. In this phase, the wheel and the pallet move independently of each other in free motion where the motion of the pallet depends only on its initial conditions. 3) The impact stage: This stage follows free motion and usually involves a reversal of the motion of the pallet. Under certain circumstances, temporary motion reversal of the wheel is also possible.

In this investigation, the first two stages of the motion follow essentially the formulations of [9]. In the important stage of the impact, however, our dynamic model is applied.

Referring to Fig. 1 of Part I, $M_1$ and $M_2$ denote the equivalent masses of the escape wheel (the driver) and the pallet, respectively. The driving force, $P$, is calculated from the given torque with variable moment arms. Following [9], a coefficient of restitution equal to 0.3 is used.

The initial conditions for the numerical experiments are specified as follows:

relative initial displacement = 0.0
relative initial velocity = 0.0
initial driving force = 1.53 N
} The coupled motion stage

relative initial displacement = 0.0
relative initial velocity = 1.55 m/s
} The impact stage

Dynamic responses of both the pallet and the wheel are given in the following sections.

*8.1 Motion Characteristics of the Escapement.* Figures 12 and 13 give the output angular displacement and velocity curves, respectively, of the escape wheel. A comparative study with the result of Lowen and Tepper [8] is also shown. We discuss separately the following two motion stages.

1 The Coupled Motion

The displacement predicted by this model and the one in [8] agree well. However, if the relative velocity between the pallet and the wheel increases, dynamic effects due to system damping as well as material compliance will be significant. In that case, the deviation between the two approaches would be observable.

The velocity of the wheel is found to be oscillating during the initial stage. This is due to the sudden application of the driving load and this oscillation dies out as the time progresses. Figure 13(*b*) shows an enlargement of the com

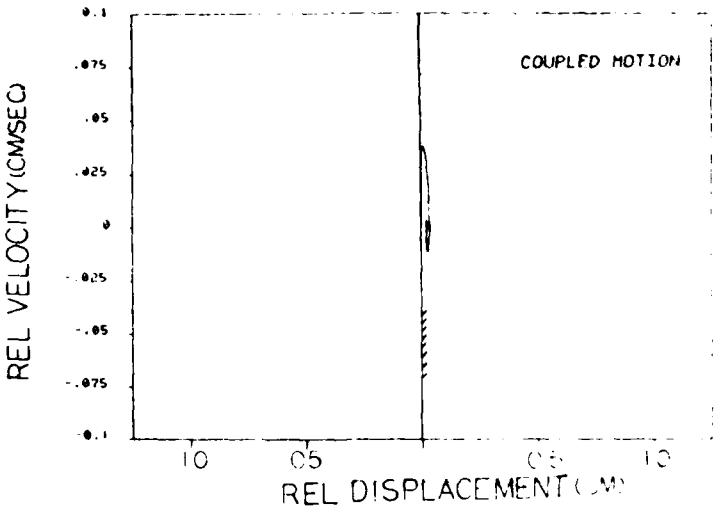


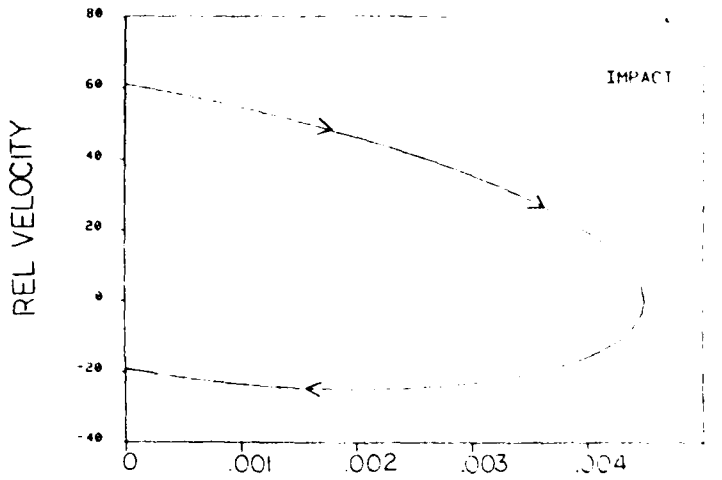


**Fig. 15 Phase-plane plots of the escapement mechanism**

parison of the result of this investigation with that of [9]. Besides oscillations, there is general agreement on the velocity curve in this stage of motion.

2 The Impact Stage

The output displacement curve shows a significant decrease of displacement due to impact. This agrees with our physical intuition. The time duration of impact is calculated to be 80 $\mu$s which accounts for about 3 percent of the total coupled motion duration. This time cannot be estimated with the approach of [9] and consequently it was neglected. Figure 13(*b*) shows there is a sudden oscillation in the velocity curve, and a decrease of velocity as a result of the impact phenomena.

*8.2 The Escape Wheel Dynamic Load.* The dynamic load between the escape wheel and the pallet has a significant effect on the motion, the wear, and fatigue of the parts. Figure 14 gives the dynamic load during the coupled motion as well as the impact motion. The following conclusions can be drawn.

1) The dynamic load during the coupled motion is found to be of no major concern since it appears to be low. The maximum dynamic load is only 1.78 N; the load reaches a final value of 1.22 N.

2) The dynamic load during the impact stage, on the other hand, is significant. The maximum value is 756.2 N which would be the main source causing severe vibrations to the wheel and the pallet.

*8.3 The Phase-Plane Plot.* Figure 15 shows the phase-plane plot of the escapement. We have the following observations.

1 During the coupled motion, the graph shows that the limit cycle is small and vanishes immediately after a few cycles. No bounce has been observed.

2 The phase-plane plot of the impact stage is unstable. This is because the relative velocity during impact is large. A significant bounce follows immediately after the impact.

## Conclusion

The dynamic responses of Geneva mechanisms, ratchets, and escapements have been analyzed. It is shown that the proposed dynamic model and its associated damping function approach exhibits a variety of dynamic characteristics which are believed to be representative of intermittent-motion mechanism. The dynamic load, obtained using the present approach, is an important factor for the stress analysis and the design of these mechanisms.

## Acknowledgment

The authors are grateful to the Army Research office for the support of this research through contract DAAG29-81-K-0016 to Rutgers University.

## References

1 Lee, T. W., Wang, A. C., and Niderost, G. R., "On the Dynamics and Stress Analysis of Intermittent Motion Mechanisms," *Transactions of the Twenty-Seventh Conference of Army Mathematicians*, ARO Report 82-1, pp. 401-431.

2 Fenton, R. G., "Dynamic Analysis of Geneva Mechanisms," *Machine Design*, Vol. 37, No. 2, 1965, pp. 177-182.

3 Dichwitz, O., "Mechanism of Intermittent Motion," *Machine Design*, Vol. 23, No. 12, Dec. 1951, pp. 136-145; Vol. 24, No. 1, 1952, pp. 127-141; Vol. 24, No. 2, 1952, pp. 146-155; Vol. 24, No. 3, 1952, pp. 147-155.

4 Lee, T. W., "Optimization of High Speed Geneva Mechanisms," ASME *Journal of Mechanical Design*, July 1981, Vol. 103, pp. 621-630.

5 Lee, T. W., and Wang, A. C., "On the Dynamics of the Intermittent Motion Mechanisms Part I: Dynamic Model and Response," this issue ASME JOURNAL OF MECHANISMS, TRANSMISSIONS, AND AUTOMATION IN DESIGN, pp. 534-540.

6 Bickford, J. H., *Mechanisms for Intermittent Motion*, Industrial Press, Inc., New York, 1972.

7 Chironis, N. P., *Mechanisms, Linkages, and Mechanical Controls*, McGraw Hill, New York, 1965.

8 Miles, B. W., and Wilson, C. C., "The IBM Selectric Composer Proportional Escapement Mechanism," *IBM Journal of R&D*, Vol. 12, Jan. 1968, pp. 48-59.

9 Towen, G. G., and Tepper, F. R., "Dynamics of the Pin Pallet Runaway Escapement," Technical Report ARLCD-TR-77062, U.S. Army Armament Research and Development Command, Dover, N.J., June 1978.

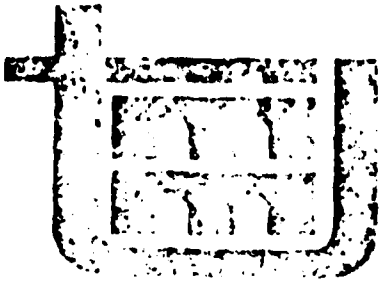

PROCEEDINGS OF THE
SIXTH WORLD CONGRESS ON

# THE THEORY OF MACHINES AND MECHANISMS

DECEMBER 15-20, 1983, NEW DELHI, INDIA

VOLUME I

EDITORS
J.S. RAO
K.N. GUPTA

WILEY EASTERN LIMITED
New Delhi Bangalore Bombay Calcutta

Proceedings of the Sixth World Congress on Theory of Machines and Mechanisms, 1983

# On the kinematic synthesis of dwell mechanisms

WANG, A.C.
Mechanical Engineering Department
Rutgers University
New Brunswick, NJ 08903
U.S.A.

LEE, T.W.
Mechanical Engineering Department
Rutgers University
New Brunswick, NJ 08903
U.S.A.

SYNOPSIS This paper presents a general approach for the kinematic synthesis of momentary-dwell mechanisms. The approach involves using the solution of first-order dwell criterion as an initial estimate and the development of a computer-aided procedure to subsequently readjust the mechanism proportions for a closer match to other dwell criteria by optimization. The proportions thus obtained provide an approximation of the high orders of dwell and, for most practical purposes, the solution is useful and acceptable. An example of a six-bar linkage is used to illustrate this approach.

## INTRODUCTION

1. Dwell mechanisms are important for their many uses such as in machine tools, packaging and textile machinery. Basically, there are two types. One gives a finite dwell, such as the standard external Geneva mechanism; the other provides instantaneous or momentary dwell. The latter can be used for performing functions while machining is in motion, for example in flying shears, labeling, closing of cans, etc. The fundamental difference between these two types lies in the output motion. Mathematically, the displacement function for the finite-dwell mechanism is a constant within a defined dwell region. Therefore, the higher order derivatives of the motion such as velocity, acceleration, and shock are zero within this region. In addition to these, at the boundary of starting or ending of a finite-dwell, the motion are generally discontinuous. For the motion of the momentary-dwell mechanism, the displacement is a nonlinear function of time or input angle. The higher order derivatives of motion generally do not equal to zero, and equal or close to zero only at an instant, i.e., the point of dwell. Furthermore, the motion curves are continuous, therefore there is no exact boundary of starting or ending of a momentary-dwell. Physically, the finite-dwell mechanism is stopped to have dwell by a locking device, such as at the Geneva mechanism the locking position of the crank can stop the wheel from moving. On the contrary, momentary-dwell mechanism does not depend on any locking device to have dwell.

2. Because of this basic difference on motion between the two types of intermittent-motion mechanisms, the synthesis methods on these mechanisms, therefore differ. In the synthesis of finite-dwell mechanisms, much emphasis is on the minimization of shock, i.e., on the improvement of the kinematic and dynamic characteristics of the mechanism for longer life and higher speeds of operation. There have been many thoughtful investigations in this respect, and a summary of them can be found in [1,2].

3. Of particular interest in this investigation is on the kinematic synthesis of the momentary-dwell type of mechanisms. The purpose is to develop analytical and computer-aided procedure on the synthesis of mechanisms with prescribed dwell characteristics. The importance is on the design of dwell mechanisms which can possess higher orders of dwell at one or more instants during the motion cycle. The development of design methods in this regard, however, has not been easy. One primary reason is that the motion of momentary-dwell mechanism is usually an algebraic equation of high order, having coefficents which are nonlinear functions of mechanism parameters. Dwell occurs due to the cancellation of relative motions of one part of the mechanism with respect to the other. Since the momentary-dwell mechanism is usually made of compound mechanisms (i.e., the combination of two or more simple mechanisms) whose motion characteristics are generally not readily known, the derivation of an explicit motion expression in terms of design parameters and, subsequently, finding its solution can be difficult.

4. There have been several investigations on the kinematic synthesis of momentary dwell mechanisms and most of them involving analytical treatment [3,4]. As the complexity of the mechanism grows higher, algebraic methods of synthesis become more difficult to develop in order to satisfy precisely the dwell characteristics. On the other hand, for most practical purposes, high order dwell criteria need not to be satisfied exactly and they can be met approximately. The following represents an attempt to develop an approach for the approximate synthesis of momentary-dwell mechanisms.

BASIC APPROACH

. . A general approach for the kinematic synthesis of mo entary-dwell mechanisms is presented. The method involves using the solution of first-order dwell criterion as an initial . stimate and the development of a computer-aided procedure to subsequently readjust the mechanism proportions for a closer match to other dwell riteria by optimization. The proportions thus btained provide an approxination to high order dwells and, for most practical purposes, the solution is useful and acceptable.

.. The computer-aided synthesis procedure is based on an effective optimization algorithm, namely, the HOT code (Heuristic Optimization echnique of Lee and Freudenstein [5]) to reach solution.

7 To illustrate this basic approach, the inematic synthesis of a six-bar dwell linkage s presented. In the following, we begin with an analytical investigation on the motion characteristics of the mechanism. The kinematic nthesis of the mechanism with prescribed dwell haracteristics follows. It is found that the first-order dwell criterion is a second-order quation in terms of the half-tangent of the out- it angle and its solution can be readily obtained alytically. As for the second- and high-order dwells, numerical solution involving optimization comes essential. This example, therefore, monstrates the potential usefulness of the pproach.

Displacement Analysis

.. A six-bar dwell linkage [6], shown in its schematic view in Fig. 1, consists of six links denoted as $r_1$, $r_2$, $r_3$, $r_4$, $r_5$, and $r_6$. The in- t is usually a continuous rotary motion which is applied to link $r_2$ and $\theta_1$ refers to as the input displacement angle. The output shaft, entered at the pivot G, would then provide a momentary dwell motion if the linkage is properly proportioned.

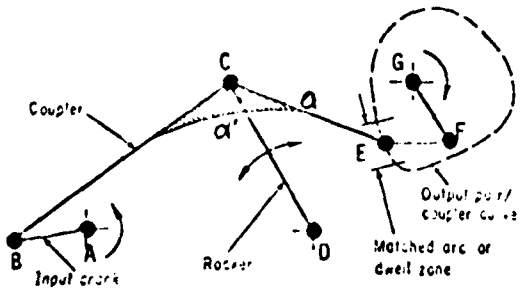


Fig. 1

Ten design parameters are required. These are six link lengths; the coupler bent angle, a'; the extended coupler length, a; and the position parameters of the output crank, namely, the inclination angle and the fixed distance between the rocker pivot and the output pivot, θ and b, respectively.

9. The motion of the pivot point between two couplers ABCE and EF is of major concern. The couplers point, E, traces an essentially oval-shaped path. This path generally has high-order curvature, and therefore, its corresponding radius is not a constant. However, if dimensions of the mechanisms are so designed that the radius of the curvature of the point E is equal or close to a constant during certain range of the motion cycle, and if the link length $r_6$ is made equal to this instantaneous radius of curvature, then the output crank, $r_6$, has momentary dwell. In the following, we first begin with the motion of a four-bar coupler point.

10. Referring to Fig. 2, the position of the coupler point E can be expressed as

$$\bar{r}_E = (1-\lambda)\bar{r}_B + \lambda\bar{r}_C \qquad (1)$$

where

$$\bar{r}_E = \overline{AE},\ \bar{r}_B = \overline{AB},\ \bar{r}_C = \overline{AC} \text{ and } \lambda = \frac{l}{r_3} e^{i\alpha}$$

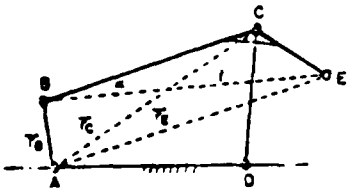


Fig. 2

Rearranging eq. (1), we have the position of the coupler point E in the Cartesian coordinate system,

$$X_E = X_B + \frac{l}{r_3}\cos\alpha(X_C-X_B) + \frac{l}{r_3}\sin\alpha(Y_C-Y_B)$$

$$X_E = Y_B + \frac{l}{r_3}\cos\alpha(Y_C-Y_B) - \frac{l}{r_3}\sin\alpha(X_C-X_B) \qquad (2)$$

where

$$X_B = r_2\cos\theta_1 \qquad X_C = r_4\cos\theta_2 + r_1$$
$$Y_B = r_2\sin\theta_1 \qquad Y_C = r_4\sin\theta_2 \qquad (3)$$

The velocity, acceleration and shock equations of the coupler point E can be easily derived by differentiating equations (2) and (3).

11. Two forms of the displacement equation of the six-bar linkage can be derived. One which is derived from an inverted mechanism (Fig. 3) is explicit in terms of the coordinates of the floating pivot, F, of the output crank; the other is an angular displacement equation relating the input and output angular relationship. We give the results of derivation as follows:

$$A_0X_F + B_0Y_F = C_0 \qquad (4)$$

where

$$A_0 = 2[R_1\cos(\theta_1-\alpha)-R_2\cos(\theta_2-\alpha)+r_2]$$

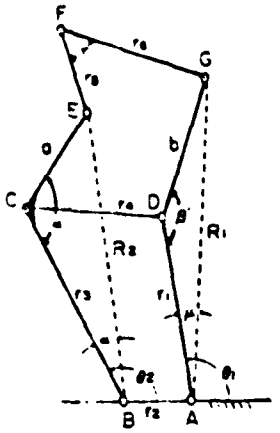


Fig. 3

$$B_0 = 2[R_1\sin(\theta_1-u)-R_2\sin(\theta_2-a)]$$
$$C_0 = R_1^2-R_2^2+r_2^2+r_5^2-r_6^2+2R_1r_2\cos(\theta_1-u)$$

and

$$A\sin\psi + B\cos\psi + C = 0 \qquad (5)$$

where

$$A = Y_E-Y_G$$
$$B = X_E-X_G$$
$$C = -(A^2+B^2+r_6^2-r_5^2)/(2r_6)$$

Equation (5) can also be rewritten in terms of the half-tangent form of $\psi$

$$\psi^+ = 2\tan^{-1}\left[\frac{A+\sqrt{A^2+B^2-C^2}}{B-C}\right]$$

and (7)

$$\psi^- = 2\tan^{-1}\left[\frac{A-\sqrt{A^2+B^2-C^2}}{B-C}\right]$$

These two solutions of eq. (6) correspond to two different configurations of a six-bar linkage. It is worth noting that the displacement equations, eq. (4) and eq. (5) have similar form. For the study of high-order motion analysis, the latter is chosen, since algebraically, it is more convenient to handle.

## Dwell Criteria

12. In a momentary dwell mechanism, the dwell is defined when the first or second derivative of the output motion with respect to the input motion vanishes at an instant. The order of the consecutive derivatives which are zero at that instant refers to the degree or order of dwell. In the following the dwell criteria for the first-order is derived. Criteria for higher orders can be derived in a similar manner. The definition of the first-order dwell is the existence of the velocity ratio which reduces to zero at an instant and the satisfaction of the displacement eq. (5), i.e.,

$$A'\sin\psi + B'\cos\psi + C' = 0 \qquad (8)$$

$$A\sin\psi + B\cos\psi + C = 0 \qquad (9)$$

where

$$A' = Y_E' \qquad A = Y_E-Y_G$$
$$B' = X_E' \qquad B = X_E-X_G$$
$$C = \frac{-(AA'+BB')}{r_6} \qquad C = \frac{-(A^2+B^2+r_6^2-r_5^2)}{2r_6}$$

For the first-order dwell, eq. (8) and (9) should be satisfied simultaneously. The solution is:

$$\sin\psi_D = \frac{C'B-B'C}{AB'-BA'}$$
$$\cos\psi_D = \frac{A'C-C'A}{AB'-BA'} \qquad (10)$$

For the first-order dwell, eq. (10) should always be satisfied. It can be seen that the motion characteristics of the coupler point, E and link length $r_5$ and $r_6$ play important roles in the first-order dwell.

## KINEMATIC SYNTHESIS

13. In the previous sections, motion equations and criteria of dwell have been developed. These equations are nonlinear and need to be solved simultaneously. Analytical solution is possible only for the velocity dwell and generally is not possible for higher order dwell. Therefore the kinematic synthesis with prescribed high-order dwell characteristics becomes a rather tedious and involved task in which numerical approach is essential. The synthesis procedure of the six-bar linkage with prescribed dwell involves the determination of ten design parameters, and the satisfaction of specified dwell conditions. These design parameters include six link lengths, ($r_1$, $r_2$, $r_3$, $r_4$, $r_5$, and $r_6$), two extended coupler lengths (a and b), one coupler angle ($a'$), and one position angle ($e$).

14. Generally, in the case of first-, second-, and third-order dwells, there are fewer equations than the number of parameters to be determined. For instance, for the third-order dwell, there are four conditions including one displacement equation and three dwell equations. Additional specifications from the designer, therefore, are necessary. In the following, we first introduce a rotatability criterion of the six-bar linkage, which will define the feasible range of design parameters of the mechanism. Then, a method of analytical synthesis for the first-order dwell is introduced. Two design parameters ($r_5$ and $r_6$) can be specified throughout the synthesis procedure. For higher order dwells, solution of dwell equa-

tions explicit in design parameters is difficult to obtain. Therefore, a numerical synthesis procedure up to the third-order dwell is presented. The procedure combines a method of analytical synthesis with an optimum design technique, i.e., the HOT algorithm [5]. In the following section we begin with a discussion on the rotatability criteria of the six-bar dwell linkage.

Rotatability Criterion

15. The rotatability study of a six-bar linkage uses the well-known Grashof criterion. Referring to Fig. 4, the six-bar linkage is a compound linkage consisting of a four-bar linkage and a double-crank. It is desirable that the four-bar linkage is of the crank-rocker type. The rotatability study involves the following two stages:

1) Rotatability of the input crank

Grashof criterion can be used directly, we have

$$\ell + s < P+Q \tag{11}$$

where $\ell$ and $s$ represent the longest and the shortest link, respectively; the intermediate links are denoted as P and Q.

For a crank-rocker linkage, S must be the crank and the frame being either one of the adjacent links.

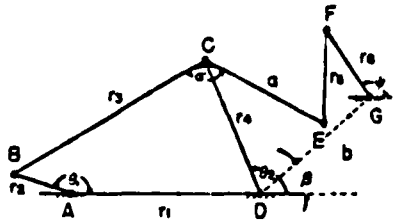


Fig. 4

) Rotatability of the output crank

This concerns the links $r_5$, $r_6$ and $r_G$ and a ariable length $r_6$ which is the distance between oints O and E. Referring to eq.(9), we must have

$$A^2 + B^2 > C^2 \tag{12}$$

ere

$$C = -(A^2+B^2+r_6^2-r_5^2)/(2r_6)$$

tting $d = \sqrt{A^2+B^2}$ we have

$$d > C$$

d

$$(d+r_6) > r_5 \tag{14}$$

uation (14) obviously holds from the argument that $r_5$, $r_6$ and d form a triangle. In addition, we can write

$$r_5 + r_6 > d \tag{15}$$

and

$$r_5 + d > r_6 \tag{16}$$

Equations (13), (14), (15), and (16), therefore, are the rotatability criteria of the output crank. Since the parameter d depends on the motion of the coupler point E, the coupler curve of point E plays an important role on the synthesis of the output cranks $r_5$ and $r_6$.

Transmission-Angle Characteristics

16. The transmission angle of the six-bar linkage is denoted as the smaller angle between links $r_5$ and $r_6$ (Fig. 3). The transmission-angle behavior of the six-bar linkage differs from that of the slider-crank and four-bar mechanism, therefore, it warrants an investigation. The transmission angle $\tau$ is

$$\cos\tau = (r_5^2+r_6^2-d^2)/(2r_5r_6) \tag{17}$$

where

$$\begin{aligned} d &= |EG| = \sqrt{(X_E-X_G)^2+(Y_E-Y_G)^2} \\ X_E &= R_2\cos(\phi_2-\alpha) \\ Y_E &= R_2\sin(\phi_2-\alpha) \\ X_G &= R_1\cos(\phi_1-\mu) + r_2 \\ Y_G &= R_1\sin(\theta_1-\mu) \end{aligned} \tag{18}$$

or

$$\cos\tau = \frac{(R_1^2+R_2^2+r_2^2-r_5^2-r_6^2)-2R_1R_2\cos(\theta_2-\theta_1-\alpha+\mu)}{-2r_5r_6} - \frac{r_2[R_1\cos(\theta_1-\mu)-R_2\cos(\theta_2-\alpha)]}{r_5\,r_6} \tag{19}$$

Equation (19) gives the transmission angle. It is desirable that the maximum variation of this angle from the right angle on the entire motion be minimized.

Analytical Synthesis

17. The analytical synthesis of a six-bar linkage with velocity dwell is introduced in this section. The result provides explicit expression of $r_5$ and $r_6$ in terms of other design parameters. The velocity dwell equations are from eqs. (8) and (9)

$$A'\sin\psi + B'\cos\psi + C' = 0$$

$$A\sin\psi + B\cos\psi + C = 0$$

where

$$A = Y_E-Y_G$$

$$B = X_E\,X_G$$

$$C = -(A^2+B^2+r_6^2-r_5^2)/2r_6$$

$$A' = Y_E'$$

$$B' = X_E'$$

$$C' = -(AA'+BB')/r_6$$

Solving for $r_5$ and $r_6$, we have

$$r_5 = \sqrt{A^2+B^2+\left(\frac{A'A+B'B}{A'\sin\psi+B'\cos\psi}\right)\left[\left(\frac{A'A+B'B}{A'\sin\psi+B'\cos\psi}\right) - (A\sin\psi+B\cos\psi)\right]} \qquad (20)$$

$$r_6 = (A'A+B'B)/(A'\sin\psi+B'\cos\psi) \qquad (21)$$

The Optimization Problem

18. Using the analysis developed before, it is possible to optimize the kinematic design of the six-bar linkage for higher-order dwell by a proper choice of the geometric parameters. The design problem can now be converted to an optimization problem as follows for dwell up to the third order:

$$\text{Minimize: } f = W_1E_1 + W_2E_2 + W_3E_3 \qquad (22)$$

Subject to:
(a) dimensional constraints on design parameters
(b) Constrains on entire-motion characteristics, such as rotatability, transmission-angle characteristics, limits on velocity fluctuations, etc.

In eq. (22), f represents the objective function; $W_1$, $W_2$, and $W_3$ are weighting factors chosen by the designer depending on design applications; $E_1$, $E_2$, and $E_3$ denote as the error functions corresponding to the deviation of dwell positions of the velocity acceleration and shock, respectively, and are given as follows

$$E_1 = |\psi_D-\psi_{2D}|; \quad E_2 = |\psi_D-\psi_{3D}|; \quad E_3 = |\psi_D-\psi_{4D}|$$

wehere

$$\psi_D = \frac{A_1+\sqrt{A_1^2+B_1^2-C_1^2}}{B_1-C_1} \quad \text{and} \quad \psi_{iD} = \frac{A_i+\sqrt{A_i^2+B_i^2-C_i^2}}{B_i-C_i},$$

$$i = 2,3,4.$$

Many optimization techniques are available and can be used for this application. However, because of its efficiency, the HOT code is used. A computer program for optimum design of the six-bar linkage for higher orders of dwell was developed. The program was written in FORTRAN IV language.

Example. Design of a six-bar linkage. The mechanism dwells when the input crank angle is between 3 to 5 radians, and the following four-bar proportions have been specified:

$r_1 = 3.0$ cm, $r_2 = 1.0$ cm, $r_3 = 3.6$ cm, $r_4 = 2.5$ cm, $a = 2.2$ cm, $b = 2.4$ cm, $\alpha' = 130°$ and $\beta = 40°$.

Solution: The design stages are given in the following.
1. Analytical synthesis procedure. Equations (20) and (21) give $r_5 = 1.75$ cm and $r_6 = 1.75$ cm. With this set of design parameters, the first-order dwell is ensured.
2. The optimum synthesis procedure using HOT gives the solution set as follows: $r_1 = 2.98$ cm, $r_2 = 0.98$ cm, $r_3 = 3.62$ cm, $r_4 = 2.32$ cm, $r_5 = 1.7$ cm, $r_6 = 1.8$ cm, $a = 2.2$ cm, $b = 2.4$ cm, $\alpha' = 124°$ and $\beta = 41.4°$.
This set of design parameters will provide an approximate third-order dwell. Motion characteristics of the linkage are shown in Fig. 5.

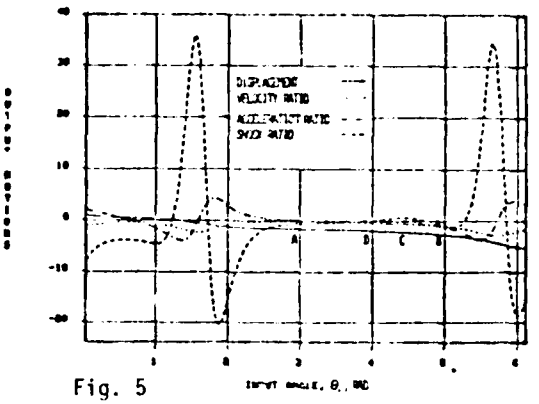


Fig. 5

ACKNOWLEDGEMENT

The authors are grateful to the Army Research Office for the support of this research through Contract DAAG29-81-K-0016 to Rutgers University.

REFERENCES

1. BICKFORD, J.H. Mechanisms for Intermittent Motion, Industrial Press, N.Y., N.Y., 1972.
2. LEE, T.W. AND WANG, A.C. On the Dynamics of Intermittent-Motion Mechanisms, Parts 1 & 2, ASME Paper 82-DET-64 and 65, to appear in Journal of Mechanical Design.
3. LEE, T.W. AND SHERESHEVSKY, Y. Kinematic Synthesis of Planar Two-Gear Drives with Prescribed Dwell Characteristics, ASME Journal of Mechanical Design, Oct. 1982, pp. 687-697.
4. LEE, T.W. AND AKBIL, E. Kinematic Synthesis of Spherical Two-Gear Drives with Prescribed Entire-Motion Characteristics, Part 1: Displacement Analysis and Dwell Characteristics, ASME Paper 82-DET-124, to appear in Journal of Mechanical Design.
5. LEE, T.W. AND FREUDENSTEIN, F. Heuristic Combinatorial Optimization in the Kinematic Design of Mechanisms, Parts 1 & 2, ASME Journal of Engineering for Industry, Nov. 1976, pp. 1277-1284.
6. Machine Design, Dec. 8, 1966, p. 194.

# Automated Dynamic Analysis of Chain-Driven Mechanical Systems

**Ting W. Lee**
Associate Professor,
Department of Mechanical and Aerospace Engineering,
Rutgers University,
New Brunswick, N.J. 08903

*A general approach to analyze the dynamics of chain-driven systems subjected to transient loads is developed and applied. The method suitable for many automated dynamic analysis techniques involves the simulation of the dynamic effect of chain by a displacement function and the introduction of this function as a kinematic constraint to couple with the system equations of motion. A general purpose dynamic analysis algorithm, the DADS code (Dynamic Analysis and Design Systems), is then employed to generate the set of system equations and to provide a computer-aided dynamic analysis of the overall chain-driven system. Two ways of formulating the chain displacement functions are described. One provides the displacement of the chain based on the pitch circles of chain sprockets; the other includes a consideration of the polygonal effect of the chain which contributes essentially to the dynamics of the chain. The latter involves the use of the principle of kinematic equivalency, i.e., modeling the chain dynamic effect by a four-bar linkage. Using the proposed displacement function, the kinematic motion of the chain can be taken into account. This procedure, therefore, makes the system adaptable to conventional dynamic analysis code in which the chain is usually not included as one of the standard elements. Moreover, pulsation and dynamic load of the chain as well as the system dynamic response due to chain effect may be estimated. A typical large-scale chain-driven system which is an externally powered machine gun is investigated to illustrate the potential usefulness of the approach.*

## 1 Introduction

Dynamic analysis of any mechanical system of realistic complexity is not a simple task. These systems usually involve a large number of mechanical components, such as gears, shafts, springs, cams, linkages, etc., and the interactions between components are nonlinear. In addition, loading and operational speed may impose additional complexities, i.e., the presence of discontinuous forces, mass, velocities, and potential energies, which characterize the intermittent motion and inertia loading from the high speed. The problem of analyzing the dynamics of a large mechanical system is, therefore, complicated.

There have been significant contributions recently on the study of dynamic response of mechanisms and mechanical systems involving computer-aided techniques.[1] Most of them take an approach which is general, involving the treatment of Lagrangian formulation of the system equations of motion and the use of numerical methods to yield solution. This is useful in many applications concerned particularly with large and complicated mechanical systems. System components may have various degrees of freedom and the generation of system equations in this case is not simple. Large-scale kinematic and dynamic analysis codes such as ADAMS, DADS, DRAM, DYMAC, IMP, KINSYN, LINCAGES, and others have significantly facilitated the implementation of modern analytical developments in mechanisms to the solution of realistic problems which may be otherwise difficult to obtain.

Of particular interest and concern in this investigation is the study of the dynamics of chain driven mechanical systems. There are several reasons motivating this study. Firstly, there is a real need for the dynamic analysis of systems of this kind. In recent times, primarily because of low cost, high efficiency, and capability to operate at high loads, chain drives have become one of the most popular and economic means of power transmission. Second and most importantly, methods and approaches are not available to treat chain-driven systems and there is not much work reported in the literature regarding chain drives. Moreover, modern kinematic and dynamic codes, to the author's knowledge, have not yet included chain as a basic element in the codes, and consequently, these codes are not directly applicable to chain-driven systems. The problem, therefore, warrants our investigation.

We begin with a dynamic analysis of the chain drive. A dynamic model of the chain is presented and it is basic to the determination of the dynamic response, such as dynamic load and motion characteristics of the chain. A typical large-scale mechanical system, an externally powered modern machine gun involving chain drive, is then investigated. It is used as an illustration of the proposed approach. The kinematic modeling and dynamic modeling using an effective code,

[1] The work of E. J. Haug and his co-workers; the work of M. A. Chace, N. Orlandea, J. J. Uicker, etc.; R. E. Beckett, K. C. Pan and S. C. Shu, ASME *Journal of Engineering for Industry*, Aug. 1977, pp. 666-673.

Contributed by the Design Automation Committee and presented at the Design and Production Engineering Technical Conference, Washington, D.C., September 12-15, 1982, of THE AMERICAN SOCIETY OF MECHANICAL ENGINEERS. Manuscript received at ASME Headquarters, June 9, 1982. Paper No. 82-DET-61.

DADS, are given. Finally, numerical results are presented and conclusions are drawn.

## 2 The Dynamics of Chain Drives

In the following, we give, first, a discussion on the chain polygonal action which affects the velocity fluctuation of chain based on a dynamic model. Secondly, we give the derivation of the position, velocity and acceleration equations of chain drive. A chain displacement function which represents essentially the motion characteristics of the chain is presented and is used in our study of the dynamics of the chain-driven system.

**2.1 Polygonal Action.** The action of a chain as it runs over a sprocket can be compared to a nonslipping thread running over a regular polygon prism. When the chain engages a sprocket, each link falls on a chord of the sprocket pitch polygon rather than the true pitch circle. Therefore, the active pitch diameter of the sprocket varies between the limits of a circle inscribed in the pitch polygon and a circle circumscribing the pitch polygon. The chain lying on the sprocket forms a polygon rather than a circle resulting in the "polygonal action" of the chain drive.

The speed of the chain, therefore, fluctuates even with the constant driving speed of the sprocket due to this "polygonal action." Impact occurs because of the difference in the velocities of the point on the roller and the point which comes into contact with the sprocket. This results in cyclic acceleration and deceleration which creates dynamic loads in the chain and often causes excessive noise and vibration. The effects of impact become complex and significant at higher speeds. Especially if the frequency of the velocity fluctuation coincides with a resonant frequency of the chain system, large stresses may occur which can cause fatigue failure.

Some aspects of polygonal action have been discussed in the literature [1-5]. Several interesting approximations have been made of the driven shaft angular velocity characteristics because of the polygonal effect of sprockets. A closer examination of the chain drive components shows that the motion of the system is actually transmitted through a series of four-bar linkages (Fig. 1). Using this concept, Morrison [3] analyzed the variation of the angular speed of the driven sprocket and found that by increasing the number of teeth in the sprockets the difference between pitch polygon and pitch circle will reduce and so does the polygonal effect. Bremer [5] recommended that the sprocket should at least have 30 teeth. In the particular case that the drive sprockets have a one-to-one ratio of their pitch circles and their center distance equals a whole number of link pitches, the chain will transmit uniform angular motion through the driven sprocket. Then, there is no speed fluctuation in the driven sprocket. The chain links, however, are still subject to pulsations. There is a polygonal effect on the connecting chain links, which is due to the speed fluctuation of each link along the linear direction of its chain path. In this case, the motion of the chain links and their masses become significant in the design consideration of the chain drives.

In chain drives, there are two ways of transmitting the power. In the common case, load is transmitted through the driven sprocket. In other cases, the load may be carried by a stud on the chain which makes the driven sprockets serve essentially as idlers. In the latter case, usually the impact effect between chain rollers and sprocket teeth can be neglected. The masses of chain links and the masses attached to the chain links, however, would still be subject to velocity fluctuation and, therefore, generate dynamic loads. The motions characteristics of the chain links and dynamic loads are analyzed and presented in the next section.

**2.2 Pulsation and Dynamic Loads.** As mentioned in the previous section, the chain drive can be treated by an equivalent mechanism of a four-bar linkage. The position, velocity, and acceleration of any point in the chain can, therefore, be expressed mathematically in terms of the four-bar parameters and the driving crank angle. A convenient method to derive these motion expressions is to use complex numbers to express the vector loop-closure equation of the equivalent linkage and to obtain its time derivatives. The following represents such an approach.

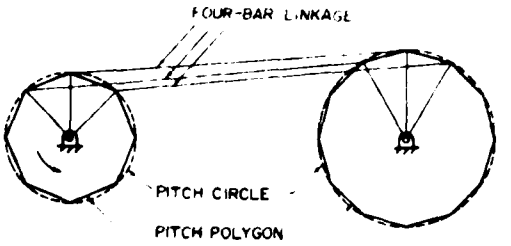

Fig. 1 Equivalent four-bar linkage of the chain drive

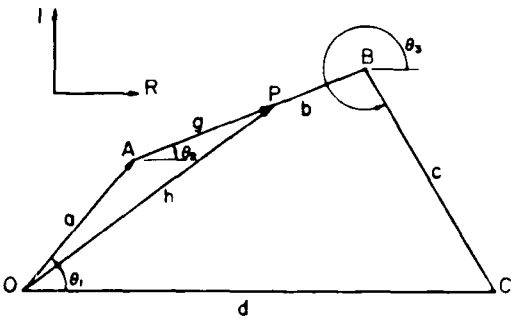

Fig. 2 Position vector for four-bar linkage

Take a point, P, for instance, in the chain link as shown in Fig. 2. We are interested in deriving its motion expressions, in particular, its linear velocity and acceleration in the direction of the chain path. The point, P, may be considered as a point on the coupler of the equivalent four-bar linkage. Referring to Fig. 2 and denoting $a$, $b$, $c$, and $d$ as the link length of the four bars, we have the position vector of P in complex number rotation.

$$\bar{h} = ae^{i\theta_1} + ge^{i\theta_2} \tag{1}$$

where the parameters $\theta_1$, $\theta_2$, and $\theta_3$ denote the angular positions of the links as shown in Fig. 2; the vectors $\bar{a} = \bar{OA}$ and $\bar{g} = \bar{AP}$.

Differentiating equation (1) with respect to time, we obtain the velocity of the point, P, as

$$\dot{\bar{h}} = ia\omega_1 e^{i\theta_1} + ig\omega_2 e^{i\theta_2} \tag{2}$$

The real and imaginary components are then,

$$\begin{aligned} R_v &= -a\omega_1 \sin\theta_1 - g\omega_2 \sin\theta_2 \\ I_v &= a\omega_1 \cos\theta_1 + g\omega_2 \cos\theta_2 \end{aligned} \tag{3}$$

Further differentiating equation (3) with respect to time, we obtain the acceleration of the point, P. Denoting the angular accelerations as $d\omega_1/dt = \alpha_1$ and $d\omega_2/dt = \alpha_2$, we have

$$\ddot{\bar{a}} = (-\omega_1^2 + i\alpha_1)ae^{i\theta_1} + (-\omega_2^2 + i\alpha_2)ge^{i\theta_2} \tag{4}$$

The real and imaginary parts are,

$$\begin{aligned} R_a &= -a(\omega_1^2 \cos\theta_1 + \alpha_1 \sin\theta_1) \\ &\quad -g(\omega_2^2 \cos\theta_2 + \alpha_2 \sin\theta_2) \\ I_a &= -a(\omega_1^2 \sin\theta_1 - \alpha_1 \cos\theta_1) \\ &\quad -g(\omega_2^2 \sin\theta_2 - \alpha_2 \cos\theta_2) \end{aligned} \tag{5}$$

Referring to Fig. 3, it is apparent that the real parts of equations (3) and (5) represent the linear velocity and acceleration of the point, P, parallel to the $X$-direction of the chain path, and the imaginary parts are the velocity and acceleration perpendicular to the $x$-direction.

In the case that the driving and the driven sprockets having a one-to-one ratio, the linear velocity ($V_l$) and acceleration ($a_l$) equations along the direction of the chain path of the contact point between the driving sprocket and the chain links become very simple. They are

$$V_l = -a\omega_1 \sin\theta_1$$

$$a_l = -a(\omega_1^2 \cos\theta_1 + \alpha_1 \sin\theta_1) \tag{6}$$

Furthermore, if the driving sprocket is running at constant speed, we have $\alpha_1 = 0$ and

$$V_l = -a\omega_1 \sin\theta_1$$

$$a_l = -a\omega_1^2 \cos\theta_1 \tag{7}$$

The chain pulsates with a period which is equal to

$$t = 60/Nn \text{ s} \tag{8}$$

where $N$ denotes the speed of the driving sprocket, and $n$ denotes the number of teeth on the sprocket. Thus, the frequency of this pulsation is

$$f = Nn/60 \text{ pulses per s} \tag{9}$$

If this frequency is close to the natural frequency of the chain system, the amplitudes in the $Y$-direction can reach a dangerous magnitude.

Now, consider that one chain link engages with the driving sprocket in the range of angle 90 deg $-\beta$ to 90 deg $+\beta$ (Fig. 3). By using equation (7), the accelerations at the instants that a particular link engages the sprocket while an adjacent one leaves the sprocket can be written as

$$a_{\text{engage}} = -a\omega^2 \sin\beta \tag{10}$$

and

$$a_{\text{leave}} = a\omega_1^2 \sin\beta \tag{11}$$

where, $\omega_1$ denotes the angular velocity of the sprocket and it is

$$\omega_1 = \frac{\pi N}{30} \text{ rad/s}$$

and

$$\beta = \sin^{-1}\left(\frac{L}{2a}\right) \tag{12}$$

The instantaneous increase in chain acceleration as a new sprocket tooth engages the chain is, therefore, equal to

$$\Delta a = |a_{\text{eng.}} - a_{\text{leave}}| = 2a\omega_1^2 \sin\beta \tag{13}$$

After substituting $\omega_1$ and $\beta$ into equation (13), we have

$$\Delta a = 2a\left(\frac{\pi N}{30}\right)^2 \sin\frac{\pi}{n}$$

$$= L\left(\frac{\pi N}{30}\right)^2 \tag{14}$$

It is this change of acceleration which results in an instantaneous dynamic load. We have

$$F_d = \sum_i \frac{W_i}{g}\left[2a\left(\frac{\pi N}{30}\right)^2 \sin\frac{\pi}{n}\right] \tag{15}$$

where $\Sigma_i W_i$ denotes the sum of the weight of all chain links plus the equivalent weight of all the following cascaded mechanical components.

Equations (1) and (15) which represent the general form of the chain displacement equation and the instantaneous dynamic load, respectively, are useful in the dynamic study of chain-driven systems. Depending upon the particular system in question, expressions similar to these can be derived and this will be demonstrated in a later section.

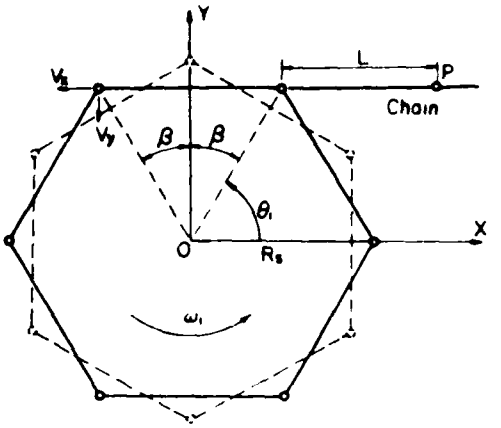


Fig. 3 A schematic of the chain polygon

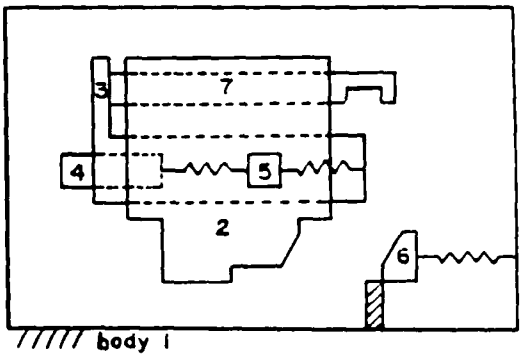


1: Gun body
2: Bolt-carrier
3: Striker
4: Striker plug and retainer
5: Buffer spring
6: Sear
7: Bolt

Logical spring-damper pairs

| Mass capture & release | Mechanical stop (impact) |
|---|---|
| Bodies 2 - 3 | Bodies 1 - 2 |
| 2 - 4 | 1 - 3 |
| 2 - 6 | 1 - 4 |
| 2 - 7 | 1 - 6 |
| | 1 - 7 |

Fig. 4 A schematic of the bolt-carrier assembly

## 3 Dynamic Modeling of an Automatic Weapon System—The Model X Gun

In this section, we would like to illustrate the use of chain displacement function in connection with an effective dynamic analysis code to study the dynamics of a complicated large-scale mechanical system with chain drive. It is the study of a new externally powered machine gun hereinafter referred to as the Model X gun.

Before a description of the kinematics of the gun, it is essential to give a brief introduction of the dynamic computer code, DADS, which is chosen in this investigation.

The DADS code (Dynamic Analysis and Design System) developed by Haug, Wehage, and their co-workers [6, 7] is a powerful computational package for the analysis and design

of mechanical systems. The code differs from other computer packages not only in its computational method, but also in its approach to treat mechanisms or mechanical systems with intermittent motion. The code utilizes logical spring and dampers [8, 9] to simulate the jump conditions which often occur for such systems. This makes the code particularly attractive to the dynamic study of mechanical systems with intermittent motion, such as the automatic weapon system. In the following sections, the DADS code is applied to study the dynamics of the Model X gun.

The kinematics of the Model X gun is determined essentially by the motion characteristics of the bolt-carrier assembly (i.e., bolt-carrier group) shown in Fig. 4, which is a mechanical system with intermittent motion.

The motion of the bolt-carrier contains a sequence of events involving finite masses capture and release as well as mechanical stops. The bolt-carrier, driven by the stud of a chain which moves along a definite near-square path (Fig. 5), moves in a reciprocating motion. Various gun operational stages are performed as the chain undergoes a cycle.

Let us consider now the modeling of the driving mechanism, in particular, the bolt-carrier and its associated components, in order to be able to adapt to the DADS code. We give first a terminology of components. The basic approach of modeling is presented next. Then, the kinematic motion cycle of the bolt-carrier assembly is outlined and graphically displayed.

**Terminology.** The bolt-carrier assembly consists of the following components (Fig. 4):

| Mass No. | Part Name and Function |
|---|---|
| 1 | gun body; taken as reference frame |
| 2 | bolt-carrier; the part that carries the bolt, striker, buffer spring and retainer and plug in the motion |
| 3 | striker; striking the fire pin to start propellant ignition |
| 4 | striker plug and retainer; retaining the buffer spring in compression |
| 5 | buffer spring; the lumped mass of buffer spring that functions as buffer and supplies the energy for striking |
| 6 | sear; the portion of the mechanism which controls the firing of the gun |
| 7 | bolt; the body that locks the cartridge into and extracts it from the chamber through camming action relative to the bolt-carrier |

In the dynamic model, the friction force between all translational joints are assumed to be zero. Mass 5 corresponds to the lumped mass of the buffer spring. It is assumed to be located, initially, at the center of bodies 3 and 4 and is precompressed to the length of 6.045 cm or 2.38 in.

**Basic Approach.** The driving mechanism of the Model X gun is a typical example of a large-scale, complex intermittent-motion mechanism. It is difficult to model. The application of DADS to analyze its dynamic response is not a simple task. In the following, the basic approach of modeling is given.

(1) The model includes only the bolt-carrier assembly. Other components of the power train are not taken into consideration.

(2) The kinematic motion of the bolt-carrier serves as input of the code, which is supplied as an externally user-supplied constraint function.

The displacement function of the bolt-carrier obtained from the kinematic analysis computer code of the Model X gun [10] is applied to DADS as a constraint. The code incorporates this constraint with the system equations of motion which are then solved simultaneously and iteratively at each time increment to match the value of state variables corresponding with the constrained displacements.

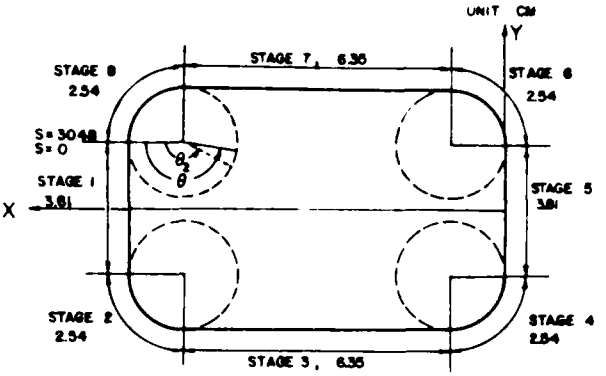

Fig. 5 Operational cycle of the Model X gun

(3) Logical springs and dampers are used to simulate the mass discontinuity and the impact phenomena. The selection of the magnitudes of these parameters and the proper locations to place them are often a heuristic approach (refers to Fig. 4). Details will be discussed later.

**The Motion Cycle.** The motion cycle of the bolt-carrier assembly involves two rectilinear motion periods (forward and rearward motions[1]) and two dwell periods. The dwell period, referring to Fig. 5, corresponds esentially to the indexing period of the Geneva mechanism (stage 1), and the firing and the gas escaping period (stage 5). In this study, only the forward and rearward motions are of concern. A detailed description of these motions is given in the following:

**(1) Forward Motion.** The forward motion involves the gun operational Stages 2, 3, and 4 of Fig. 5. In terms of the progressing of time, we have the following events:

(*a*) At $t = 0$, the bolt-carrier is ready to move rightward, and bodies 3, 4, and 7 are in the extreme left positions. The velocity and displacement of each body are at its initial value. The sear is stationary against the gun body (body 1) (Fig. 6).

(*b*) At $t = t_1 > 0$, the bolt-carrier starts to move rightward with the bolt (body 7) and the striker (body 3); however, the striker plug and retainer (body 4) remains stationary (Fig. 7).

(*c*) At $t_2$, the bolt-carrier captures the striker plug and retainer (body 4) and both move toward the right. At this moment, all the components, except sear, are moving at the same speed and direction (Fig. 8).

(*d*) At $t_3$, the striker (body 3) makes contact with the sear (body 6), and the buffer spring is under compression due to this effect. The rest of the masses (bodies 2, 7, and 4) continue to move rightward (Fig. 9).

(*e*) At $t_4$, the bolt (body 7) is locked on the gun barrel, and the bolt-carrier (body 2) is in contact with sear (body 6). The spring between the sear and the gun body (body 1) is in compression (Fig. 10).

(*f*) At $t_5$, the striker is ready for firing. All other components (bodies 2, 4, 6, and 7) are stopped and are going into the dwell stage (Fig. 11).

The time events described above are graphically displayed in Figs. 6 through 11. The logical spring-damper pairs (referring to Fig. 4) are used to simulate the finite masses capture and release, which are defined between body 2 and bodies 3, 4, 6, and 7. In addition, they are used to simulate the mechanical stop (i.e., impact), which are defined between body 1 and bodies 2, 3, 4, 6, and 7.

[1] Forward motion is designated as the motion cycle before firing.

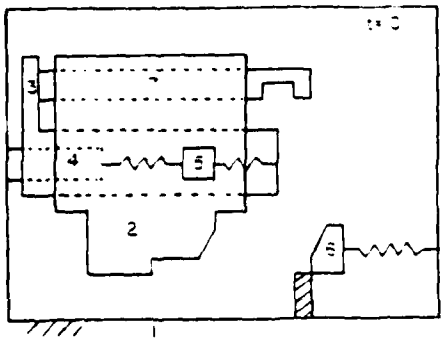


Fig. 6 Initial position of the bolt-carrier in forward motion

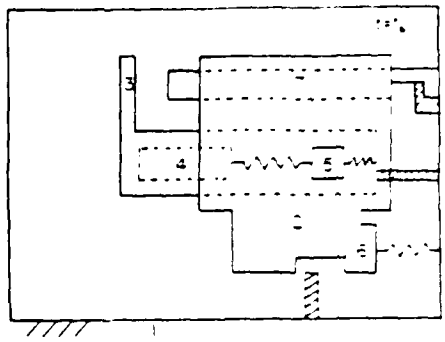


Fig. 10 The position that the bolt-carrier contacts the sear

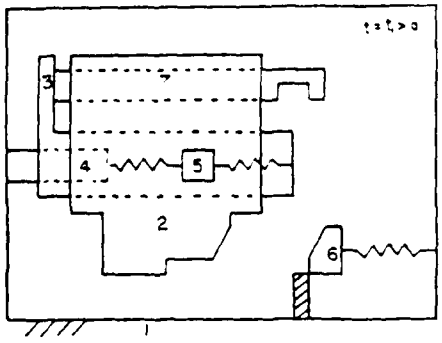


Fig. 7 Bolt-carrier assembly starts to move in the rightward position

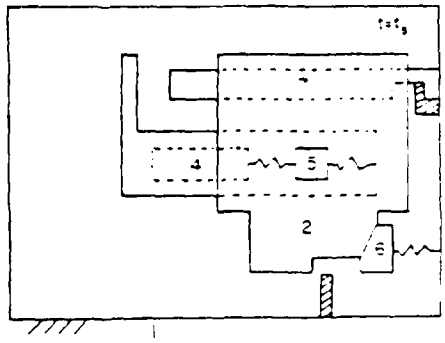


Fig. 11 The position of gun firing

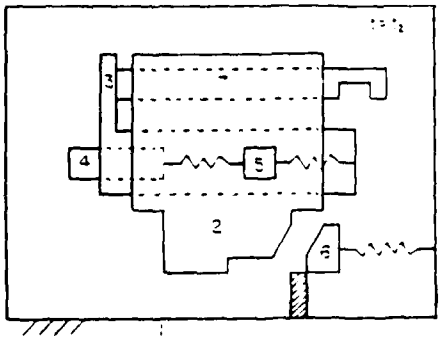


Fig. 8 The position that the bolt-carrier captures masses

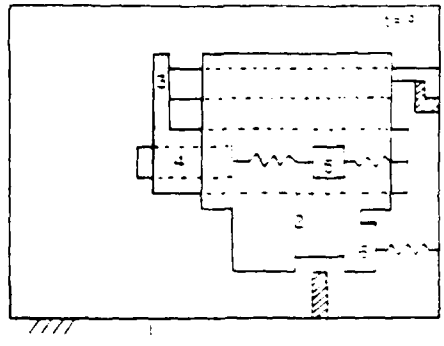


Fig. 12 Initial position of the bolt-carrier in rearward motion

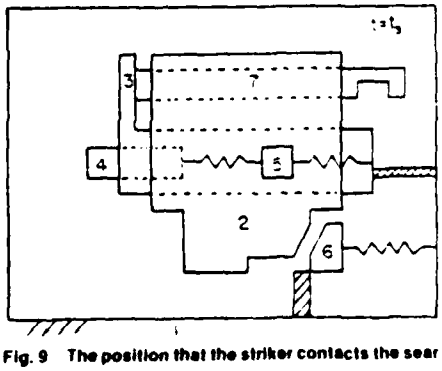


Fig. 9 The position that the striker contacts the sear

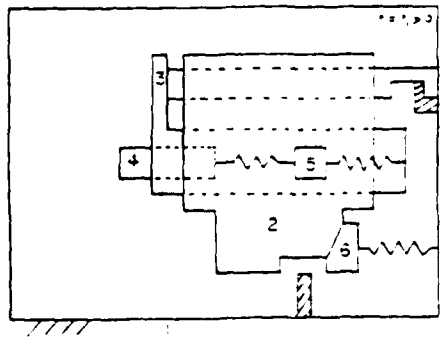


Fig. 13 Bolt-carrier assembly starts to move in the leftward position

**(2) Rearward Motion.** The rearward motion corresponds to the gun operational stages 6, 7, and 8 (Fig. 5). This part of the motion cycle is simulated with the consideration that the bolt (body 7) and the striker (body 3) are keyed together as a single body, denoted as body 3. This is because there is no relative motion between them during the period of motion. The time events are given as follows:

(*a*) At $t = 0$, the bolt-carrier (body 2) and its associated components are ready to make leftward motion while the buffer spring is compressed. The velocities and displacements of all members are at their initial conditions (Fig. 12).

(*b*) At $t = t_1 > 0$, the bolt-carrier starts to move leftward with the striker-plug and retainer (body 4). In the meantime, the bolt and striker (body 3) remain stationary. This is because the bolt is locked on the gun barrel and the striker sustains a spring force. The buffer spring is gradually released to its precompressed length. The sear moves at the same speed as the bolt-carrier (Fig. 13).

(*c*) At $t_2$, the bolt-carrier captures mass 3 (striker and bolt), and together they move toward the left. The sear is mechanically stopped by the gun body (body 1) (Fig. 8).

(*d*) At $t_3$, the striker-plug and retainer (body 4) contact the gun body (body 1) and they are stopped mechanically (i.e., impact). The buffer spring is then compressed. The bolt-carrier, the striker, and the bolt continue to move leftward. The sear remains motionless against the body 1 (Fig. 7).

(*e*) At $t_4$, the movement of the bolt-carrier is ceased and goes into the dwell stage. In the meantime, all other members are also in dwell (Fig. 6).

Logical spring-damper pairs are defined between body 2 and bodies 3, 4, and 6 to simulate the mass capture and release. In addition, they are defined between body 1 and bodies 2, 4, and 6 to simulate the mechanical stop.

The dynamic response during the dwell stages is not of concern in the modeling. This is because at the dwell stages of the motion cycle, the driving chain stud moved along the vertical direction of the chain path and there is no relative motion in the $X$-direction.

A summary of the time events and the corresponding graphical representation of the system are given in Table 1.

**Table 1 Time events representing the motion cycle of the gun mechanism**

| Figure | Motion: Forward Event No.* | Motion: Rearward Event No.* | Comments |
|---|---|---|---|
| 1 | a | e | Extreme left position |
| 5 | b | d | |
| 6 | c | c | Intermediate |
| 7 | d | | position |
| 8 | e | | |
| 10 | | b | |
| 11 | f | | Extreme right |
| 12 | | a | position |

*Refer to Section 3.

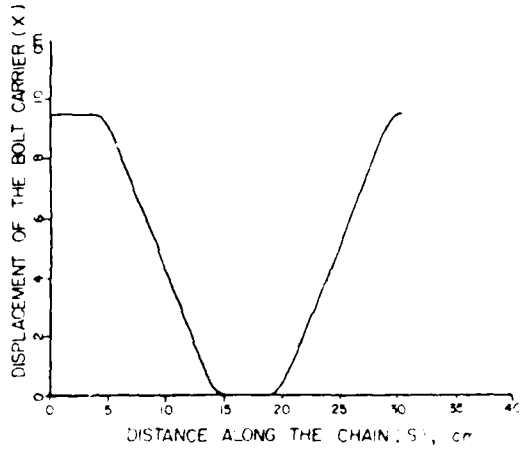


**Fig. 14 Displacement curve of the bolt-carrier in kinematic motion**

## 4 Chain Displacement Function

The expression of the chain displacement function depends upon the particular chain derived system in question. In the following, chain displacement functions are formulated for the Model X gun. The approach, however, is general and can be extended to any chain-driven system.

Denoting the motion parameter of the bolt-carrier along the longitudinal coordinate as $X$, and the displacement of the chain stud along the chain path as $S$ reference positions of both $X$ and $S$ are shown in Fig. 5. The chain path can be specified by eight positions or stations which divide the path into four straight and four curved portions. There are two ways to formulate the chain displacement function: 1) the kinematic displacement function; and 2) the dynamic displacement function.

**(1) The Kinematic Displacement Function.** In this approach the chain sprocket is physically replaced by the sprocket pitch circle. Polygonal effect, or the dynamic effect of the chain is, therefore, neglected. The displacement function formulated with this assumption is called the kinematic displacement function and it is described for each operational stage as follows:

1. Stage 1, $0 \le S \le 3.81$ cm
   $S = r_s(\theta - \theta_1), \theta_1 = 0$ deg
   $X = 6.35 + 2r_s$
2. Stage 2 (buffering), $3.81 \le S \le 6.35$ cm
   $S = 3.81 + r_s(\theta - \theta_2), \theta_2 = 135$ deg
   $X = r_s + 6.35 + r_s\cos(\theta - \theta_2)$
3. Stage 3, $6.35 \le S \le 12.7$ cm
   $S = 12.7 + r_s(\theta - \theta_3), \theta_3 = 225$ deg
   $X = r_s + 6.35 - r_s(\theta - \theta_3)$
4. Stage 4, $12.7 \le S \le 15.24$ cm
   $S = 12.7 + r_s(\theta - \theta_4), \theta_4 = 450$ deg
   $X = r_s - r_s\sin(\theta - \theta_4)$
5. Stage 5, $15.24 \le S \le 19.05$ cm
   $S = 15.24 + r_s(\theta - \theta_5), \theta_5 = 540$ deg
   $X = 0$
6. Stage 6, $19.05 \le S \le 21.59$ cm
   $S = 19.05 + r_s(\theta - \theta_6), \theta_6 = 675$ deg
   $X = r_s - r_s\cos(\theta - \theta_6)$
7. Stage 7, $21.59 \le S \le 27.94$ cm
   $S = 21.59 + r_s(\theta - \theta_7), \theta_7 = 765$ deg
   $X = r_s + r_s(\theta - \theta_7)$
8. Stage 8, $27.94 \le S \le 30.48$ cm
   $S = 27.94 + r_s(\theta - \theta_8), \theta_8 = 990$ deg
   $X = 8.0 + r_s\sin(\theta - \theta_8)$

By specifying the crank angle, $\theta$, the location of the chain stud and the displacement of the bolt-carrier along the $X$-axis can be calculated. The calculated displacement curve, shown in Fig. 14, matches very closely to the experimental result [10] which is shown in Fig. 15, using an Optron dynamic tracker.[1]

**(2) The Dynamic Displacement Function.** The dynamic displacement function implies that the dynamic of the chain,

[1] Electro-optical displacement tracks, model 501, Optron Corp., Wood-bridge, Conn.

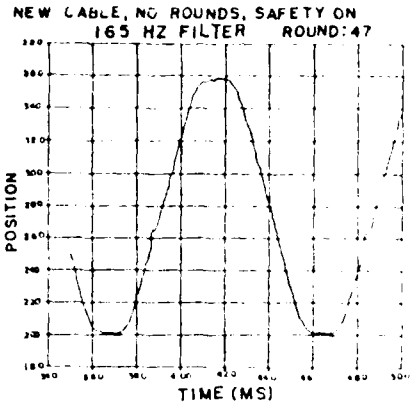


Fig. 15 The experimental displacement curve of the bolt-carrier

namely, the polygonal effect is incorporated in the displacement function using a model of four-bar linkage. Considering that the motion of chain stud in the forward and rearward direction can be divided into three operational stages as shown in Fig. 5, the displacement equations can be defined as follows:

**Forward Motion and Rearward Motion**[4]

*A. Stage 2, $0<\theta<90$ deg (Stage 6 for Rearward Motion).* In this stage, the chain stud moves along the pitch circle of the sprocket. We have

$$x = r_s(1 - \cos\theta) \tag{16}$$

where $r_s$ denotes the pitch circle of sprocket and $\theta$ denotes the crank angle.

*B. Stage 3, 90 deg $<\theta<$ 315 deg (Stage 7 for Rearward Motion).* The chain stud in this stage is in the span of chain links. As mentioned in Section 2, the chain drive can be modeled as an equivalent four bar linkage. The chain stud, therefore, can be considered as a point that moves along the coupler link and is subject to periodic motion. This can be seen by referring to Fig. 3. We have, therefore

(i) If $\theta_1 > 22.5$ deg

$$x = r_s + (N+1)L - r_s\sin(45 \text{ deg} - \theta_1) \tag{17}$$

(ii) If $\theta_1 < 22.5$ deg,

$$x = r_s + NL + r_s\sin\theta_1 \tag{18}$$

where $\theta_1 = \theta - 90$ deg $- 45$ deg $* N$, $N$ is the integer part of $(\theta - 90$ deg $/ 45$ deg) and $L$ is the link length. For every 22.5 degrees of $\theta_1$, the chain stud advances for a distance of one chain link.

*C. Stage 4, 315 deg $<\theta<$ 405 deg (Stage 8 for Rearward Motion).* In this stage, the path of the chain stud coincides with the pitch circle again, and is moving along the pitch circle. We have, therefore

$$x = r_s + 6.35 + r_s\sin(\theta - 315 \text{ deg}) \tag{19}$$

The displacement function of the chain is used as a kinematic constraint which serves as the input to the DADS code and it is coupled with the system equations of motion to represent the dynamic state of the chain-driven system.

## 5 The Dynamic Response of the Model X Gun

The output of the DADS code provides information concerning essentially two phases of study: the initial phase and the dynamic analysis phase.

[4] In the rearward motion, the displacement equations are identical as those of the forward motion, except the direction of motion.

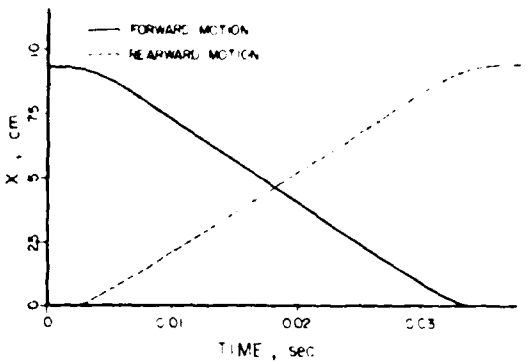


Fig. 16 The displacement curves of the bolt-carrier

**5.1 The Initial Phase.** The initial stage refers to the assembly phase of the system equations of motion in the DADS program. This involves the formulation of Jacobian matrix of partial derivatives for both the forward and rearward motions. The following information must be supplied: the position $(x,y,\phi)$ and velocity $(\dot{x},\dot{y},\dot{\phi})$ of bodies 2 through 7; the constraint forces which are generated to maintain these initial conditions for bodies at specified positions; information on the spring-damper pairs (such as velocity, spring length, force in $x$-direction and force in $y$-direction) and the spring and damping coefficients for the logical spring-damper pairs with respect to time; and the user-supplied constraint value.

**5.2 The Dynamic Analysis Phase.** The dynamic analysis phase is initiated when the static initial condition is removed. Physically, this means the chain stud begins to drive the bolt-carrier to move along the chain path. Certain conclusions can be made as follows:

(1) The displacement curves of the bolt carrier (body 2) are plotted in Fig. 16 for forward and rearward motion. These curves represent the constrained motion of the bolt-carrier along the $X$-direction. They match with the displacement curve reported in [10]. This is expected because the displacement function serves as the external constraint equation of the motion of the bolt-carrier.

(2) The velocity curves of the bolt-carrier are shown in Figs. 17 and 18. These curves represent the solution of system equations of motion at each time increment using different chain displacement functions.

(3) The velocity of other components can be readily obtained from the computer output. For instance, the forward motion of the striker is shown in Fig. 19. The curve represents the characteristics of intermittent-motion. The velocity of body 3 initially is the same as body 2 because of the mass capture effect. After a very short time interval, until $t = 0.025$ s, body 3 is stopped. This is done through the logical spring-damper pair to simulate the impact. The sudden change of velocity gives rise to a jump condition and demonstrates the behavior of intermittent-motion.

The effect of chain dynamics on the contact forces between components is significant. This can be seen by a comparison of the logical springer-damper forces between the bolt-carrier (body 2) and the striker plug (body 4), the sear (body 6) and the bolt (body 7) using different displacement functions. Numerical results and some typical comparisons are shown graphically in Figs. 20 and 21. For instance, the contact force between bodies 2 and 4 (refer to Fig. 5, during the chain operational stage 3 and a portion of stage 4) deviates considerably for both approaches. This is because the fluctuation of velocity is totally neglected in the analysis using the kinematic displacement function.

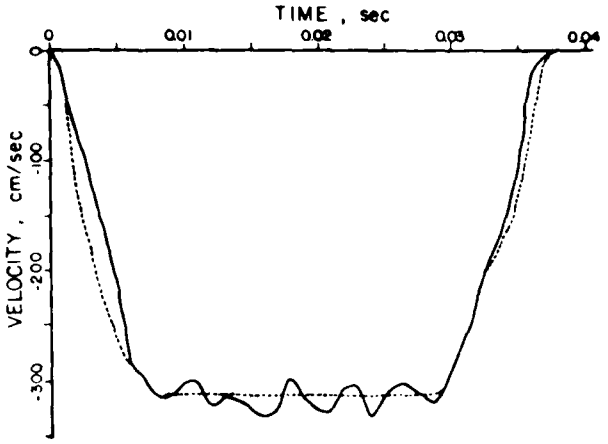


Fig. 17 The velocity of the bolt-carrier in forward motion

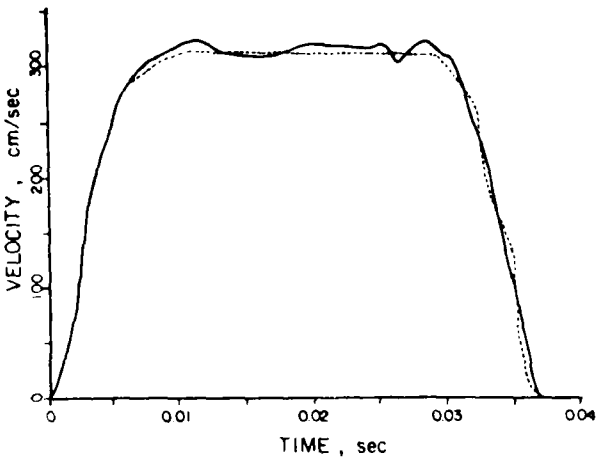


Fig. 18 The velocity of the bolt-carrier in rearward motion

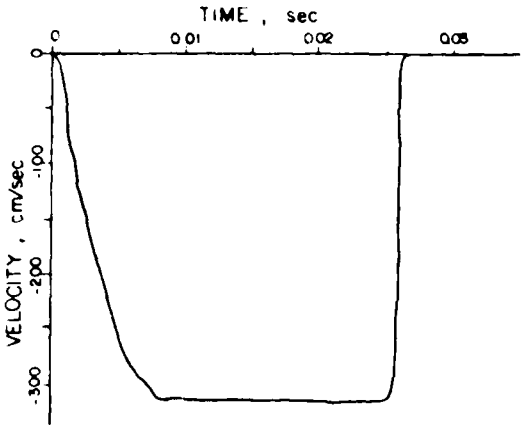


Fig. 19 The velocity of the striker in forward motion

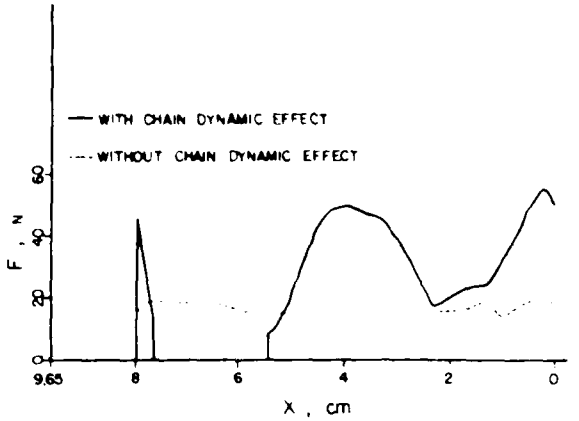


Fig. 20 Contact force between the bolt-carrier (body 2) and the striker plug-and-retainer (body 4) in forward motion

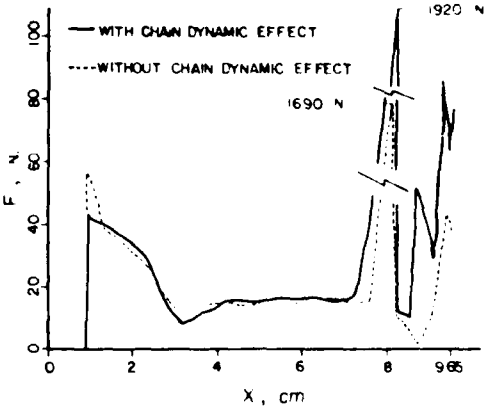


Fig. 21 Contact force between the bolt-carrier (body 2) and the striker (body 3) in rearward motion

(4) The present chain drive of the Model X gun is a good design. It apparently has already utilized some of the design criteria discussed and found in this investigation. The driving and driven sprockets are of the same size. In addition, the chain link length to pitch ratio is even. Therefore, a major part of the polygonal effect is essentially eliminated.

(5) The dynamic load of the chain is estimated in the next section. It can be reduced by increasing the number of teeth in the sprocket. Such design should minimize noise and vibration, and prolong the life of the chain. Moreover, the vibration transmitted through the bolt-carrier assembly can also be reduced.

**5.3 Dynamic Load.** One of the important pieces of information is the dynamic load generated by the chain links and this can be easily estimated based upon the theory developed before.

In the Model X gun, the chain has 24 links and it is 30.58 cm or 12 in. in length and has a mass of 214.32 gm (or weighs 0.4725 lb). The dynamic load at an operational speed of the gun, say 600 shots per minute, may be predicted with the help of equation (15). We have the following:

$$\text{Let } N = 1875 \text{ rpm}$$
$$L = 1.27 \text{ cm (0.5 in.)}$$
$$n = 8$$
$$\Sigma(W_i/g) = 720.4 \text{ gm}$$

Then, equation (15) gives a maximum dynamic load,

$$F_d = 352.74 \text{ N.}$$

The magnitude of this dynamic load is large. Therefore, its effect is significant. It is this load which generates part of the noise, vibration and stresses.

## 6 Conclusions

A general approach utilizing the DADS code to analyze the

dynamics of chain-driven systems has been presented. A model of the chain is formulated. It uses the equivalent four-bar linkage to derive a displacement function which represents the polygonal effect of chain. This function, in turn, serves as the kinematic constraint which is used as an input into the DADS to be coupled with the system equations. Using this approach, the dynamic analysis of a complicated chain-driven mechanical system is made possible. As an illustration, an automatic weapon system (i.e., the Model X gun) is modeled and analyzed.

The dynamic responses of the Model X gun are given. Forces between components as well as motion characteristics of this weapon system are fully explored, especially those for the impact forces between various components and the chain dynamic loads, which are difficult to estimate. Information such as this can be utilized to provide a durability study and design optimization of the gun.

The result of this investigation, it is believed, has extended our capability on the automated dynamic analysis to a large class of mechanical systems involving chain drives.

## 7 Acknowledgments

The author is grateful to the U.S. Army Research Office and the Army Armament Research and Development Command, Dover, NJ of the support of this research to Rutgers University; and to Mr. Chih-Hsing Ma for computational assistance.

## References

1 Radzimovsky, G. I., "Eliminating Pulsations in Chain Drives," *Product Engineering*, Vol. 26, No. 7, July 1955, pp. 153-157.

2 Mahalingram, S., "Polygonal Action in Chain Drive," *Journal of Franklin Institute*, Vol. 265, No. 1, 1958, pp. 23-28.

3 Morrison, R. A., "Polygonal Action in Roller Chain Drives," *Machine Design*, Vol. 24, No. 9, Sept. 1952, pp. 155-159.

4 Bouillon, G., and Tordion, G. V., "On Polygonal Action in Roller Chain Drives," ASME *Journal of Engineering for Industry*, May 1965, pp. 243-250.

5 Bremer, N. C., "Heavy Duty Chain Drives for Marine Propulsion Service," *Trans.* ASME, Vol. 69, 1947, p. 441-452.

6 Haug, E. J., Wehage, R. A., and Barman, N. C., "Dynamic Analysis and Design of Constrained Mechanical Systems," Technical Report No. 50, Material Division, College of Engineering, University of Iowa, Iowa City, Iowa, Nov. 1978.

7 Haug, E. J., Wehage, R. A., and Barman, N. C., "Design Sensitivity Analysis of Planar Mechanism and Machine Dynamics," ASME *Journal of Mechanical Design*, Vol. 103, No. 3, July 1981, pp. 560-570.

8 Haug, E. J., Barman, N. C., and Benzkofer, P. D., "Application of the Logical Function Method for Dynamic Analysis of Large Scale Systems with Intermittent Motion," Final Report, Project DAAK10-79-M-1781, Small Caliber System Laboratory, U.S. Army Armament, R and D Command, 1979.

9 Barman, N. C., "Design Sensitivity Analysis and Optimization of Constrained Dynamic Systems," Ph.D. thesis, University of Iowa, Iowa City, Iowa, 1979.

10 Lee, T. W., and Dahdouh, F., "A Computer Simulation of the Model X Gun Kinematics," Technical Report ARSCD-PR-81024, U.S. Army Armament Research and Development Command.

## APPENDIX B

## Articles Related to the Subject of

## Kinematic Characteristics of Mechanical Manipulators

1. On the Workspace of Mechanical Manipulators

2. On the Evaluation of Manipulator Workspace

3. Optimization of Manipulator Workspace

4. Feasibility Study of A Platform Type of Robotic Manipulators from A Kinematic Viewpoint

**D. C. H. Yang**
Graduate Student

**T. W. Lee**
Associate Professor
Mem. ASME

Department of Mechanical and
Aerospace Engineering,
Rutgers University,
New Brunswick, N.J. 08903

# On the Workspace of Mechanical Manipulators

*This paper presents an analytical investigation of manipulator workspace. The first part presents the derivation of a set of recursive equations in terms of motion and design parameters representing the workspace. These formulas are basic for the determination of the characteristics as well as the shape of workspace. The remainder of the paper concerns the investigation of the existence of hole and void in workspace. A set of criteria is formulated. Algorithms for implementing these criteria are developed. Manipulators with both unlimited and limited revolute joints are studied in this investigation.*

## 1 Introduction

One of the basic questions encountered in manipulator design is the determination of the shape of workspace. Given the structure of a manipulator, can one specify the shape of its workspace and study its characteristics analytically? The problem is a difficult one, primarily because of the large number of degrees of freedom involved in the manipulator system and the inherent complexity on spatial geometry. Therefore, very few investigations of the subject are on the record [1-6]. Roth [1] presented a pioneer study in 1975 on the relationship between the kinematic geometry and manipulator performance including workspace. Kumar and Waldron [2, 3] presented a thoughtful investigation on workspace and developed the theory and algorithm for tracing the bounding surfaces of manipulator workspace. Sugimoto and Duffy [4] proved the theories for determining the extreme distances of manipulator's hand. Tsai and Soni [5] studied the accessive region of manipulator with two and three revolute joints in planar motion. Recently, Gupta and Roth [6] in their illuminating paper, further extended the work of Roth and investigated certain design considerations on workspace, including the effect on hand size. Basic concepts and some investigations of primary (or dextrous) and secondary workspace have been presented [2, 3, 6].

This paper and a companion paper [7] represent an attempt to treat the foregoing question. The objectives of the present paper are: 1) to derive a set of recursive equations to represent the workspace analytically; 2) to formulate a set of criteria to investigate certain characteristics of this workspace, namely, the existence of hole and void; 3) to develop an effective algorithm for implementing these criteria; and 4) to extend the aforementioned studies to the practical case of limited revolute joint.

## 2 Manipulator Description

A manipulator with $n$ unlimited revolute joints in series can be represented schematically, as shown in Fig. 1. There are $n$ coordinate frames to specify the configuration. For any coordinate frame, say $k$, the $Z_k$-axis is always the joint axis and the $X_k$-axis is in the direction of common normal between axes $Z_k$ and $Z_{k+1}$. The $Z_1$-axis is attached to a fixed frame. The last link, link $n$, is associated with the hand or the end effector of the manipulator. Any link, say link $k$, is always considered to be connected to joint $k$. Three parameters are

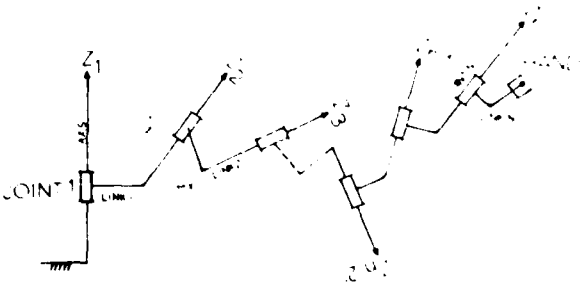


Fig. 1 A manipulator with $n$ revolute joints in series

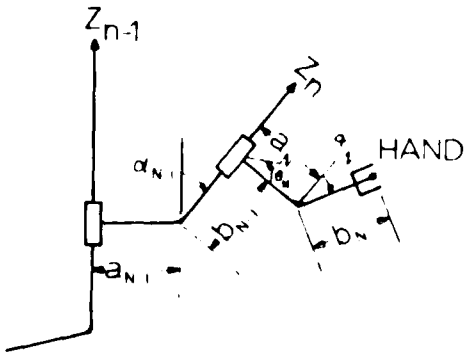


Fig. 2 Geometrical relationships between joints $n$ and $n-1$. ($a_{n-1}$ = common normal, $b_{n-1}$ = axial distance, $\alpha_{n-1}$ = twist angle and hand H)

Contributed by the Mechanisms Committee and presented at the Design and Production Engineering Technical Conference, Washington, D.C., September 12-15, 1982 of THE AMERICAN SOCIETY OF MECHANICAL ENGINEERS. Manuscript received at ASME Headquarters June 15, 1982. Paper No. 82-DET-127

needed to specify the geometrical relation of two consecutive joints: Referring to Fig. 2, they are $a_k$, the common normal between two consecutive axes $Z_k$ and $Z_{k+1}$; $\alpha_k$, the twist angle of these two axes; and $b_k$, the axial offset of joint $k+1$ on the axis $Z_{k+1}$. For convenience, the hand twist angle, $\alpha_n$, is sometimes considered to be zero. In this investigation, however, it is included as one of the design parameters. In the following, theory and criteria on manipulator workspace with unlimited revolute joint are first developed; they are then extended to the limited case which is of practical concern.

## 3 Analytical Representation of Workspace

The workspace of a manipulator is defined as the region which can be reached by the center of the manipulator's hand, $H$. Following the notion used in [6], let $W_k(H)$ denote the workspace generated by the point $H$ by turning all the revolute joints $k, k+1, \ldots, n$ with complete rotations while holding the axis $k$ as fixed. Referring to Fig. 2, if the revolute joint $n$ makes a complete rotation, the locus of the center of the hand $H(x_n, y_n, z_n)$ is a circle with respect to the coordinate frame $n$. The circle can be expressed in a parametric form by

$$\begin{aligned} x_n &= r_n \cos\vartheta_n \\ y_n &= r_n \sin\vartheta_n \\ z_n &= b_n \cos\alpha_n \end{aligned} \tag{1}$$

where

$$r_n = \sqrt{a_n^2 + (b_n \sin\alpha_n)^2} \tag{2}$$

and $\vartheta_n$ denotes the rotation angle of the joint $n$. In the case that the hand axis is parallel to the $Z$-axis of joint $n$, i.e. $\alpha_n = 0$, equation (1) then reduces to

$$\begin{aligned} x_n &= a_n \cos\vartheta_n \\ y_n &= a_n \sin\vartheta_n \\ z_n &= b_n \end{aligned} \tag{3}$$

The geometrical relationship between any two consecutive coordinate frames, say $n$ and $n-1$, can be represented by a homogeneous transformation $[A]_n$. By first turning the coordinate frame $n-1$ an angle $-\alpha_{n-1}$ with respect to the axis $X_{n-1}$, then followed by two pure translations along the axes $X_{n-1}$ and $Z_n$ with magnitudes $a_{n-1}$ and $b_{n-1}$, respectively, we have

$$[A]_n = \begin{bmatrix} 1 & 0 & 0 & a_{n-1} \\ 0 & \cos\alpha_{n-1} & \sin\alpha_{n-1} & 0 \\ 0 & -\sin\alpha_{n-1} & \cos\alpha_{n-1} & 0 \\ 0 & 0 & 0 & 1 \end{bmatrix} \begin{bmatrix} 1 & 0 & 0 & 0 \\ 0 & 1 & 0 & 0 \\ 0 & 0 & 1 & b_{n-1} \\ 0 & 0 & 0 & 1 \end{bmatrix}$$

$$= \begin{bmatrix} 1 & 0 & 0 & a_{n-1} \\ 0 & \cos\alpha_{n-1} & \sin\alpha_{n-1} & b_{n-1}\sin\alpha_{n-1} \\ 0 & -\sin\alpha_{n-1} & \cos\alpha_{n-1} & b_{n-1}\cos\alpha_{n-1} \\ 0 & 0 & 0 & 1 \end{bmatrix} \tag{4}$$

Let space $k$ be the space that all its points are specified by the coordinate frame $k$. Using equation (4), the circle represented by equation (1) in space $n$ can then be formulated in space $n-1$ as follows:

$$\begin{bmatrix} x \\ y \\ z \\ 1 \end{bmatrix}_{n-1} = [A]_n \begin{bmatrix} x \\ y \\ z \\ 1 \end{bmatrix}_n - [A]_n \begin{bmatrix} r_n\cos\vartheta_n \\ r_n\sin\vartheta_n \\ b_n\cos\alpha_n \\ 1 \end{bmatrix} \tag{5}$$

and

## Nomenclature

Circular projection: It is the cross-section made by the physical profile of a rotating body on a screen containing the rotating axis; it depends on the shape of the body and the geometrical configuration of the rotating link, such as the twist angle, etc.

Coordinate frame $k$: Cartesian coordinate with origin at joint $k$, the $Z$-axis aligning along the joint axis, and the $X$-axis being the common normal between the axes $k$ and $k+1$

Space $k$: the space in which all points are specified by the coordinate frame $k$

$[A]_k$ = a homogeneous transformation which represents the geometrical relationship between the coordinate frames $k$ and $k+1$

$a_k$ = the common normal between the axes $Z_k$ and $Z_{k+1}$ (Fig. 2)

$b_k$ = the axial offset distance of the joint $k+1$ on link $k$ (Fig. 2)

$PL, PR$ = the distances between the axis $Z_k$ and points on $W_{k+1}^L(H)$ and $W_{k+1}^R(H)$ (Fig. 7)

$W_k(H)$ = workspace with respect to (w.r.t.) the joint $k$; or the set of reachable points of manipulator's hand, $H$, w.r.t. the joint $k$ (Fig. 3)

$W_k^L(H), W_k^R(H)$ = the circular projections of $W_{k-1}(H)$ on the left- and right-hand side of the plane $X_k Z_k$. They represent also left- and right-hand side cross-sections on $W_k(H)$ cut by the plane $X_k Z_k$ (Fig. 5(a)).

$XL, XR$ = distances between the axis $Z_k$ and points on $W_k^L(H)$ and $W_k^R(H)$ (Fig. 6)

$X_k, Y_k, Z_k$ = the coordinate axes of the frame $k$. $Z_k$ is also the axis of joint $k$ (Fig. 1).

$(x_k, y_k, z_k)$ = the coordinate of a point in workspace $W_k(H)$ w.r.t. the coordinate frame $k$ (Fig. 3)

$(x_k, y_k, z_k)^*$ = the coordinate of a point in workspace $W_k(H)$ w.r.t. the coordinate frame $k$ (Fig. 3)

$\alpha_k$ = the twist angle between the axes $Z_k$ and $Z_{k+1}$ (Fig. 2)

$\beta_k$ = the location angle of the link $k+1$ w.r.t. the link $k$; the angle between the axes $X_k$ and $X_{k+1}$ in case of limited joint $k+1$ (Fig. 14)

$\vartheta_k$ = rotating angle of the joint $k$ (Fig. 12)

$\varphi_k$ = $\pi/2 - \alpha_k$; an angular quantity (Fig. 6)

$\Theta_k$ = rotational range of the joint $k$

$$
\begin{aligned}
x_{n-1}^{*} &= r_n \cos\vartheta_n + a_{n-1} \\
y_{n-1}^{*} &= r_n \sin\vartheta_n \cos\alpha_{n-1} \\
&\quad + b_n \cos\alpha_n \sin\alpha_{n-1} + b_{n-1} \sin\alpha_{n-1} \\
z_{n-1}^{*} &= -r_n \sin\vartheta_n \sin\alpha_{n-1} \\
&\quad + b_n \cos\alpha_n \cos\alpha_{n-1} + b_{n-1} \cos\alpha_{n-1}
\end{aligned} \tag{6}
$$

The workspace $W_{n-1}(H)$ can be obtained by turning the circle now represented by equation (6) with respect to the $Z_{n-1}$-axis. The shape of $W_{n-1}(H)$ is a torus, as shown in Fig. 3, and can be represented by

$$
\begin{aligned}
x_{n-1} &= r_{n-1} \cos\vartheta_{n-1} \\
y_{n-1} &= r_{n-1} \sin\vartheta_{n-1} \\
z_{n-1} &= z_{n-1}^{*}
\end{aligned} \tag{7}
$$

where

$$
r_{n-1} = \sqrt{x_{n-1}^{*2} + y_{n-1}^{*2}}
$$

Equations (1), (6), and (7) completely specify the evolution process of generating a workspace from the space $n$ to the space $n-1$.

A general recursive formula for workspace $W_k(H)$ can therefore be formulated as follows:

$$
\begin{aligned}
x_k &= r_k \cos\vartheta_k \\
y_k &= r_k \sin\vartheta_k \\
z_k &= z_k^{*}
\end{aligned} \tag{8}
$$

where

$$
r_k = \sqrt{x_k^{*2} + y_k^{*2}}
$$

and

$$
\begin{bmatrix} x \\ y \\ z \\ 1 \end{bmatrix}_k^{*} = [A]_{k+1} \begin{bmatrix} x \\ y \\ z \\ 1 \end{bmatrix}_{k+1} \tag{9}
$$

Equations (8) and (9) form the analytical representation of the manipulator workspace and are the basic formulas for the investigation of the existence of hole and void in workspace, and for the determination of the shape of workspace [7].

## 4 Cross-Section of Workspace Cut by $XZ$ Plane

Having the analytical representation of a workspace, it is now possible to investigate its characteristics. In this paper we are concerned with characteristics such as hole and void. In a companion paper [7], the investigations on the shape of the workspace including boundary and volume are reported. A basic approach to investigate these characteristics involves a close examination of cross-sections of a workspace. An important and convenient cross-section for this purpose is the cross-section of $W_k(H)$ cut by the plane $X_k Z_k$. This cross-section can be obtained by setting $y_k$ equal to zero, or equivalently, $\vartheta_k = 0$ or 180 deg, from equation (8). Mathematically, the cross-section may be expressed as

$$
\begin{aligned}
x_k &= \pm r_k \\
z_k &= z_k^{*}
\end{aligned} \tag{10}
$$

When $x_k = +r_k$, it means that the cross-section is on the right-hand side of the axis $Z_k$, and is denoted as $W_k^R(H)$. Similarly, the cross-section formed by $x_k = -r_k$ and $z_k = z_k^{*}$ is denoted as $W_k^L(H)$. It is worth noting that $W_k^R(H)$ and $W_k^L(H)$ are mirror images of each other and represent the

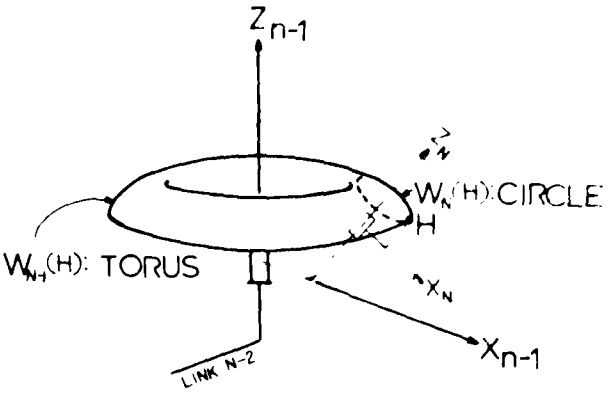


Fig. 3 The evolution of workspace

circular projections of the workspace $W_{k-1}(H)$ on the plane $X_k Z_k$. The term "circular projection" means the projection obtained on the plane $X_k Z_k$ as the workspace $W_{k-1}(H)$ rotates with the link $k$ and with respect to the axis $Z_k$.

In the following sections, criteria are established to examine cross-sections with regard to hole and void.

## 5 Hole in Workspace

A workspace that has a hole means there exists at least one straight line which is surrounded by the workspace yet without making contact to it. For a manipulator with revolute joints, its workspace $W_k(H)$ has a hole if and only if the preceding workspace $W_{k-1}(H)$ does not contact the axis $Z_k$. This implies that $W_k^R(H)$ does not contact the axis $Z_k$.

The mathematical criteria for the hole in workspace can be established based on the minimum distance between $W_k^R(H)$ and the axis $Z_k$, denoted by $XR_{min}$, as follows:

1. Without hole

$$
XR_{min} = 0 \tag{11.1}
$$

2. With hole

$$
XR_{min} > 0 \tag{11.2}
$$

Figures 4(*a*) and 4(*b*) illustrate these cases.

## 6 Void in Workspace

A void is defined as a region buried within a reachable workspace, which however, is not itself reachable by the manipulator's hand. From a practical point of view, it is always desirable to shun a void in the workspace, except in the case where a void contains a fixed part of the manipulator. The necessary condition for workspace, $W_k(H)$, containing a void is that the preceding workspace $W_{k-1}(H)$ has a hole. However, it is by no means a sufficient condition, as shown in Fig. 5. It is found in this study that the shape of $W_{k-1}(H)$ and the design of link $k$ also play important roles in determining the existence of void in workspace $W_k(H)$.

Depending upon the relative position of the axis $Z_k$ with respect to $W_{k-1}(H)$, three distinct and exclusive cases are considered. First, the workspace is apart from the axis $Z_k$; this means that the axis $Z_k$ neither contacts nor passes through the hole of the workspace $W_{k-1}(H)$. Second, the workspace $W_{k-1}(H)$ contacts the axis $Z_k$. Third, the axis $Z_k$ passes through the hole of workspace $W_{k-1}$. The criteria are different for these three situations and they are discussed separately as follows:

**6.1 Void in Workspace: When Axis $Z_k$ Is Apart from Workspace $W_{k-1}(H)$.** The condition of having void in

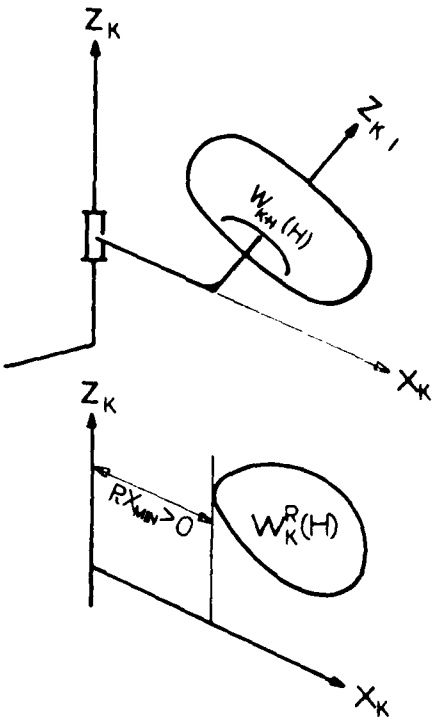


Fig. 4(a) A case of $W_k(H)$ with hole

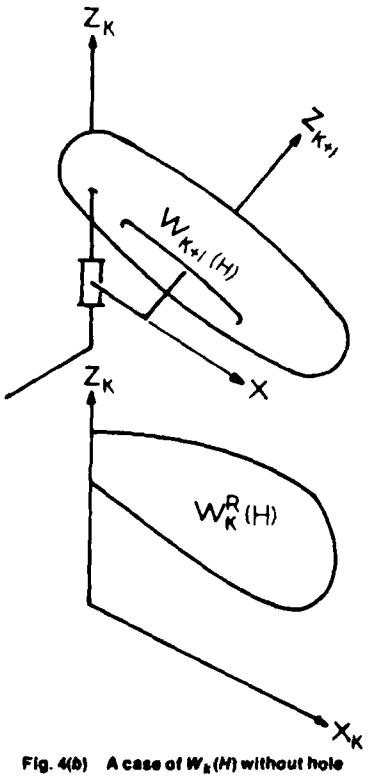


Fig. 4(b) A case of $W_k(H)$ without hole

$W_k(H)$ in this case, as shown in Fig. 8, can be analyzed from two aspects: firstly, for given shape of the workspace, $W_{k+1}(H)$, to determine the effect of the twist angle $\alpha_k$ and secondly, to see the effect of the depth of workspace $W_{k+1}(H)$ along its axis. Criteria for each case are established. If either

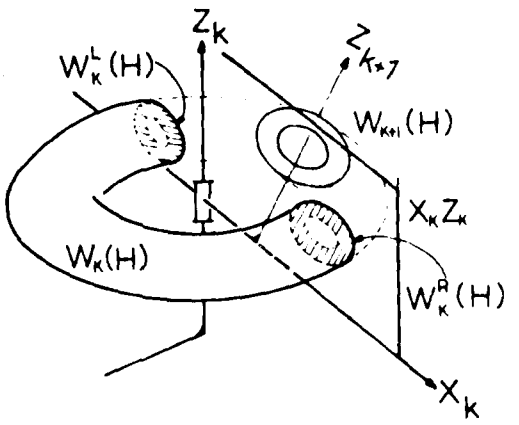


Fig. 5(a) The existence of void in workspace: $W_{k+1}(H)$ has hole and $W_k(H)$ has void

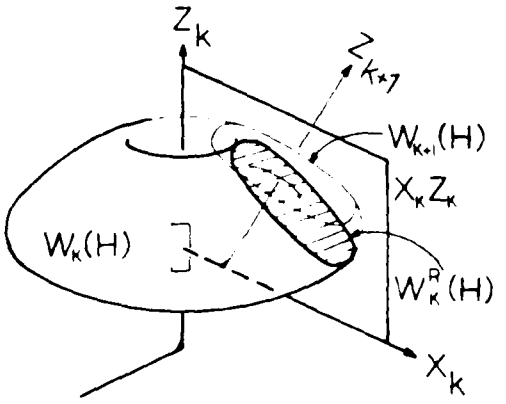


Fig. 5(b) The existence of void in workspace: $W_{k+1}(H)$ has hole and $W_k(H)$ has no void

one of these criteria is satisfied, a hole in workspace $W_{k+1}(H)$ will not cause a void in workspace $W_k(H)$.

*6.1.1 Criterion Based on Twist Angle.* One way to determine the existence of void in $W_k(H)$ is by an examination of the cross-section of $W_{k+1}(H)$. By viewing from a plane perpendicular to the axis of the joint $k$, one can examine the relative clearance between the circular projections, namely $W_{k+1}^R(H)$ and $W_{k+1}^L(H)$. This clearance depends upon the twist angle $\alpha_k$ and usually increases with increasing $\alpha_k$. If there exists no clearance, then there is no void in $W_k(H)$.

For the sake of illustration, let the cutting plane $X_{k+1}$ $Z_{k+1}$ for obtaining the circular projections $W_{k+1}^R(H)$ and $W_{k+1}^L(H)$ be perpendicular to the plane $X_k$ $Y_k$. Referring to Fig. 6, by rotating the axis $Z_{k+1}$ with an angle $\varphi_k = \pi/2 - \alpha_k$, the new position $Z'_{k+1}$ should then be parallel to the plane $X_k$ $Y_k$. The extreme distances between $Z'_{k+1}$ and $W_{k+1}^R(H)$ and $W_{k+1}^L(H)$ are shown as $XR_{min}$ and $XL_{max}$, respectively, as shown in Fig. 6. It is clearly seen that if the difference between these two quantities vanishes, there would be no void in $W_k(H)$. We, therefore, have the following criterion:

Criterion 1: *The workspace* $W_k(H)$ *has no void if the orthogonal projection of* $W_{k+1}^L(H)$ *and* $W_{k+1}^R(H)$, *with respect to a plane perpendicular to the* $Z'_{k+1}$ *axis, overlap. More specifically, the difference between the extreme distances,* $XR_{min}$ *and* $XL_{max}$ *is less than or equal to zero, i.e.,*

$$XR_{min} - XL_{max} \leq 0 \tag{12}$$

Mathematically it is not necessary that the cutting plane $X_{k+1}$ $Z_{k+1}$ be perpendicular to the plane $X_k$ $Y_k$. This is because the workspace $W_{k+1}(H)$ is always symmetric with respect to axis

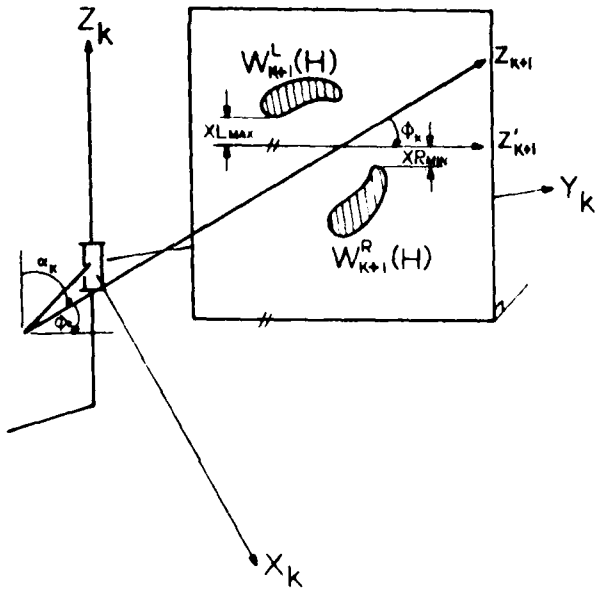


Fig. 6 Illustration of the effect of the twist angle on void

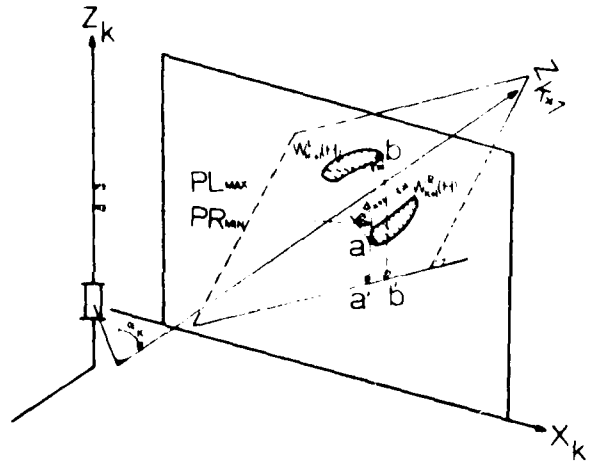


Fig. 7 Illustration of the effect of the workspace depth, $d_{k+1}$ on void

$Z_{k+1}$. The criterion is true whenever the cutting plane contains the axis $Z_{k+1}$.

Analytical expression for $XR_{min}$ and $XL_{max}$ can be derived as follows:

$$XR_{min} = \text{Min}[r_{k+1}\cos\varphi_k - z_{k+1}\sin\varphi_k]$$
$$XL_{max} = \text{Max}[-r_{k+1}\cos\varphi_k - z_{k+1}\sin\varphi_k] \quad (13)$$

where

$$\begin{bmatrix} x \\ z \end{bmatrix}_{k+1} = \begin{bmatrix} \cos\varphi_k & -\sin\varphi_k \\ \sin\varphi_k & \cos\varphi_k \end{bmatrix} \begin{bmatrix} x \\ z \end{bmatrix}_{k+1}$$
$$= \begin{bmatrix} \cos\varphi_k & -\sin\varphi_k \\ \sin\varphi_k & \cos\varphi_k \end{bmatrix} \begin{bmatrix} \pm r_{k+1} \\ z_{k+1} \end{bmatrix} \quad (14)$$

*6.2.2 Criterion Based on the Depth of Workspace* $W_{k+1}(H)$ *Along its Axis.* The depth of the workspace $W_{k+1}(H)$ along the $Z_{k+1}$-axis is defined as $d_{k+1}$, as shown in Fig. 7. This quantity represents, however, only one aspect of the characteristics of the shape of $W_{k+1}(H)$. It affects the relative distance of the $W^R_{k+1}(H)$ and $W^L_{k+1}(H)$ with respect to the joint $k$, i.e. $Z_k$-axis, which in turn affects the existence of void on $W_k(H)$. These relative distances are discussed as follows.

Referring to Fig. 7, let the axis $X_{k+1}$ be perpendicular to the plane $X_kZ_k$ and $PR(p)$ and $PL(q)$ be the distances of the axis $Z_k$ with respect to points $p$ and $q$ on $W^R_{k+1}(H)$ and $W^L_{k+1}(H)$, respectively. Denoting $PR_{min} = PR(a)$ and $PL_{max} = PL(b)$ as the minimum and maximum values of $PR(p)$ and $PL(q)$, respectively, we, therefore, have the following criterion:

Criterion 2: *The workspace* $W_k(H)$ *has no void if the circular projections of* $W^R_{k+1}$ *and* $W^L_{k+1}(H)$, *on any plane containing the rotating axis* $Z_k$, *overlap. More specifically, the difference between the extreme distances* $PR_{min}$ *and* $PL_{max}$ *is less than or equal to zero, i.e.,*

$$PR_{min} \le PL_{max} \quad (15)$$

*The distance* $PR(x, y)$ *and* $PL(x, y)$ *can be formulated as* follows:

$$PR(x, y) = \sqrt{x_k^2 + y_k^2} \ (\text{use } x_{k+1} = r_{k+1})$$
$$PL(x, y) = \sqrt{x_k^2 + y_k^2} \ (\text{use } x_{k+1} = -r_{k+1}) \quad (16)$$

where

$$\begin{bmatrix} x_k \\ y_k \\ z_k \\ 1 \end{bmatrix} = [A]_{k+1} \begin{bmatrix} \pm r_{k+1} \\ 0 \\ z_{k+1} \\ 1 \end{bmatrix} \quad (17)$$

**6.2 Void in Workspace: When Axis $Z_k$ Contacts to Workspace $W_{k+1}(H)$.** There are two types of contact between the axis $Z_k$ and workspace $W_{k+1}(H)$: single-portion contact (Fig. 9) and double-portion contact (Fig. 10). The terminology "double-portion contact" means that the contact between the axis $Z_k$ and the workspace $W_{k+1}(H)$ has a range of discontinuity.

In the case of single-portion contact, the criteria of no void in workspace $W_k(H)$ are the same as the previous case of no contact. Therefore when either equation (12) or equation (15) is true, there is no void in $W_k(H)$. In the case of double-portion contact, it is obvious that a void always exists in the workspace $W_k(H)$ regardless of whether the criteria of equations (12) and (15) are satisfied or not.

**6.3 Void in Workspace: When Axis $Z_k$ Passes Through The Hole of Workspace $W_{k+1}(H)$.** An example of this case is shown in Fig. 11. Apparently there is always a hole in workspace $W_k(H)$; however, there is no possibility of having a void.

## 7 An Algorithm for Detecting Void in Workspace

There are three distinctive geometrical relationships between the axis $Z_k$ and the workspace $W_{k+1}(H)$ as described previously. Consequently, corresponding to each category, the cross-section of $W_{k+1}(H)$ cut by the plane $X_kZ_k$ are different, as shown in Figs. 8, 9(*a*) 9(*b*), 10, and 11.

Given the structure of a manipulator, the question, therefore, is how to classify it according to these categories. A mapping technique is presented in this investigation for this purpose and an effective algorithm is developed to implement the technique.

**7.1 A Mapping Technique.** Realizing that the circular

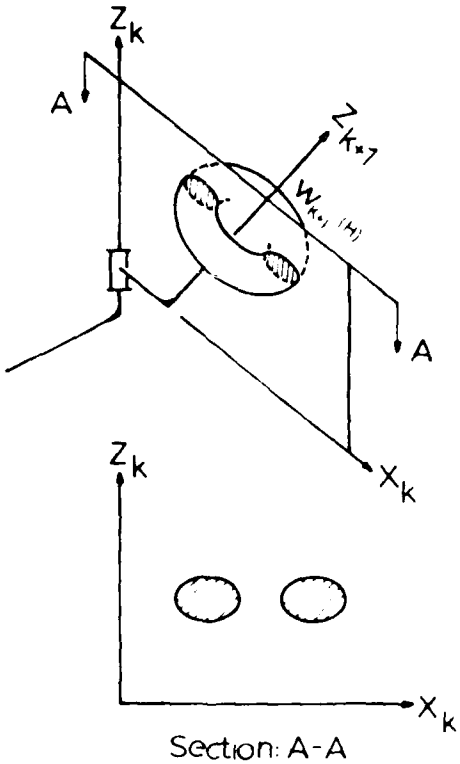


Fig. 8 Axis $Z_k$ is apart from workspace $W_{k+1}(H)$

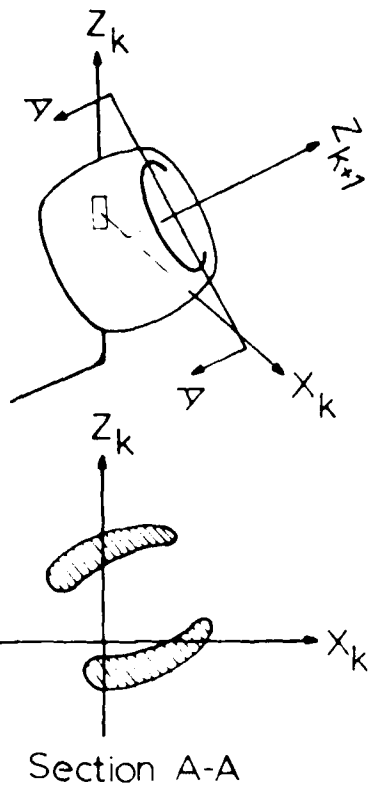


Fig. 10 Axis $Z_k$ contacts to $W_{k+1}(H)$: double-portion contact

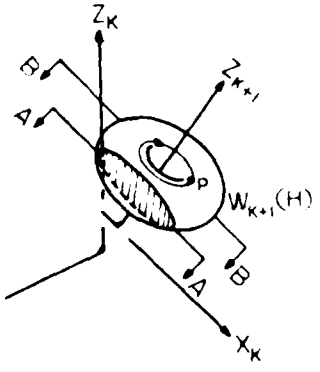


Fig. 9 Axis $Z_k$ contacts to $W_{k+1}(H)$: single-portion contact

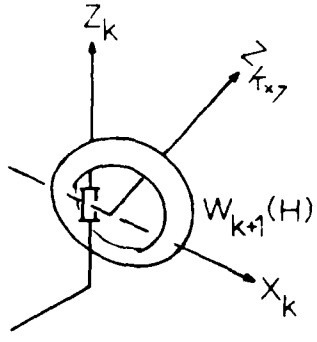


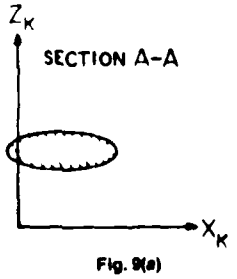


Fig. 9(a)
Section A-A; cut-through solid

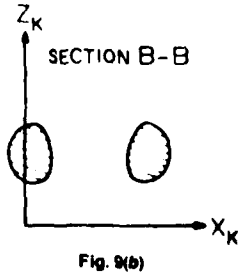


Fig. 9(b)
Section B-B; cut-through hole

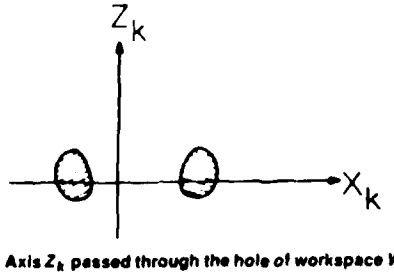


Fig. 11 Axis $Z_k$ passed through the hole of workspace $W_{k+1}(H)$

projection, either $W^R_{k+1}(H)$ or $W^L_{k+1}(H)$, can be readily obtained (equation (10)), the problem now is to find the appropriate procedure to map this cross-section from the $X_{k+1}\,Z_{k+1}$-plane to the plane $X_k Z_k$. Referring to Fig. 12, all points on $W^R_{k+1}(H)$ are mapped onto the plane $X_k Z_k$ through a rotation of link $k+1$ at various angles denoted by $\vartheta_{k+1}$.

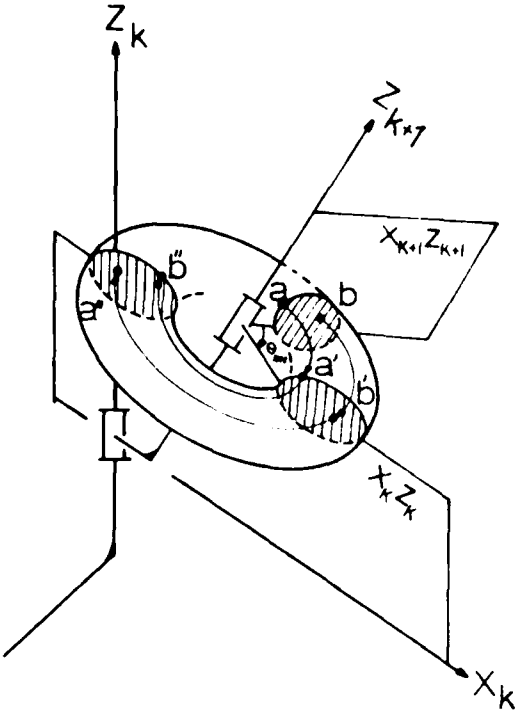


Fig. 12 Illustration of the concept of the Mapping Process

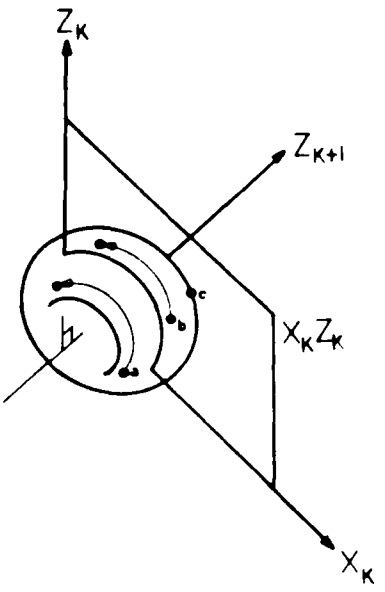


Fig. 13 A special condition that there is no mapping

This angle can be derived using a homogeneous transformation formula, equation (9), and then setting $y_k^*$ equal to zero, we have,

$$\vartheta_{k+1} = \sin^{-1}\left(-\frac{z_{k+1}\sin\alpha_k + b_k\sin\alpha_k}{r_{k+1}\cos\alpha_k}\right) \tag{18}$$

and

$$\begin{aligned} x_k^* &= r_{k+1}\cos\vartheta_{k+1} + a_k \\ y_k^* &= r_{k+1}\sin\vartheta_{k+1}\cos\alpha_k + z_{k+1}\sin\alpha_k + b_k\sin\alpha_k = 0 \\ z_k^* &= -r_{k+1}\sin\vartheta_{k+1}\sin\alpha_k + z_{k+1}\cos\alpha_k + b_k\cos\alpha_k \end{aligned} \tag{19}$$

Equation (18) shows that different points $(r_{k+1}, z_{k+1})$ on $W_{k+1}^R(H)$ have different mapping angles $\vartheta_{k+1}$. Knowing $\vartheta_{k+1}$, the corresponding point on $X_k Z_k$-plane in space $k$ can be calculated from equation (19).

**7.2 A Numerical Algorithm.** An algorithm is developed to analyze data obtained from the mapping function, equations (18) and (19). It is worth noting that equation (18) is not single valued; for each point of $(r_{k+1}, z_{k+1})$, there correspond two values of $\vartheta_{k+1}$, namely, $\vartheta_{k+1}$ and its complementary angle, $\pi - \vartheta_{k+1}$. Consequently, two values of $x_k$ are obtained from equation (19). This results in two groups of points: $[x_k(\vartheta_{k+1}), z_k]$ and $[x_k(\pi - \vartheta_{k+1}), z_k]$. From the sign of the extreme values of $x_k$ for each group denoted by $[\max(x_1), \min(x_1)]$ and $[\max(x_2), \min(x_2)]$, classifications of different categories based on general relationship of $Z_k$ and $W_{k+1}(H)$ can be established as follows:

1. Axis $Z_k$ is apart from $W_{k+1}(H)$:

$$\begin{aligned} &\text{Sign}[\max(x_1)] = \text{Sign}[\min(x_1)] \\ &\quad = \text{Sign}[\max(x_2)] = \text{Sign}[\min(x_2)] \end{aligned} \tag{20}$$

2A. Single-portion contact:

$$\text{Sign}[\max(x_1)] = \text{Sign}[\min(x_1)]$$

$$\text{Sign}[\max(x_2)] \neq \text{Sign}[\min(x_2)]$$

or

$$\begin{aligned} &\text{Sign}[\max(x_1)] \neq \text{Sign}[\min(x_1)] \\ &\text{Sign}[\max(x_2)] = \text{Sign}[\min(x_2)] \end{aligned} \tag{21}$$

2B. Double-portion contact:

$$\begin{aligned} &\text{Sign}[\max(x_1)] \neq \text{Sign}[\min(x_1)] \\ &\text{Sign}[\max(x_2)] \neq \text{Sign}[\min(x_2)] \end{aligned}$$

3. Axis $Z_k$ passes through the hole:

$$\begin{aligned} &\text{Sign}[\max(x_1)] = \text{Sign}[\min(x_1)] \\ &\quad \neq \text{Sign}[\max(x_2)] = \text{Sign}[\min(x_2)] \end{aligned} \tag{23}$$

**7.3 Special Conditions.** There are two special conditions of equation (18): 1) When the numerator is greater than the denominator, there will be no solution; and 2) when $\cos\alpha_k$ equals zero.

This first condition implies that mapping does not exist. Physically this means that the point in consideration does not come in contact with the plane $X_k Z_k$ when link $k+1$ makes a complete rotation, such as the point $p$ in Fig. 9.

The second condition refers to the case when the twist angle between the axes $Z_k$ and $Z_{k+1}$ is of a right angle. Consequently the mapping is meaningless. Referring to Fig. 13, the points $a$, $b$, and $c$ cannot be mapped onto the plane $X_k Z_k$. In this case equation (15) should be used as a criterion.

## 8 Manipulator With Limited Revolute Joints

The discussions and development so far were based upon unlimited revolute joints, in which case three parameters, namely, $a_k$, $b_k$, and $\alpha_k$, are sufficient to specify the geometrical relationship of two consecutive joints. However, in practice, most manipulators have limited joints. In this section, formulas and modifications are presented which take into account this effect. It is found that an additional angular parameter must be introduced. In the following, the justification of an additional parameter is presented, followed by a discussion on how to define this parameter; then a formula for the modified homogeneous transformation is

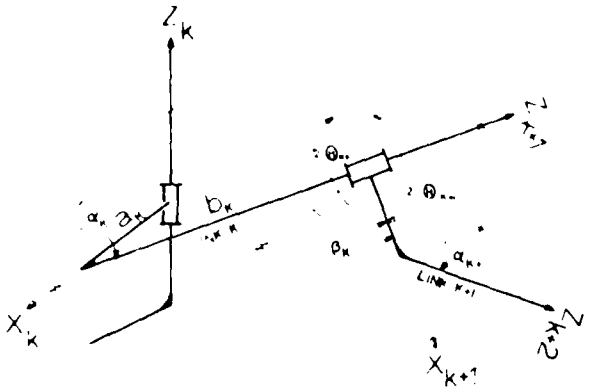

Fig. 14 Geometrical configuration for a limited joint

derived; and finally, the characteristics of hole and void are discussed.

For an unlimited joint, the Cartesian coordinate frame associated with this joint is defined by aligning the $Z$-axis along the joint axis, and by specifying the $X$-axis as the common normal between two consecutive axes. Since the joint can perform unlimited rotations, the location of $X$-axis on the plane $X_{k+1}$ $Y_{k+1}$ can be arbitrary. This is not true, however, for a limited joint. Since there is a portion of turning range, physically it cannot be reached by the link; the location defining this link therefore becomes important. Additional constraint on the selection of the $X_k$-axis must be introduced.

Considering a particular joint which is limited, say, the joint $k+1$, it is now relevant to define the Cartesian coordinate frame associated with this joint. Referring to Fig. 14, by specifying the link $k+1$ which is always in the mid-range of the joint rotation, and consequently the $X_{k+1}$-axis is also defined. A new parameter, $\beta_k$ is introduced and is defined as the angle between the $X_k$-axis and the $X_{k+1}$-axis in the same direction as the right-handed screw with respect to the axis $Z_{k+1}$. This parameter specifies the physical location of the link $k+1$ with reference to the link $k$ and, therefore, is called the location angle.

The homogeneous transformation between the coordinate frames $k+1$ and $k$ can now be represented by

$$[A]_{k+1} = \begin{vmatrix} 1 & 0 & 0 & a_k \\ 0 & \cos\alpha_k & \sin\alpha_k & b_k \sin\alpha_k \\ 0 & \sin\alpha_k & \cos\alpha_k & b_k \cos\alpha_k \\ 0 & 0 & 0 & 1 \end{vmatrix} \begin{vmatrix} \cos\beta_k & -\sin\beta_k & 0 & 0 \\ \sin\beta_k & \cos\beta_k & 0 & 0 \\ 0 & 0 & 1 & 0 \\ 0 & 0 & 0 & 1 \end{vmatrix}$$

$$= \begin{vmatrix} \cos\beta_k & -\sin\beta_k & 0 & a_k \\ \cos\alpha_k \sin\beta_k & \cos\alpha_k \cos\beta_k & \sin\alpha_k & b_k \sin\alpha_k \\ -\sin\alpha_k \sin\beta_k & -\sin\alpha_k \cos\beta_k & \cos\alpha_k & b_k \cos\alpha_k \\ 0 & 0 & 0 & 1 \end{vmatrix} \quad (24)$$

Characteristics of workspace regarding hole and void for a limited joint become relatively simple. For a manipulator with a limited joint, say joint $k+1$, there will be no hole in workspace $W_{k+1}(H)$; consequently, there will be no void in workspace $W_k(H)$.

## 9 Conclusion

This study provides some basic theories and formulations concerning the manipulator workspace. Analytical representation of workspace is presented. The difficult problem of the existence of hole and void in workspace can be treated with a set of procedures and criteria established in this investigation. Practical considerations are also included. Specific examples illustrating the basic theory presented here are reported in a companion paper [7], together with an investigation of the boundary and volume of workspace. The result of this research, it is hoped, will contribute toward the basic understanding and design of mechanical manipulators.

## 10 Acknowledgments

The authors are grateful to the Army Research Office for the support of this research through contract DAAG29-81-K-0016 to Rutgers University. Daniel Yang gratefully acknowledges the support of RCA Laboratories, Princeton, N.J., where he is employed.

## References

1 Roth, B., "Performance Evaluation of Manipulators from a Kinematic Viewpoint," NBS Special Publication No. 459, *Performance Evaluation of Programmable Robots and Manipulators*, 1975, pp. 39–61.

2 Kumar, A., and Waldron, K. J., "The Workspaces of a Mechanical Manipulator," ASME *Journal of Mechanical Design*, Vol. 103, No. 3, July 1981, pp. 665–672.

3 Kumar, A., and Waldron, K. J., "The Dextrous Workspace," ASME paper 80-DET-108, 1980.

4 Sugimoto, K., and Duffy, J., "Determination of Extreme Distances of a Robot Hand—Part 1: A General Theory," ASME *Journal of Mechanical Design*, Vol. 103, No. 3, July 1981, pp. 631–636.

5 Tsai, Y. C., and Soni, A. H., "Accessible Region and Synthesis of Robot Arms," ASME *Journal of Mechanical Design*, Vol. 103, No. 4, Oct. 1981, pp. 803–811.

6 Gupta, K. C., and Roth, B., "Design Considerations for Manipulator Workspace," ASME *Journal of Mechanical Design*, Vol. 104, No. 4, Oct. 1982, pp. 704–712.

7 Lee, J. W., and Yang, D. C. H., "On the Evaluation of Manipulator Workspace," this issue of ASME Journal of Mechanisms, Transmissions, and Automation in Design, pp. 70–77.

**T. W. Lee**
Associate Professor
Mem. ASME

**D. C. H. Yang**
Graduate Student

Department of Mechanical and Aerospace Engineering,
Rutgers University,
New Brunswick, N.J. 08903

# On the Evaluation of Manipulator Workspace

*This paper presents a theorem regarding manipulator workspace and, based on this theorem, a manipulator performance index is introduced. It is found that for a given manipulator structure the ratio of the volume of the workspace to the cube of its total link length is a constant. Algorithms for outlining the boundary profile of workspace and for quantitative evaluation of its volume are presented. A computer package, KAM, is developed, which implements the theories and algorithms developed in this investigation as well as in a companion paper [1]. Several specific examples are given to illustrate the application of the performance index and the capability of KAM.*

## 1 Introduction

There are a few basic problems on manipulator workspace remaining unsolved or only partially solved [1-4]. For instance, what criterion on workspace can one use on the evaluation of the kinematic performance of manipulators, or more fundamentally, how can the shape of a manipulator's workspace be determined?

This paper deals with these problems. In particular, the objectives are: firstly to develop an algorithm to outline the boundary of the workspace and to evaluate its volume quantitatively; and secondly, to present a manipulator performance index which is based on workspace and can be evaluated efficiently.

## 2 Manipulator With Revolute Joints

An analytical investigation of manipulator workspace is given by Yang and Lee [1]. The following, taken from [1], represent a description of manipulator geometry and a summary of the results on the analytical representation of workspace.

A manipulator with $n$ unlimited revolute joints in series can be represented schematically, as shown in Fig. 1. There are $n$ coordinate frames to specify the configuration. For any coordinate frame, say $k$, the $Z_k$ axis is always the joint axis and the $X_k$ axis is in the direction of the common normal between axes $Z_k$ and $Z_{k+1}$. The $Z_1$ axis is attached to a fixed frame. The last link, link $n$, is associated with the hand or the end effector of the manipulator. The link $k$ is connected to joint $k$. Three parameters are needed to specify the geometrical relation of two consecutive unlimited joints (joint being capable of making a complete rotation). Referring to Fig. 2(*a*), these parameters are $a_k$, the common normal between two consecutive axes $Z_k$ and $Z_{k+1}$; $\alpha_k$, the twist angle

Fig. 1 A revolute-joint manipulator

of these two axes [illegible] axis $Z_{k+1}$. For [illegible] rotational limit), an added [illegible] angle of link $k+1$ with respect [illegible] Fig. 2(*b*).

The workspace of a manipulator is defined as the [illegible] which can be reached by the center of the manipulator's hand. $H$, and $W_k(H)$ denotes the workspace generated by the point $H$, holding the axis $k$ as fixed while all the revolute joints $k$, $k+1, \ldots, n$ make rotations.

A general recursive formula for workspace $W_k(H)$ can therefore be formulated as follows

$$\begin{aligned} x_k &= r_k \cos\vartheta_k \\ y_k &= r_k \sin\vartheta_k \\ z_k &= z_k^* \end{aligned} \tag{1}$$

where $r_k = \sqrt{x_k^{*2} + y_k^{*2}}$ and

$$\begin{bmatrix} x \\ y \\ z \\ 1 \end{bmatrix}_k = [A]_{k-1} \begin{bmatrix} x \\ y \\ z \\ 1 \end{bmatrix}_{k+1} \tag{2}$$

where $\vartheta_k$ represents the rotation angle of joint $k$ and $[A]_{k-1}$

Contributed by the Mechanisms Committee and presented at the Design and Production Engineering Technical Conference, Washington, D.C., September 12-15, 1982, of THE AMERICAN SOCIETY OF MECHANICAL ENGINEERS. Manuscript received at ASME Headquarters, June 13, 1982. Paper No. 82-DET-126.

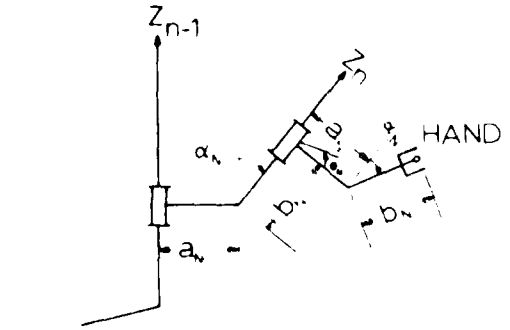


Fig. 2(a) Geometrical relationships between unlimited revolute joints

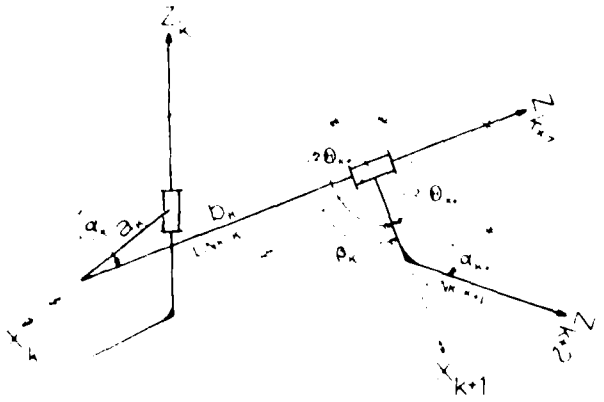

Fig. 2(b) Geometrical relationships between limited revolute joints

denotes the homogeneous transformation which provides the geometrical relationship between two consecutive coordinate frames $k+1$ and $k$. Depending upon whether the revolute joint is unlimited or limited, there are different expressions for $[A]_{k+1}$. For unlimited revolute joint, it is given as,

$$[A]_{k+1} = \begin{vmatrix} 1 & 0 & 0 & a_k \\ 0 & \cos\alpha_k & \sin\alpha_k & b_k \sin\alpha_k \\ 0 & -\sin\alpha_k & \cos\alpha_k & b_k \cos\alpha_k \\ 0 & 0 & 0 & 1 \end{vmatrix} \tag{3}$$

For limited revolute joint, we have

$$[A]_{k+1} = \begin{vmatrix} \cos\beta_k & \sin\beta_k & 0 & a_k \\ \cos\alpha_k \sin\beta_k & \cos\alpha_k \cos\beta_k & \sin\alpha_k & b_k \sin\alpha_k \\ \sin\alpha_k \sin\beta_k & -\sin\alpha_k \cos\beta_k & \cos\alpha_k & b_k \cos\alpha_k \\ 0 & 0 & 0 & 1 \end{vmatrix} \tag{4}$$

where $\beta_k$, referred to as the location angle, denotes the angle between the axes $X_k$ and $X_{k+1}$ while the joint $k+1$ is located at the center of its rotational range.

## 3 Boundary and Volume of Workspace

Having an analytical representation of a workspace, it is now possible to investigate the boundary and volume of manipulator workspace quantitatively. The basic approach involves the construction of a proper cross-section of the workspace, and from which numerical methods are developed to determine its boundary and subsequently the volume of the workspace.

Following [1], an important and convenient cross-section for this purpose is the cross-section on $W_k(H)$ cut by the plane $X_k Z_k$. It can be obtained by setting $y_k$ equal to zero or equivalently, $\vartheta_k = 0$ or 180 deg, from equation (1). Mathematically, this cross-section may be expressed as,

$$x_k = \pm r_k$$
$$z_k = z_k^* \tag{5}$$

When $x_k = +r_k$, it implies that the cross-section is on the right-hand side of the axis $Z_k$, and is denoted as $W_k^+(H)$. Similarly, the cross-section formed by $x_k = -r_k$ and $z_k = z_k^*$ is denoted as $W_k^-(H)$. It is worth noting that $W_k^+(H)$ and $W_k^-(H)$ are mirror images of each other and represent the circular projections of the workspace $W_{k-1}(H)$ on the plane $X_k Z_k$. The term "circular projection" [1] means the projection obtained on the plane $X_k Z_k$ as the workspace $W_{k-1}(H)$ rotates with the link $k$ and with respect to the axis $Z_k$.

Because the workspace $W_{k-1}(H)$ is symmetric with respect to the axis $Z_k$, $W_k^+(H)$ contains all the geometrical information regarding the shape of the workspace. The mathematical expression of $W_k^+(H)$, in equation (5), can be rewritten in parametric form as,

$$x_k = r_k = f(\vartheta_{k+1}, \vartheta_{k+2}, \ldots, \vartheta_n)$$
$$z_k = z_k^* = g(\vartheta_{k+1}, \vartheta_{k+2}, \ldots, \vartheta_n) \tag{6}$$

By scanning sequentially the joint angles $\vartheta_n$, $\vartheta_{n-1}$, ..., and $\vartheta_{k+1}$ according to their rotation limits, at a reasonably small interval, most of the points of $W_k^+(H)$ can thus be obtained.

**3.1 Boundary.** An algorithm for detecting the boundary of the workspace is developed. It is given as follows:

1. Dividing the plane $X_k Z_k$ into $I \times J$ small rectangles of width $\Delta x$ and height $\Delta z$, where $I$ and $J$ are the number of divisions along the $X$ axis and the $Z$ axis, respectively. Each rectangle is denoted as $P_{ij}(x_i, z_j)$ which is used to provide a binary imagine of $W_k^+(H)$, i.e.,

$P_{ij} = 1$, if $P_{ij}$ is a portion of $W_k^+(H)$

$P_{ij} = 0$, otherwise.

2. Initialization: set all $P_{ij}(x_i, z_j) = 0$.
3. Scanning process:
(*a*) Scanning all $\vartheta$'s beginning with $\vartheta_n$.
(*b*) For any $\vartheta_i$, say $\vartheta_i$, scanning up to $\Theta_i$ with step size $\Delta\vartheta_i$.
4. Construction of the binary image of $W_k^+(H)$.

$P_{ij}(x_i, z_j) = 1$, if any point $(x, z)$ in equation (6) falls into the following range $[x_i - \Delta x/2, x_i + \Delta x/2]$ and $[z_j - \Delta z/2, z_j + \Delta z/2]$ where, $\Delta x = x_{i+1} - x_i$ and $\Delta z = z_{j+1} - z_j$.

Record the extreme values of $z$ within each rectangle, $P_{ij}$. This gives $z_{max}(x_i)$ and $z_{min}(x_i)$.

Go to step 3 until the scanning process is complete. A data base for $W_k^+(H)$ is now stored.

5. Construction of the boundary of $W_k^+(H)$.

The extreme points of those rectangles which have $P_{ij}(x_i, z_j) = 1$ and are adjacent to the rectangles with $P_{ij}(x_i, z_j) = 0$, define the boundary of $W_k^+(H)$ (referring to Fig. 3). This construction is done by a scanning process which searches all $I \times J$ rectangles systematically.

This algorithm is capable of determining the boundary of workspace with irregular shape having convexity and void. If $W_k^+(H)$ is concave or it has void with respect to the $Z$ axis at certain values along the $X$ axis, say $x_i$, then there is a discontinuity of the value of $P_{ij}$, i.e., $P_{ij}$ changes from 1 to 0 and returns to 1. This characteristic can also be seen from Fig. 3.

**3.2 Volume.** Knowing the boundary of $W_k^+(H)$, the volume of workspace $W_{k-1}(H)$ can then be calculated by

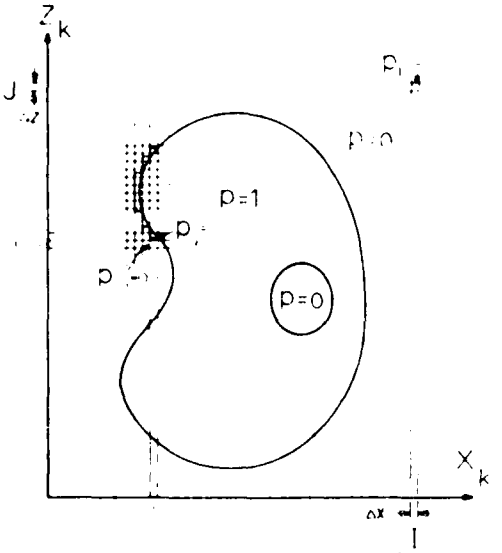


Fig. 3 Construction of the boundary of $W_k^R(H)$

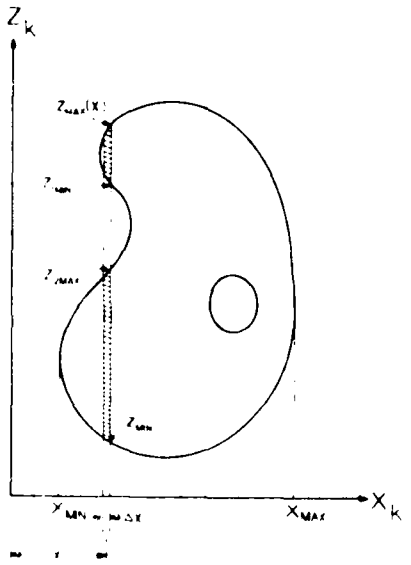

Fig. 4 An illustration of the integration of workspace volume

$$V_k = \sum_{x_{min}}^{x_{max}} \begin{cases} 2\pi x[(z_{max}(x) - z_{min}(x))\Delta x] \\ 2\pi x[(z_{2max}(x) - z_{1min}(x) + z_{2max}(x) - z_{min}(x))\Delta x] \end{cases} \quad (7)$$

referring to Fig. 4, where $X_{max}$ and $X_{min}$ denote the maximum and minimum of the $x$ value of $W_k^R(H)$; $z_{max}(x)$ and $z_{min}(x)$ are extreme values of $z$ at $x$; $z_{1min}(x)$ and $z_{2max}(x)$ are local extremes of $z$ value at the discontinuity while $W_k^R(H)$ is concave or has void at $x$; and $\Delta x$ represents the width of the dividing rectangle. For a certain value of $x$, if $W_k^R(H)$ has no discontinuity, the upper equation of equation (7) is used; if there exists discontinuity, the lower one should be used. If the joint $k$ is a limited revolute joint, then the angle $2\pi$ in equation (7) should be replaced by the physical turning range $\Theta_k$ of the joint. However, in this situation, error may occur in equation (7) from the undetermined end shape of the workspace. Fortunately, for most commercially available robots the first two or three links, which usually determine the volume of the workspace, are coplanar. Therefore the error

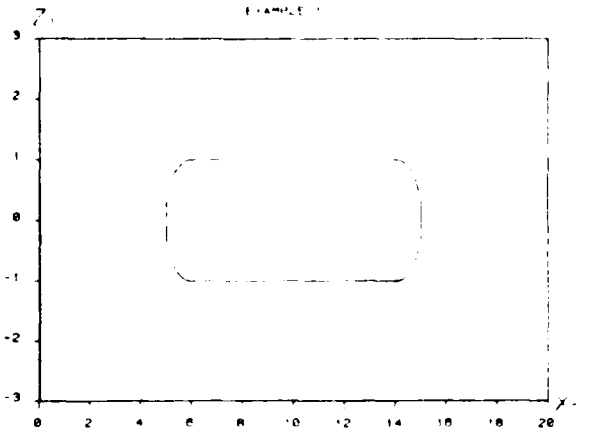

Fig. 5 Example 1 – boundary outlined by KAM

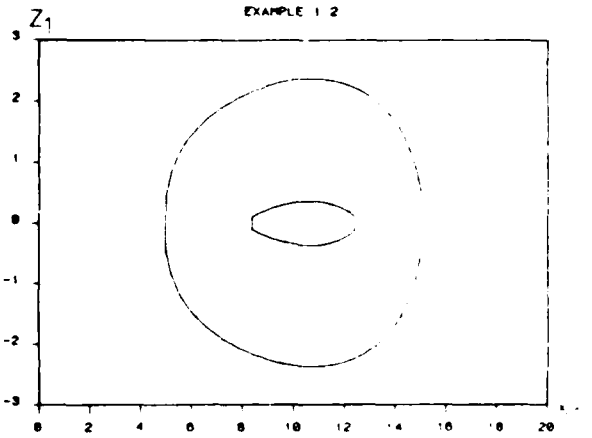


Fig. 6 Example 1 – workspace with void

due to the undetermined end shape will merely be caused by the last few short links, and shall not be very significant in practice.

## 4 Computer Program and Examples for the Boundary and Volume of Workspace

A computer program called KAM (Kinematic Analysis of Manipulators) and written in FORTRAN is developed. The code implements the theories and criteria presented in this paper as well as in the companion paper [1]. For a given manipulator structure, the program first defines analytically the workspace, then explores the existence of hole and void, outlines the boundary, and finally, calculates the total volume of the workspace. The inputs of the program are the geometrical parameters specifying the manipulator structure. These are, the number of revolute joints, the common normals, twist angles, and the axial offset distances. For a limited joint, two additional parameters, the location angle $\beta$, and the physical turning range $\Theta$, of the joint are needed. At present, KAM can handle manipulators up to six revolute joints; however, the extension of a higher number of joints does not present a problem. It can be easily done if it is needed.

Three problems which are believed to be representative are chosen to demonstrate the effectiveness as well as the capability of KAM.

*Example 1.* This example gives some indications of how well the prediction of KAM compares with the theoretical result on a special case. The problem, taken from Gupta and

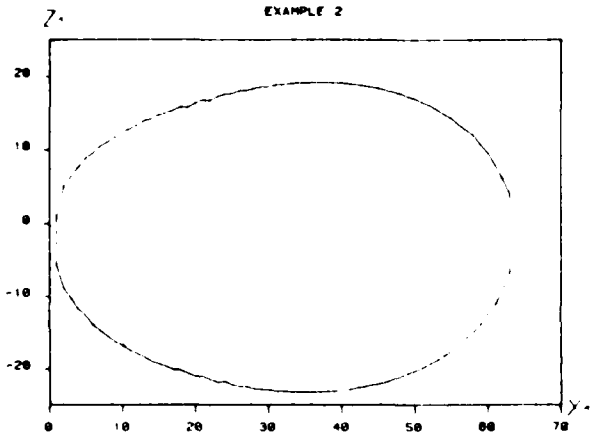


Fig. 7 Example 2 – boundary outlined by KAM

Roth [5], refers to a very simple manipulator. It has three unlimited revolute joints with special proportions: $a_1 = 10$, $a_2 = 4$, $a_3 = 1$; $b_1 = 0$, $b_2 = 0$, $b_3 = 0$; $\alpha_1 = 0$ deg, $\alpha_2 = 90$ deg, $\alpha_3 = 0$ deg. Because of the simplicity of the structure, analytical formulas for calculating the volume and the condition of existence of void in terms of the angle $\alpha_1$ can be derived and have been given [5]. A comparative study is given as follows:

| | volume [in.$^3$] | angle $\alpha_1$ |
|---|---|---|
| analytical [5] | 1202.7 | $\alpha_1 > 14.4475$ deg |
| KAM | 1215.7 | $\alpha_1 > 14.478$ deg |

The comparison looks very good. The predicted value of volume is within 1 percent of the analytical value, and the difference on the angle $\alpha_1$ which is the angle that the workspace starts to have void, is less than 0.004 percent. Figure 5 shows the boundary of the workspace of this example.

Figure 6 shows a workspace which has a void in it. All design parameters are the same for this case, except for the twist angle $\alpha_1$ which equals 20 degrees. The volume of this workspace equals 2309.9 in$^3$.

*Example 2.* In this example, a comparative study is given with the method of Kumar and Waldron [6]. A manipulator has six unlimited revolute joints with the following geometrical configuration: $a_1 = 32$, $a_2 = 16$, $a_3 = 8$, $a_4 = 4$, $a_5 = 2$, $a_6 = 1$; $b_1 = 0$, $b_2 = 5$, $b_3 = 0$, $b_4 = 0$, $b_5 = 1$, $b_6 = 0$; $\alpha_1 = 26.7$ deg, $\alpha_2 = 123.5$ deg, $\alpha_3 = -24.5$ deg, $\alpha_4 = 86.0$ deg, $\alpha_5 = -143$ deg, $\alpha_6 = 0$ deg. The boundary of workspace outlined by KAM is shown in Fig. 7, and matches with the result of [6]. Furthermore, KAM provides additional information such as no void in workspace and a quantitative value of the volume of workspace which equals 436753 in$^3$.

*Example 3.* In this example, a commercially available robot PUMA 600 is used as an illustration. Of particular interest is that this is a practical example, like any industrial robot, usually having limited revolute joints. Design parameters of this manipulator are: $a_1 = 0$, $a_2 = 18$, $a_3 = 0$, $a_4 = 0$, $a_5 = 0$, $a_6 = 0$; $b_1 = 10$, $b_2 = 4$, $b_3 = 17$, $b_4 = 0$, $b_5 = 2$, $b_6 = 0$; $\alpha_1 = 90$ deg, $\alpha_2 = 180$ deg, $\alpha_3 = 90$ deg, $\alpha_4 = 90$ deg, $\alpha_5 = 90$ deg, $\alpha_6 = 0$ deg; $\beta_1 = -90$ deg, $\beta_2 = -90$ deg, $\beta_3 = 30$ deg, $\beta_4 = 180$ deg, $\beta_5 = 0$ deg; $\Theta_1 = 320$ deg, $\Theta_2 = 250$ deg, $\Theta_3 = 270$ deg, $\Theta_4 = 280$ deg, $\Theta_5 = 200$ deg, $\Theta_6 = 532$ deg. Since the hand of a manipulator is interchangeable, depending on applications, it is best to exclude it from our evaluation of the workspace. The manipulator is, therefore, equivalent to a five joint manipulator. Using KAM, the workspace of PUMA 600 is found to be 183885.6 in.$^3$, and its boundary is shown in Fig. 8(*a*).

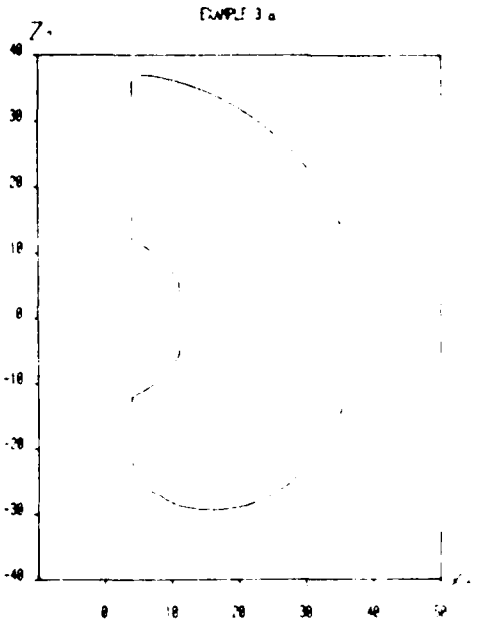


Fig. 8(*a*) PUMA 600 – real case

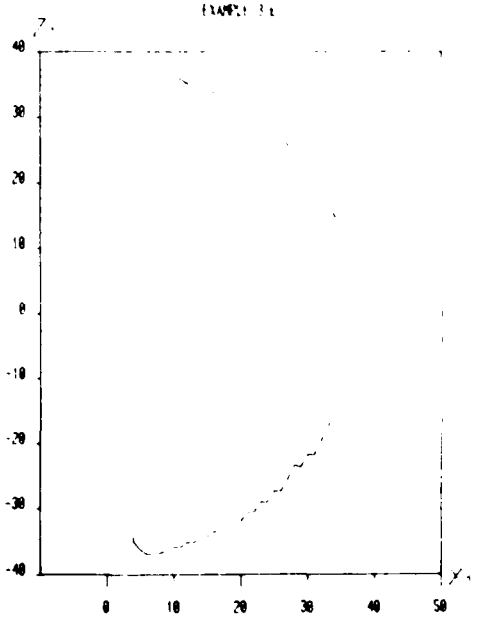


Fig. 8(*b*) PUMA 600 – ideal case

To make a comparison with an ideal case, that is, if all the joints on the PUMA 600 were unlimited, the volume of the workspace then equals to 216410 in.$^3$, and its boundary is shown in Fig. 8(*b*). It is worth noting that in this example the workspace of the real manipulator is about 17.6 percent less than the ideal case.

## 5 A Performance Index Based on Workspace Volume

Given a manipulator we are now capable of evaluating its workspace volume quantitatively. The question remaining in this investigation is the development of a performance index based on workspace volume. In this section, such index is presented. A theoretical proof is given which shows this index

is a constant and remains to be the same for similar manipulator structures.

The length of links of manipulator with $n$ revolute joints are $a_1, a_2, \ldots, a_n$ and $b_1, b_2, \ldots, b_n$ which correspond to their common normals and axial offsets. For convenience in our discussion, they are renamed as $l_1, l_2, \ldots, l_n, l_{n+1}, \ldots, l_{2n}$. Based on the concept of dimensional analysis, the volume of this manipulator's workspace can be represented by a general formula,

$$V = \sum_{i,j,k}^{2n} \mu_{ijk} l_i l_j l_k \tag{8}$$

where $i$, $j$, and $k$ can be any integer from 1 to $2n$, and $\mu_{ijk}$ is the corresponding coefficient of the term $l_i l_j l_k$. The coefficients $\mu_{ijk}$ can be any real value depending on the structure of a manipulator.

It is found in this investigation that there is a definite relationship between the volume of workspace and the total length of a manipulator. This is given in the following theorem:

**Theorem.** For a given manipulator, (i.e., the twist angles, rotation limits, location angles, and the proportions of link length are given), the ratio between the volume of the workspace and the cube of the total length is a constant, i.e.,

$$\frac{V}{(l_1 + l_2 + \ldots + l_{2n})^3} = \frac{V}{L^3} = \text{constant} \tag{9}$$

Proof:

Since the proportions of link length are fixed, the length of any link can be represented by the length of another link with the given proportion. Now let every link be in terms of the axial offset distance of the last link, $l_{2n}$, we have,

$$\begin{aligned} l_1 &= p_1 \quad l_{2n} \\ l_2 &= p_2 \quad l_{2n} \\ &\cdots \\ l_{2n-1} &= p_{2n-1} \quad l_{2n} \end{aligned} \tag{10}$$

where $p_i$'s are known proportions.

Combining equations (8) and (10),

$$V = \sum_{i,j,k}^{2n} \mu_{ijk} l_i l_j l_k = \sum_{i,j,k}^{2n} \mu_{ijk} l_{2n}^3 (p_i p_j p_k) = [P] l_{2n}^3 \tag{11}$$

where $[P] = \sum_{i,j,k}^{2n} \mu_{ijk} p_i p_j p_k = \text{constant}$.

Let $L$ represent the total link length, then,

$$\begin{aligned} L &= l_1 + l_2 + \ldots + l_{2n} \\ &= l_{2n}(p_1 + p_2 + \ldots + p_{2n-1} + 1) \\ &= [Q] l_{2n} \end{aligned} \tag{12}$$

where $[Q] = (p_1 + p_2 + \ldots + p_{2n-1} + 1) = \text{constant}$.

From equations (11) and (12), we have

$$\frac{V}{L^3} = \frac{[P] l_{2n}^3}{[Q]^3 l_{2n}^3} = \frac{[P]}{[Q]^3} = VI \tag{13}$$

Since [P] and [Q] are constants, VI is also a constant. This proves the theorem.

The notation VI stands for the Volume Index of manipulator workspace, which gives an indication of the effectiveness of link length on the creation of reachable workspace. The index can be normalized by dividing its possible maximum value. Letting the total length of a manipulator equal $L$, the maximum workspace that this manipulator can possibly have is a sphere with radius $L$ and centered at the joint 1. Therefore, the maximum VI a manipulator can possibly have is,

$$\frac{4\pi L^3/3}{L^3} = \frac{4\pi}{3} = 4.1888 \tag{14}$$

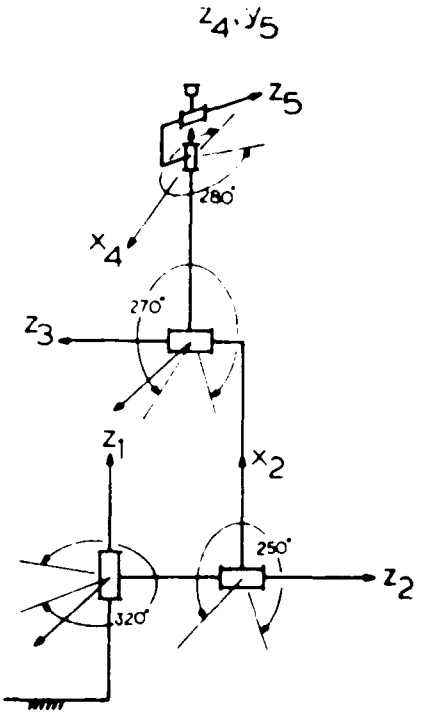


Fig. 9(a1)

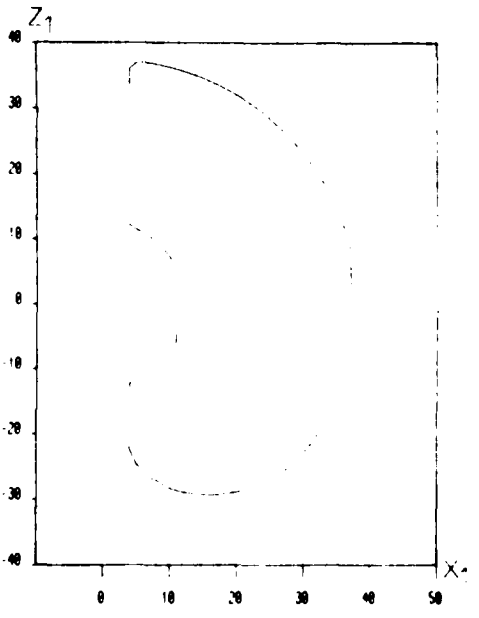


Fig. 9(a2)

**Fig. 9(a) Structure and boundary of PUMA 600**

Using this value as a normalizing factor, a normalized volume index, denoted as NVI, can be obtained, and its value is between 0 and 1.

This index is a kinematic performance index which can be used in practice for quantitative evaluation of manipulators based on workspace. Using the algorithm developed in this investigation, this performance index can be evaluated efficiently.

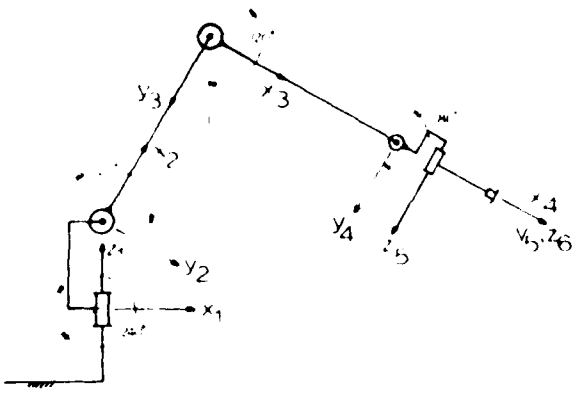


Fig. 9(b1)

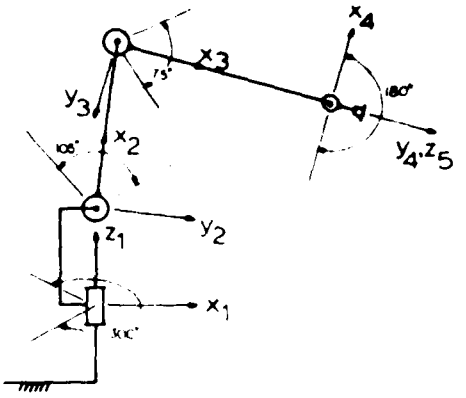


Fig. 9(c1)

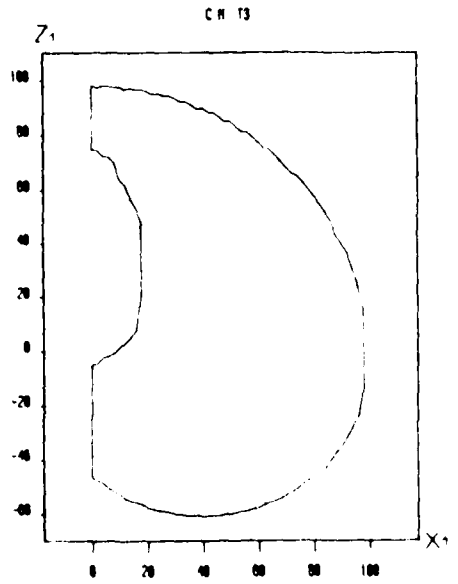


Fig. 9(b2)

Fig. 9(b) Structure and boundary of Cincinnati Milacron $T^3$

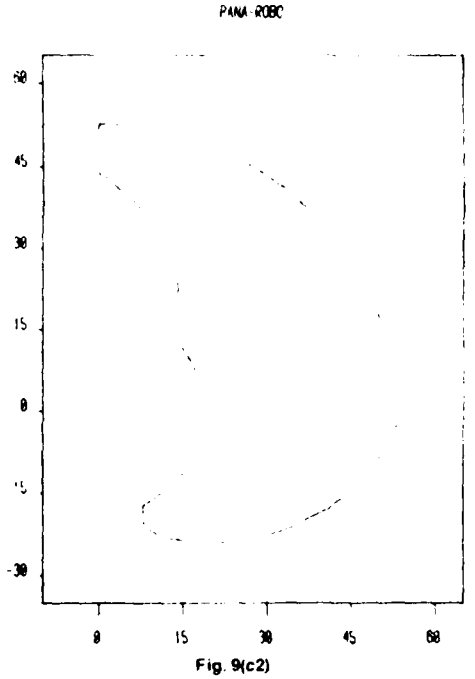


Fig. 9(c2)

Fig. 9(c) Structure and boundary of Pana-Robo

## 6 Case Studies: The Evaluation of Manipulators Based on Volume Index

Five commercially available manipulators, as shown in Fig. 9, are evaluated in terms of VI and NVI. These manipulators are:

**Case 1: PUMA 600 [7].** The design parameters of this manipulator are given in example 3 of Section 4. The structure of this manipulator and the boundary of the workspace from KAM are given in Fig. 9(*a*).

**Case 2: Cincinnati Milacron $T^3$ [8].** The design parameters of this manipulator are: $a_1 = 0$, $a_2 = 40$, $a_3 = 40$, $a_4 = 8$, $a_5 = 0$, $a_6 = 0$; $b_1 = 0$, $b_2 = 0$, $b_3 = 0$, $b_4 = 0$, $b_5 = 13$, $b_6 = 0$; $\alpha_1 = 90$ deg, $\alpha_2 = 0$ deg, $\alpha_3 = 0$ deg, $\alpha_4 = 90$ deg, $\alpha_5 = 90$ deg, $\alpha_6 = 0$ deg; $\beta_1 = -60$ deg, $\beta_2 = 90$ deg, $\beta_3 = 0$ deg, $\beta_4 = -90$ deg; $\Theta_1 = 240$ deg, $\Theta_2 = 120$ deg, $\Theta_3 = 120$ deg, $\Theta_4 = 120$ deg, $\Theta_5 = 180$ deg, $\Theta_6 = 270$ deg, $\Theta_6 = 360$ deg. The structure of this manipulator and the boundary of the workspace are given in Fig. 9(*b*).

**Case 3: Pana-Robo [9].** The design parameters of this manipulator are: $a_1 = 0$, $a_2 = 23.622$, $a_3 = 31.496$, $a_4 = 0$, $a_5 = 0$; $b_1 = 0$, $b_2 = 0$, $b_3 = 0$, $b_4 = 4.724$, $b_5 = 0$; $\alpha_1 = 90$ deg, $\alpha_2 = 0$ deg, $\alpha_3 = 0$ deg, $\alpha_4 = 90$ deg, $\alpha_5 = 0$ deg; $\beta_1 = -82.5$ deg, $\beta_2 = 97.5$ deg, $\beta_3 = -90$ deg; $\Theta_1 = 300$ deg, $\Theta_2 = 105$ deg, $\Theta_3 = 75$ deg, $\Theta_4 = 180$ deg, $\Theta_5 = 360$ deg. The structure of this manipulator and the boundary of the workspace from KAM are given in Fig. 9(*c*).

**Case 4: AID 800 [10].** The design parameters of this manipulator are: $a_1 = 0$, $a_2 = 23.622$, $a_3 = 31.496$, $a_4 = 0$, $a_5 = 0$; $b_1 = 0$, $b_2 = 0$, $b_3 = 0$, $b_4 = 3.9$, $b_5 = 0$; $\alpha_1 = 90$ deg, $\alpha_2 = 0$ deg, $\alpha_3 = 0$ deg, $\alpha_4 = 90$ deg, $\alpha_5 = 0$ deg; $\beta_1 = -92.5$ deg, $\beta_2 = 100$ deg, $\beta_3 = -90$ deg; $\Theta_1 = 300$ deg, $\Theta_2 = -95$ deg, $\Theta_3 = 70$ deg, $\Theta_4 = 180$ deg, $\Theta_5 = 360$ deg. The structure of this manipulator and the boundary of the workspace from KAM are given in Fig. 9(*d*).

**Case 5: Cybotech V30 [11].** The design parameters of this manipulator are: $a_1 = 0$, $a_2 = 31.496$, $a_3 = 39.37$, $a_4 = 0$, $a_5 = 0$,

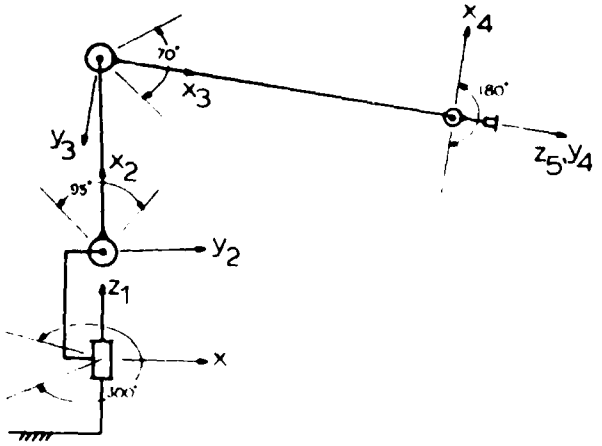


Fig. 9(d1)

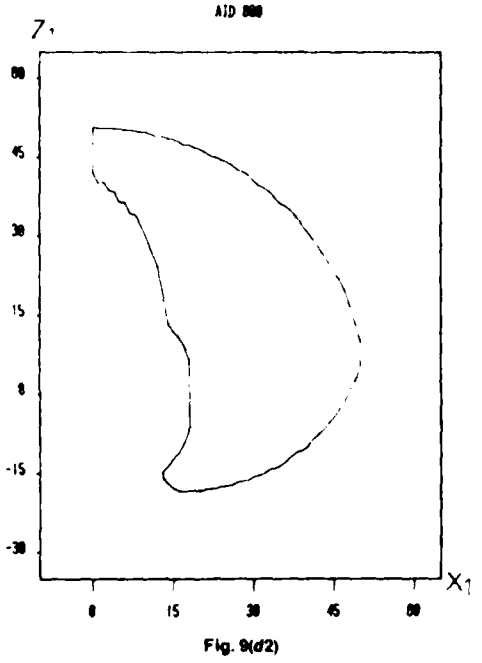


Fig. 9(d2)

Fig. 9(d) Structure and boundary of Automatix AID 800

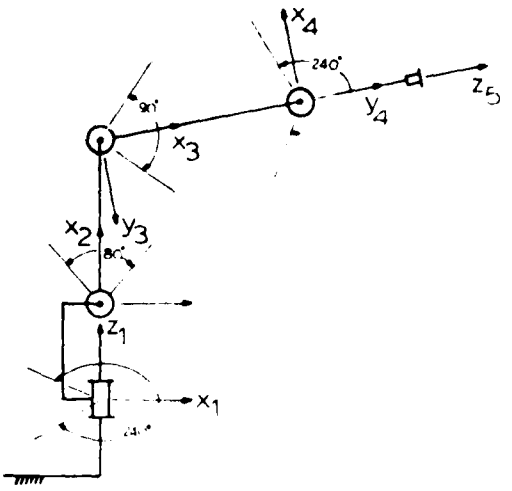


Fig. 9(e1)

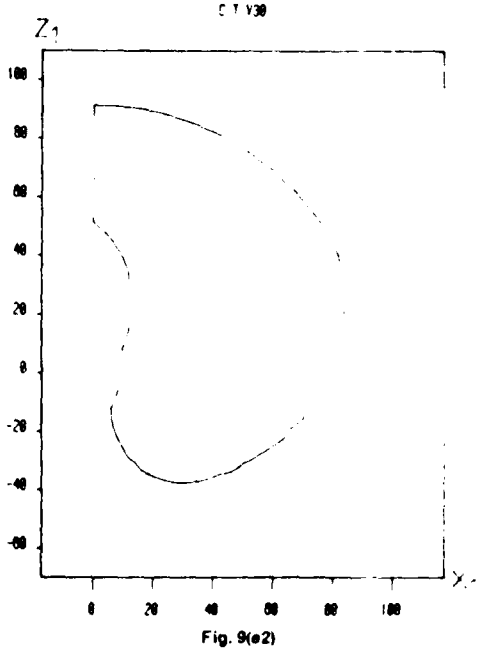


Fig. 9(e2)

Fig. 9(e) Structure and boundary of Cybotech V30

$b_1 = 0$, $b_2 = 0$, $b_3 = 0$, $b_4 = 23.622$, $b_5 = 0$; $\alpha_1 = 90$ deg, $\alpha_2 = 0$ deg, $\alpha_3 = 0$ deg, $\alpha_4 = 90$ deg, $\alpha_5 = 0$ deg, $\beta_1 = -90$ deg, $\beta_2 = 80$ deg, $\beta_3 = -90$ deg; $\theta_1 = 240$ deg, $\theta_2 = 80$ deg, $\theta_3 = 90$ deg, $\theta_4 = 240$ deg, $\theta_5 = 360$ deg. The structure of this manipulator and the boundary of the workspace from KAM are given in Fig. 9(*e*).

It is worth noting that there is a link structure which is common to all the abovementioned manipulators. That is a joint, say joint $k+1$, located on the $Z$ axis of the previous joint, joint $k$ (for instance, joints 1 and 2 of cases 2, 3, 4, and 5; and joints 4 and 5 of case 1 belong to this kind of structure). Consequently, the distance between these two joints with respect to the axis $Z_k$ does not affect the shape and characteristics of workspace $W_k(H)$. Referring to Fig. 10, it is obvious that the distance $d_z$ only affects the relative height of the workspace $W_k(H)$ with respect to the coordinate frame $k$. Therefore $d_z$ is considered to be zero in this comparative study.

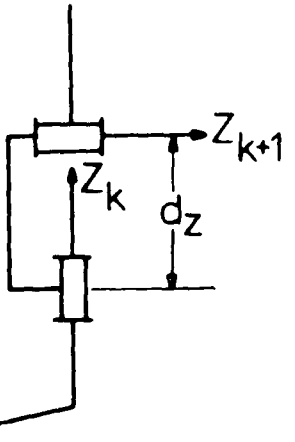


Fig. 10 An illustration of the link structure: the joint $k+1$ is on the axis of joint $k$

The evaluation of these manipulators based on VI and NVI is given in the following table:

**Table 1 Performance evaluation of industrial robots based *on volume index***

| | D.F. | T.Length | Volume | VI | NVI |
|---|---|---|---|---|---|
| PUMA 600 | 6 | 51.0 | 183986 | 1.39 | 0.331 |
| C.M. $T^3$ | 6 | 101.0 | 2295233 | 2.23 | 0.532 |
| Pana Robo | 5 | 59.84 | 355937 | 1.66 | 0.397 |
| AID 800 | 5 | 59.02 | 267350 | 1.30 | 0.310 |
| CT V30 | 5 | 94.49 | 1299251 | 1.54 | 0.368 |

## 7 Conclusion

The result of this investigation has demonstrated that it is possible to analytically evaluate the manipulator workspace and most importantly, it presents a kinematic performance index for manipulators. It is the ratio of the volume of a manipulator's workspace to the cube of its total link length. Based on this index, five commercially available robots can be compared and rated for the first time according to their workspace. This study, it is believed, provides one of the very basic tools necessary for the evaluation of manipulator performance.

## 8 Acknowledgments

The authors are grateful to the Army Research Office for the support of this research through contract DAAG 29-81-K-0016 to Rutgers University. Daniel Yang gratefully acknowledges the support of RCA Laboratories, Princeton, NJ, where he is employed.

## References

1 Yang, D. C. H. and Lee, T. W., "On the Workspace of Mechanical Manipulators," this issue ASME Journal of Mechanisms, Transmissions, and Automation in Design, pp. 62–70.

2 Roth, B., "Performance Evaluation of Manipulators from a Kinematic Viewpoint," NBS Special Publication No. 459: *Performance Evaluation of Programmable Robots and Manipulators*, 1975, pp. 39–61.

3 Uicker, J. J., "Some Unanswered Questions on the Kinematic Analysis of Robots and Manipulators," *Proceedings of the National Science Foundation* Workshop on the Impact on the Academic Community of Required Research Activity for Generalized Robotic Manipulators, University of Florida, Feb. 1978, pp. 198–211.

4 Roth, B., "Kinematic Design For Manipulation," NSF Workshop on the research needed to advance the state of knowledge in Robotics, The University of Rhode Island, April 15–17, 1980, pp. 110–118, NTIS No. PB81 132557.

5 Gupta, K. C., and Roth, B., "Design Considerations for Manipulator Workspace," ASME *Journal of Mechanical Design*, Vol. 104, No. 4, Oct. 1982, pp. 704–712.

6 Kumar, A., and Waldron, K. J., "The Workspace of a Mechanical Manipulator," ASME *Journal of Mechanical Design*, Vol. 103, No. 3, July 1981, pp. 665–672.

7 PUMA 600 Robot, Unimation Inc., Shelter Rock Lane, Danbury, CT 06810.

8 Cincinnati Milacron $T^3$ Robot, Cincinnati Milacron, Cincinnati, Ohio 45209.

9 Arc-Welding Robot: Pana Robo, Matsushita Electric Trading Co., LTD., P.O. Box 288, Osaka, Japan.

10 AID robot, Automatix Inc., 217 Middlesex Turnpike, Burlington, MA 01803.

11 Cybotech V30 Robot, Cybotech Corp., P.O. Box 88514, Indianapolis, IN 46208.

# Robotics Research and Advanced Applications

*presented at*

THE WINTER ANNUAL MEETING OF
THE AMERICAN SOCIETY OF MECHANICAL ENGINEERS
PHOENIX, ARIZONA
NOVEMBER 14-19, 1982

*sponsored by*

THE DYNAMIC SYSTEMS AND CONTROLS DIVISION, ASME

*edited by*

WAYNE J. BOOK
GEORGIA INSTITUTE OF TECHNOLOGY

THE AMERICAN SOCIETY OF MECHANICAL ENGINEERS
United Engineering Center 345 East 47th Street New York, N.Y. 10017

# OPTIMIZATION OF MANIPULATOR WORKSPACE

D. C. H. Yang, Assistant Professor
Department of Mechanics and Structures
UCLA
Los Angeles, California

T. W. Lee, Associate Professor
Department of Mechanical and Aerospace Engineering
Rutgers University
New Brunswick, New Jersey

*ABSTRACT*

This papr presents an analytical and computer-aided procedures on the design of manipulators for optimum workspace. The subject is treated in two parts. In part I, a performance index is derived for evaluating the workspace and determining the dimensions of manipulators. The effects of geometry on the kinematic characteristics of manipulators and the design parameters are investigated. Based on this analysis an algorithm for the design of manipulator workspace is described in the second part. The effects of the design parameters on manipulator workspace are then investigated and design considerations are presented. Using this procedure, the "computer-designed model" is demonstrated, in examples, to be capable of obtaining better workspace than the conventional models available commercially at the present time. In addition, an optimized model of the RRRS robot is found and compared with the proportions of a human arm.

## 1. Introduction

The subject of optimum design of manipulators is an area of practical interest in which little has been done and reported. This is primarily due to the difficulty in establishing performance criteria for robots and manipulators. One way to evaluate performance is from the kinematic viewpoint. For instance, given the kinematic structure of a manipulator, what is its workspace? How can we design the proportions of the structure in order to optimize its workspace?

There have been a number of investigations on manipulator workspace [1-5]. Recently, Yang and Lee [1,2] developed an analytical representation of manipulator workspace and presented the first performance index on a manipulator based on workspace. A computer program called KAM (Kinematic Analysis of Manipulators) was developed which implemented the theories and criteria presented in [1]. For a given manipulator structure, KAM first defines analytically the workspace, then explores the existance of hole and void, outlines the boundary, and finally calculates the total volume of the workspace.

In the present study, a new approach is introduced. An effective algorithm is developed called KADOM which combines the Heuristic Optimization Technique (HOT) with the KAM, to provide a systematic procedure to optimize the manipulator structure based on workspace. Two problems are investigated. The first problem deals with the optimization of the RRRS manipulator, and the second

deals with the optimization of some commercially available robots. A comparative study between the human arm proportions and the optimized RRRS structure is also investigated.

## 2. Manipulator with Revolute Joints

An analytical investigation of manipulator workspace is given by Yang and Lee [1]. The following, taken from [1], represents a description of manipulator geometry and a summary of the results on the analytical representation of workspace.

A manipulator with n unlimited revolute joints in series can be represented schematically, as shown in Fig.1. There are n coordinate frames to specify the configuration. For any coordinate frame, say k, the $Z_k$ axis is always the joint axis and the $X_k$ axis is in the direction of the common normal between axes $Z_k$ and $Z_{k+1}$. The $Z_1$ axis is attached to a fixed frame. The last link, link n, is associated with the hand or the end effector of the manipulator. The link k is connected to joint k. Three parameters are needed to specify the geometrical relation of two consecutive unlimited joints (joint being a capable making a complete rotation). Referring to Fig 2a, these parameters are $a_k$, the common normal between two consecutive axes $Z_k$ and $Z_{k+1}$; $\alpha_k$, the twist angle of these two axes, and $b_k$, the axial offset of joint k+1 on the axis $Z_{k+1}$. For limited revolute joint (joint with physical rotational limit), an additional parameter $\beta_k$, the location angle of link k+1 with respect to link k, is needed as shown in Fig 2b. A position angle $\beta_k$ is defined as the angle between the $X_k$ axis and the $X_{k+1}$ axis while both the link k and the link k+1 being in the mid-range of their joint rotation.

The workspace of a manipulator is defined as the region which can be reached by the center of the manipulator's hand. H, and $W_k(H)$ denotes the workspace generated by the point H, holding the axis k as fixed while all the revolute joints k, k+1, ..., n make rotations.

A general recursive formula for workspace $W_k(H)$ can therefore be formulated as follows.

$$\begin{aligned} x_k &= r_k \cos\vartheta_k \\ y_k &= r_k \sin\vartheta_k \\ z_k &= z_k^* \end{aligned} \tag{1}$$

where $r_k = \sqrt{x_k^{*2} + y_k^{*2}}$ and

$$\begin{bmatrix} x \\ y \\ z \\ \vdots \end{bmatrix}_k^* = [A]_{k+1} \begin{bmatrix} x \\ y \\ z \\ \vdots \end{bmatrix}_{k+1} \tag{2}$$

where $[A]_{k+1}$ denotes the homogeneous transformation which provides the geometrical relationship between two consecutive coordinate frames k+1 and k. Depending upon whether the revolute joint is unlimited or limited, there are different expressions for $[A]_{k+1}$. For unlimited revolute joint, it is given as,

$$[A]_{k+1} = \begin{bmatrix} 1 & 0 & 0 & a_k \\ 0 & \cos\alpha_k & \sin\alpha_k & b_k \sin\alpha_k \\ 0 & -\sin\alpha_k & \cos\alpha_k & b_k \cos\alpha_k \\ 0 & 0 & 0 & \vdots \end{bmatrix} \tag{3}$$

For limited revolute joint [1], we have

$$[A]_{k+1} = \begin{bmatrix} \cos\beta_k & -\sin\beta_k & 0 & a_k \\ \cos\alpha_k \sin\beta_k & \cos\alpha_k \cos\beta_k & \sin\alpha_k & b_k \sin\alpha_k \\ -\sin\alpha_k \sin\beta_k & -\sin\alpha_k \cos\beta_k & \cos\alpha_k & b_k \cos\alpha_k \\ 0 & 0 & 0 & \vdots \end{bmatrix} \tag{4}$$

Having an analytical representation, the boundary and the volume of the

workspace can subsequently be determined by the construction of the cross-secton on $W_k(H)$ cut by the plane $X_k Z_k$ [2]. Mathematically, this cross-section my be expressed as

$$x_k = \pm r_k = f(\vartheta_{k+1}, \vartheta_{k+2}, \ldots, \vartheta_n)$$
$$z_k = z_k' = g(\vartheta_{k+1}, \vartheta_{k+2}, \ldots, \vartheta_n) \qquad (5)$$

Because the $W_k(H)$ is symmetric with respect to the axis $Z_k$, therefore, Eq (5) contains all geomerical information regarding the shape of the workspace. By scanning sequentially the joint angles $\vartheta_n, \vartheta_{n-1}, \ldots, \vartheta_{k+1}$ in Eq (5) according to their rotation limits, at a reasonably small interval, most of points of $W_k(H)$ can thus be obtained.

### 3. A Performance Index Based on Workspace Volume

Given a manipulator we are now capable of evaluating its workspace volume quantitatively. Furthermore, the development of a performance index based on workspace volume is presented [2]. A definite relationship between the volume of workspace and the total length of a manipulator is found. This is given as " For a given manipulator, (i.e. the twist angles, rotation limits, location angles and the proportions of link length are given), the ratio between the volume of the workspace and the cube of the total length is a constant," i.e.,

$$\frac{V}{(l_1+l_2+\ldots+l_{2n})^3} = \frac{V}{L^3} = constant = VI \qquad (6)$$

The notation VI stands for the Volume Index of manipulator workspace, which gives an indication of the effectiveness of link length on the creation of reachable workspace. The index can be normalized by dividing its possible maximum value [2]. Let the total length of a manipulator equal L, the maximum workspace that this manipulator can possibly have is a sphere with radius L and centered at the joint 1. Therefore, the maximum VI a manipulator can possibly have is

$$\frac{4\pi L^3/3}{L^3} = \frac{4\pi}{3} \approx 4.1888 \qquad (7)$$

Using this value as a normalizing factor, a normalized volume index, denoted as NVI, can be obtained, and its value is between 0 to 1.

Five commerically available manipulators, namely PUMA 600 (Unimation Inc.), $T^3$ (Cincinnati Milacron), Pana-robo (Matsushita LTD), AID 800 (Automatix Inc.), and V30 (Cybotech Corp.) are evaluated based on VI and NVI. The results are given in the following table.

| — | dof | T Length | Volume | VI | NVI |
|---|---|---|---|---|---|
| PUMA 600 | 6 | 51.0 | 163986 | 1.39 | 0.331 |
| CM $T^3$ | 6 | 101.0 | 2295233 | 2.23 | 0.532 |
| Pana-Robo | 5 | 59.84 | 355937 | 1.66 | 0.397 |
| AID 800 | 5 | 59.02 | 267350 | 1.30 | 0.310 |
| CT V30 | 5 | 94.49 | 1399251 | 1.54 | 0.368 |

*Table 1 Performance evaluation of industrial robots based on Volume Index*

### 4. Optimization Algorithm

In the previous sections a performance index based on manipulator workspace, NVI, is presented. This index provides an objective function in the optimization of manipulator design. In this section a computer program named Kinematic Analysis and Design of Manipulators (KADOM) is developed which searches for the optimal design of manipulators based on the volume of workspace. It combines the Heuristic optimization Technique (HOT) of Lee and Freudenstein [6] and the manipulator analysis program (KAM) of Lee and Yang [2]. The design parameters for the optimization are those basic kinematical properties of a manipulator which includes the common normals, twist angles, offset distances, and location angles among joints. The objective function of the optimization is the normalized volume index (NVI). The remainder of this secton gives a brief introduction to the Heuristic OPtimization Technique.

The heuristic algorithm, H O T. program, developed especially for the purpose of mechanism optimization, differ from most of the conventional optimization methods in many ways. First, it is a non-numerical, effective discrete optimization technique, so designed to integrated well with the mathematical structure of a general mechanism design problem, which is usually characterized by long iterative procedures and nonlinearities. The algorithm is built with the special capability of by-passing the usual obstacles of nonlinearity encountered in mechanism design problems. The method is therefore not an exhaustive search method; rather, it is a systematic, intelligent guessing technique and is probabilistic in nature. Secondly, the algorithm is very efficient and simple to use. The attainability of a solution does not depend on continuity and differentiability, and it is essentially independent of the starting point of the search.

The method is a discrete one and therefore requires the discretization of a problem. In a mechanical system, this would naturally refer to the conversion of a continuous parameter variation into a discrete variation, that is, the conversion of the solution space into a finite number of states of combinations, called the selection space. The parameters are allowed only on certain prescribed discrete values or states, chosen in accordance with what seem to be reasonable ranges or proportions. This is advantageous, since the design engineer generally knows reasonable upper and lower bounds on key parameters. The selection space can e represented mathematically by a matrix (NxL) in which there are N rows and L columns corresponding to N discrete states of each of the L design parameters.

To apply the H O T. algorithm, the designer needs to supply only two subroutines: one defines the feasibility criteria, the other specifies the objective function. Once the designer selects N and provides the lower and upper bounds of each pamaters, the solution space is defined by the input selection-space matrix, (*NxL*). The algorithm then generates as many locally optimum solutions as computation time permits. The best of the locally optimum solutions may be chosen as a solution to the problem. The underlying principles of the combinatorial heuristics are given in [6,7].

In the following sections, KADOM is employed to optimize two special manipulator structures and some commercially available robots to demonstrate its capability and potential.

## 5. Optimum Design of Manipulators with RRRS Structure

Two manipulator structures which are commonly adopted in industry are optimized through the KADOM program. The result is then compared with an analytical solution. It is clear that usually for a limited revolute joint, the greater the rotation range the larger the corresponding workspace. It is therefore reasonable to consider all revolute joints be unlimited in a general study.

The first structure, as shown in Fig 3, is a manipulator with six revolute joints, and with design parameters: $a_4 = 0$, $a_5 = 0$, $a_6 = 0$, $b_1 = 0$, $b_2 = 0$, $b_3 = 0$, $b_4 = 0$, $b_5 = 0$, $b_6 = 0$, $\alpha_1 = 90°$, $\alpha_2 = 0°$, $\alpha_3 = 0°$, $\alpha_4 = 90°$, $\alpha_5 = 90°$, $\alpha_6 = 0°$, and $a_1$, $a_2$ and $a_3$ are dimensions not equal to zero. If the axes of the last three joints intersect at one point, say point H, and two pairs of them are orthogonal, then these three revolute joints are equvalent to a spherical joint at point H. Therefore, this manipulator will have a RRRS structure, as shown in Fig 4. The advantage of this structure is that its entire workspace is primary workspace [3,5]. The primary workspace is that every point in this workspace is reachable by the manipulator s hand from all directions. Contrarily, a workspace contains points which can not be reached by the manipulator hand from all directions is named as secondary workspace.

Referring to Fig 4, let design parameters $a_1$, $a_2$ and $a_3$ be variables, and all other part of the structure be fixed, the task is then to find the optimal proportions between $a_1$, $a_2$ and $a_3$ in order to obtain maximum workspace volume. The result from KADOM shows that the optimal proportion between $a_1$, $a_2$ and $a_3$ is 0 1 1, and the manipulator corresponding to this proportion is given in Fig 5.

The second structure studied in this section is shown in Fig 6. The design parameters of this manipulator are $a_1 = 0$, $a_3 = 0$, $a_4 = 0$, $a_5 = 0$, $a_6 = 0$, $b_2 = 0$, $b_4 = 0$, $b_5 = 0$, $b_6 = 0$, $\alpha_1 = 90°$, $\alpha_2 = 0°$, $\alpha_3 = 90°$, $\alpha_4 = 90°$, $\alpha_5 = 90°$, $\alpha_6 = 0°$, and $a_2$, $b_1$, and $b_3$ are dimensions not equal to zero. This is also a RRRS structure. The parameters for optimization are now $b_1$, $a_2$ and $b_3$. The result from KADOV shows the optimal proportion among $b_1$, $a_2$ and $b_3$ is also 0 : 1 : 1. The result is exactly the same as the previous example.

The question then raised is whether the structure obtained from KADOV is really a global optimal or just a local extreme. In order to answer it, the following concept is introduced. Referring to Fig 7, the workspace created by this manipulator equals a sphere with radius L and centered at joint 1. Because the hand of a manipulator can reach any point beyond its total link length, therefore, theoretically, the possible maximum workspace will be the sphere with radius the total link length and centered at the first joint, joint 1. This proves that a RRRS manipulator with $a_1 = 0$, $a_2 = L/2$, $a_3 = L/2$, $b_1 = 0$, $b_2 = 0$, $b_3 = 0$, and $\alpha_1 = 90°$, $\alpha_2 = 0°$, $\alpha_3 = 0°$, is the global optimum based on the volume of workspace. It is worth noting that the structure will remain the same when the design parameters $a_3 = 0$, $b_3 = L/2$ and $\alpha_3 = 90°$.

The optimal design of the RRRS manipulator discussed in this section is kinematically equivalent to a TRS structure (here T denotes a hooke joint). Since $a_1 = b_1 = 0$ and $\alpha_1 = 90°$, the first two revolute joints can therefore be replaced by a hooke joint.

## 6. Comparative Study of the Proportions of Human Arms with the Optimum RRRS Structure

Perhaps it is interesting and noteworthy to consider for a moment the structure of human arms. Is the human arm an "optimal design"? Is there any similarity between a human arm and the optimal RRRS structure discussed previously? There are apparent differences between a human arm and the optimal TRS structure. For instance, usually anatomical joints of a human arm have six degrees of freedom [8], they are ""designed" for two arms cooperation, and all anatomical joints are limited, etc. However, kinematically the dimensions are surprisingly close.

The dimensional comparison between an average human arm [9] and the optimal TRS manipulator is shown in Fig 8. The ratio between the upper arm and the sorearm is 1:0.82. However, if the size 9of the hand is included in the consideration and the grasp position of the hand is estimated as $0.27 * \cos 30°$ (referring to Fig 8 where 0.27 is the average length proportion of the back of a hand and 30° refers to the average grasp angle) then the proportion between the upper arm and the distance between elbow and grasp point becomes 1 : 1.05. This ratio is very close to the dimensions of the optimal TRS structure which equals 1:1. This finding is interesting. It suggests a surther analytical investigation of the subject of the workspace problem of human arms.

## 7. A Dimensional Study of Some Commercially Available Robots

In this section, numerical experiments of the link lengths of five commercially available robots discused in Chapter V are performed using the KADOV program. The purpose is to search for the best proportions of the link lengths for the existion robots. To avoid major redesign, all non-zero link lengths are allowed too vary only within ± 20% of their original length, and other design parameters, such as twist angles, location angles and zero length links remain unchanged.

The results of the optimal proportions found by KADOV are shown in Table 2. From a comparison of the NVI values between the original and new designs it is concluded that for a small variation of link length, the workspace volume for the robots, C.M. $T^3$, Puma-Robo and AID 800, do not show significant increase. However, for PUMA 600 and CT V30 robots, relatively large improvement can be achieved. Particularly in the PUMA 600 robot., a better ratio of volume to link length is obtained by reducing both design parameters $b_1$ and $b_2$, where $b_1$ and $b_2$ are offset distances of link 1 and 2 respectively. The parameter $b_1$ ($b_1$ = 10 in.), which is commonly referred to as the shoulder of the PUMA arm, actually does not contribute much to the volume of the workspace. By eliminating the shoulder, the total link length in this case would be about 20% less than the ori-

ginal one. However, the workspace volume would be only 0.8% less and the NVI value wouldbe nearly 9.1% better than the original one (Table 3). There may be reasons to include the shoulder in the PUMA structure. However, from a kinematic point of view, eliminating the shoulder would optimize the workspace.

| Robot | Volume (in **3) | Link Length (in.) | NVI |
|---|---|---|---|
| PUMA 600 | 1.83986 | 51.0 | 0.331 |
| PUMA 600 (No shoulder) | 1.82549 | 41.0 | 0.632 |
| C.M. T3 | 2.295233 | 101.0 | 0.532 |

*Table 3. A comparison of PUMA 600 Robot with and without shoulder*

## 8. Conclusion

An approach for the optimum design of manipulators based on workspace is presented and a computer code KADOM is developed. Some practical examples are given and an interesting comparative stuky with the human arm proportions is provided. The study deals with only one of many objectives for the optimization of manipulator design. Some other important engineering aspects such as the accessibility (dexterity) of the workspace, dynamics and controls, etc. need to be considered also. It is hope, however, this study provides a basic approach and an algorithm for further research in this area.

## 9. Acknowledgements

The authors are grateful to the Army Research Office for the support of this research through Contract DAAG 29-81-K-0016 to Rutgers University. Daniel Yang gratefully acknowledges the support of RCA Laboratories, Princeton, N.J. where he was employed.

## 10. References

[1] Yang, D.C.H. and Lee, T.W., "On the Workspace of Mechanical Manipulators," to appear in ASME J. of Mechanical Design.

[2] Lee, T.W. and Yang, D.C.H., "On the Evaluation of Manipulator Workspace," to appear in ASME J. of Mechanical Design.

[3] Gupta, K.C. and Roth, B., "Design Considerations for Manipulator Workspace," ASME Paper No.81-DET-79, 1981, to appear in ASME J. of Mechanical Design.

[4] Kumar, A. and Waldron, K.J., "The Workspace of a Mechanical Manipulator," ASME J. of Mechanical Design, Vol. 103, No.3, July 1981, pp.665-627.

[5] Kumar, A. and Waldron, K.J., "The Dextrous Workspace," ASME Paper No.80-DET-108, 1980.

[6] Lee, T.W. and Freudenstein, F., "Heuristic Combinatorial Optimization in the Kinematic Design of Mechanisms, Part I & II, Theory and Applications," ASME J. of Engr. for Industry, Vol.98, Nov. 1976, pp.1277-1284.

[7] Langrana, N.A. and Lee, T.W., "Analysis of Dynamic Systems Using Heuristic Optimization," ASME J. of Dynamic Syst., Measurement and Control, March 1980, pp.35-40.

[8] Kinzel, G.L., "Reduction of INstrumented Linkage Data for Simple Anatomical Joint Models," ASME J. of Mechanical Design, Vol.104, Jan. 1982, pp.218-226.

[9] Drillis, R., Contini, R. and Bluestein, M., "Body Segment Parameters: A Survey of Measurement Techniques," Artificial Limbs, Vol.2, No.1, 1964, pp.44-66.

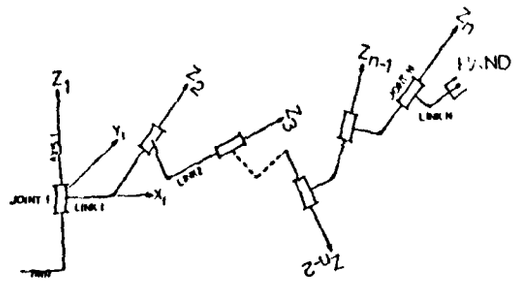


*Fig 1 A manipulator with n revolute joints in series*

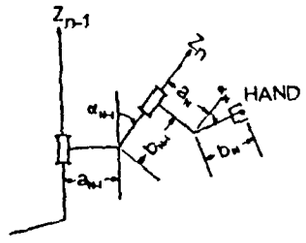


*Fig 2a Geometrical relationship between unlimited revolute joints n−1 and n*

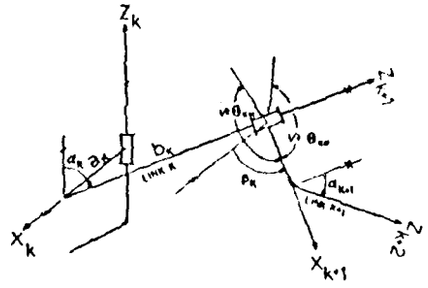


*Fig 2b Geometrical relationship between limited revolute joints k and k+1*

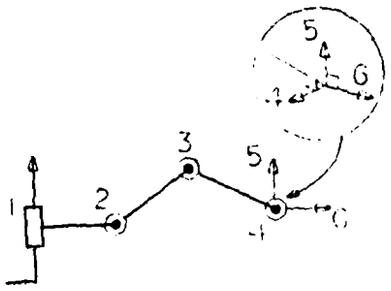


*Fig 3 A commonly adopted 6R robotic structure*

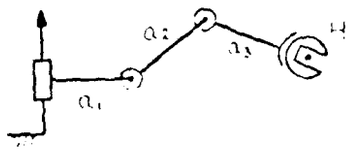


*Fig 4 The equivalent RRRS structure*

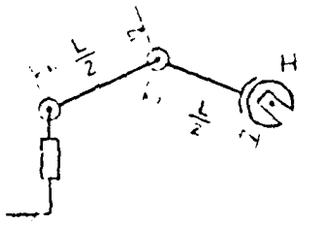


*Fig 5 The RRRS configuration with optimum workspace*

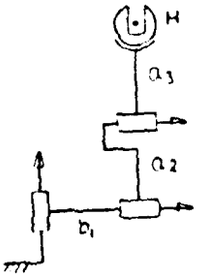


*Fig 6 Another commonly adopted RRRS robotic structure*

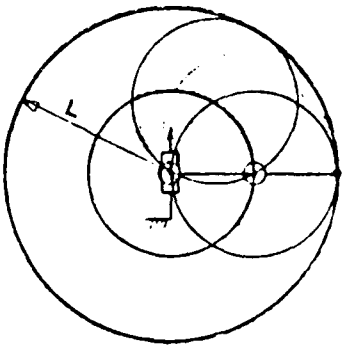


Fig 7 *The workspace of the optimum TRS structure is a sphere with radius L and centered at joint 1.*

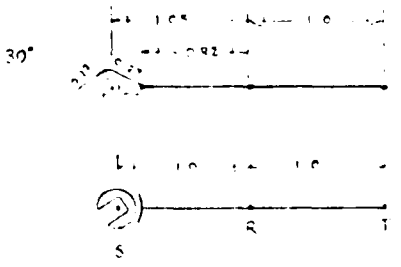


Fig 8 *A dimensional comparison between a human arm and the optimum TRS robot arm.*

Table 2

Improvement of workspace volume based on small changes in the link length proportions

| Robot | Design Parameters | Length Proportions | WVI | % Improvement of WVI |
|---|---|---|---|---|
| PUMA 600 | $b_1$, $a_2$, $b_2$, $b_3$, $b_5$ | 0.56:1:0.22:0.94:0.11 | 0.331 * | 52% |
| | | 0.37:1:0.05:0.91:0.14 | 0.503 ** | |
| C.M. $T^3$ | $a_2$, $a_3$, $a_4$, $b_5$ | 1:1:0.2:0.33 | 0.532 * | 2.4% |
| | | 0.92:1:0.26:0.4 | 0.545 ** | |
| Pana-Robo | $a_2$, $a_3$, $b_4$ | 0.75:1:0.15 | 0.397 * | 5.5% |
| | | 0.67:1:0.19 | 0.419 ** | |
| AID 800 | $a_2$, $a_3$, $b_4$ | 0.75:1:0.13 | 0.313 * | 6.4% |
| | | 0.58:1:0.14 | 0.333 ** | |
| CT V30 | $a_2$, $a_3$, $b_4$ | 0.8:1:0.6 | 0.368 * | 20% |
| | | 0.51:1:0.67 | 0.443 ** | |

* original design
** KADOM's results

THE AMERICAN SOCIETY OF MECHANICAL ENGINEERS
345 E. 47 St., New York, N.Y. 10017



83-DET-35

**D. C. H. Yang**
Assistant Professor
Department of Mechanics and Structures
University of California
Los Angeles, Calif. 90024
Assoc. Mem. ASME

**T. W. Lee**
Associate Professor
Department of Mechanical and Aerospace Engineering
Rutgers University
New Brunswick, N.J. 08903
Mem. ASME

# Feasibility Study of a Platform Type of Robotic Manipulators from a Kinematic Viewpoint[1]

*This paper presents a theoretical investigation on the feasibility of using a platform mechanism as a robotic manipulator. The existence of this type of closed-loop kinematic chain is first investigated via a kinematic number synthesis. A displacement analysis then follows, which gives inverse control equations in terms of motion and design parameters, using the [4 × 4] matrix method. Basic kinematic characteristics and limitations, such as the extreme ranges of motion and rotatability as well as workspace are investigated.*

## 1 Introduction

Traditionally, robot arms are anthropomorphic open chain mechanisms. This type of manipulator usually has longer reach, larger workspace, and more dextrous maneuverability then closed kinematic chain mechanisms. However, there are also disadvantages. The cantilever-type of structure for the open manipulators inherently has poor stiffness and therefore has undesirable dynamic characteristics, especially at high speed and high loading operating conditions. In addition, with the exception of certain configurations [1], the problem of solving the inverse function in manipulator control is always difficult.

Perhaps there is a possible alternative design for manipulators using the closed kinematic chain such as the Steward platform [2] and others [3]. This would be particularly feasible in applications where dynamic loading is severe and yet the demand on workspace and maneuverability is low. For instance, it could be used for development of an "intelligent" multi-degree-of-freedom positioner which would be versatile in many uses such as high precision machining, welding, painting, and many military applications.

There have not been many investigations of manipulators with closed kinematic chain on the record. The Steward platform [2] which is constructed by connecting two plates to six adjustable legs and is a six-degree-of-freedom 6-SPS platform mechanism. (S and P denote the spherical and prismatic joints, respectively), was originally designed as an aircraft simulator, and was also suggested for the applications of machine tool, space vehicle simulator, transfer machine, etc. Later, Hoffman and McKinnon [4] tried to simulate the aircraft motion via this type platform by applying an SAP IV finite element program. McCallion and Truong [5] used this device as an automatic assembly table. They described [5] the mechanical hardware and the problem of path synthesis was also investigated. In this book, Hunt [2] adopted the Steward platform as a mechanism for a robotic arm. Following that idea, Fichter and McDowell [6] presented a review and some preliminary design concepts on this type of manipulator. Recently, Hunt [7] undertook a systematic study on the so-called parallel-actuated robotic arms, in which many possible applicable in-parallel structures were reviewed and which included the Steward platform.

Despite its potential usefulness, this class of closed kinematic-chain manipulators does have physical limitations which it is important to recognize so that kinematic synthesis methods may be developed with these constraints and characteristics in mind. It is, therefore, necessary to gain deeper understanding of this type of mechanism and to obtain some design and application guidelines. Consequently, a feasibility study of this mechanism in the light of its potential application as a robotic positioner is both important and of practical interest.

The purpose of this investigation is to develop analytical methods and computer-aided procedures capable of analyzing the basic kinematic characteristics of the platform mechanism, such as the extreme ranges of motion as well as workspace. In particular, the objectives are: 1) to perform a number synthesis on the existence of a single (or many) platform structure(s) which is suitable for functioning as a robotic positioner; 2) to formulate an analytical model for this class of mechanism and to provide a displacement analysis including the solvability of its inverse control equations; 3) to analytically formulate the physical constraints of this mechanism, such as the rotatability of legs and ball-and-socket joints; and 4) ultimately to investigate the workspace and maneuverability of the mechanism.

Although previous investigations on this mechanism have included certain aspects of the problems mentioned here, such as mobility [2, 6, 7] and displacement relationship [2, 5, 6], a

[1] Based in part on the dissertation of the first author in partial fulfillment of the requirement for the Doctor of Philosophy in the School of Engineering, Rutgers University, New Brunswick, N.J., 1982.

Contributed by the Design Automation Committee for presentation at the *Design and Production Engineering Technical Conference*, Dearborn, Mich., September 11-14, 1983, of THE AMERICAN SOCIETY OF MECHANICAL ENGINEERS. Manuscript received at ASME Headquarters, June 10, 1983. Paper No. 83-DET-35.

Copies will be available until June 1984.

is believed that a comprehensive investigation of these subjects, especially from the consideration of physical constraints and workspace using analytical and computer-aided means, is much needed and the effort would certainly be noteworthy.

## 2 Number Synthesis

It is well known that a mechanism which is used as a general robotic manipulator should have six or more controllable degrees-of-freedom (d.o.f.). For manipulators with articulated configuration, in many cases of simple applications, the number of controllable d.o.f. can be less than six if cost and simplicity are a consideration. The Steward platform [2] has six extensible links and has six degrees-of-freedom. There are a few basic questions one can ask regarding the platform mechanism or similar mechanisms. For instance, why is it necessary to have six connecting legs, or equivalently, what is the relationship between the number of legs and the number of controllable d.o.f. of this type of mechanism? Is it possible to introduce more legs into the mechanism and yet still maintain six controllable d.o.f.? What is the possibility of having controllable d.o.f. with more than or less than six? This section of the paper deals with these problems.

**2.1 n-SS Platform.** We begin with a discussion of the *n*-SS platform as shown in Fig. 1. Since the connecting joints between the legs and the plates of the platform are ball joints and the d.o.f. of ball joints are not controllable, we therefore first determine the number "*n*" so that the mechanism would have zero degrees-of-freedom.

A general form of the degree-of-freedom equation for both planar and spatial mechanisms can be written as follows [8]:

$$F = \lambda(l - j - 1) + \sum f_i - I_d \qquad (1)$$

where

- $F$ = the effective degree-of-freedom of the assembly or mechanism,
- $\lambda$ = the degree-of-freedom of the space in which the mechanism operates (for spatial motion $\lambda = 6$, and for plane motion and motion on a surface $\lambda = 3$),
- $l$ = number of links,
- $j$ = number of joints,
- $f_i$ = degree-of-freedom of $i$th joint,
- $I_d$ = idle or passive degree-of-freedom.

It is known that generally there are special geometrical conditions which need to be taken into consideration in the determination of the d.o.f. on spatial mechanisms. Special cases are often associated with parallel, intersecting, or perpendicular joint axis. Consequently, the modifying term $I_d$ takes care of this idle d.o.f.

Referring to Fig. 1, we have $\lambda = 6$, $l = n + 2$ (including $n$ legs and 2 plates), $j = 2n$ and $f_i = 3$ (for each ball joint, the d.o.f. is 3). It is also noted that each pair of ball-and-socket joints which associate with the same leg can turn with respect to the axis of the leg freely; therefore, this is an idle d.o.f. which does not contribute to the mobility of the mechanism itself. Consequently, only five of the six d.o.f. of the ball joint pairs associate with the mobility of the mechanism. We have, therefore, $I_d = n$ which corresponds to the number of SS pairs or the number of legs. Using equation (1),

$$F = 6 - n \qquad (2)$$

Equation (2) shows that when $n$ equals six, the d.o.f. of the platform equals zero, i.e., the 6-SS platform is a structure. When $n$ is less than six, we will have $(6 - n)$ uncontrollable d.o.f. and when $n$ is greater than six, the structure is overconstrained.

**2.2 n-SPS (or n-SCS) Mechanism.** Since the 6-SS mechanism is a rigid structure, it is not manipulatable. In order to provide controlled motion on this mechanism, a cylindrical (or prismatic) joint is added to each leg. Referring to Fig. 2, each of these cylindrical joints can be controlled by a motor or linear actuator, and the length of each leg can then be adjusted individually. A cylindrical joint has two degrees-of-freedom. However, using a similar argument as in the previous section, only the translational degree of freedom affects the mobility of the mechanism and the rotational freedom is a redundant one. This suggests that the SCS leg in this particular case is kinematically equivalent to an SPS leg, where S and P represent the cylindrical and prismatic pairs, respe-

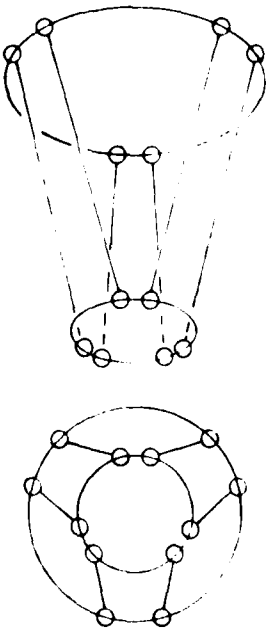

Fig. 1 A 6-SS platform mechanism

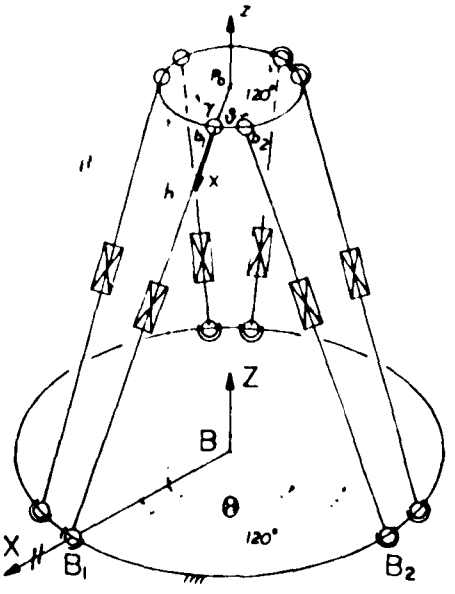


Fig. 2 A 6-SPS platform mechanism and its design parameters

tively. For a $n$-SPS platform, we have $l = 2n + 2$ and $j = 3n$, therefore,

$$F = 6[(2n + 2) - 3n - 1] + \sum_{2n} 3 + \sum_{n} 1 - n$$

$$6n + 6 + 6n + n - n - 6 \tag{3}$$

The result from equation (3) shows that a $n$-SPS platform always has six d.o.f. and among them $n$ d.o.f. are controllable. If $n$ is less than six, there exists $(6 - n)$ uncontrollable d.o.f. If $n$ is greater than six, there exists $(n - 6)$ wasted controls which are needed to compensate the overconstraints as can be seen in equation (2). Only when $n$ equals six, there are six controllable d.o.f. Therefore the 6-SPS platform is the only mechanism of its type which can be used as a general robotic manipulator.

Another interesting question could be asked. Can a platform with $n$-SPS* $(6 - n)$-SS structure serve as a $n$ d.o.f. manipulator for $n$ less than 6? Theoretically the answer is yes, but practically it is no. The reason, which will become clear later, is that in specifying the leg lengths, the problem of identifying the corresponding position (both location and orientation) of the top plate would become a very difficult task; on the other hand, if the desired position of the top plate is prescribed, it is rather easy to obtain the corresponding leg lengths. However, this is under the condition that there must be six adjustable legs. We may therefore conclude that it is impractical for the platform type of manipulators with d.o.f. less than six, whereas, in contrast, the situation often is allowed in the articulated type of manipulators.

## 3 Displacement Analysis and Controllability

It was concluded in the previous section that the 6-SPS platform which has six controllable degrees of freedom is potentially useful as a general manipulating device. The purpose of this section is to present a mathematical analysis of the input-output relationship and subsequently to demonstrate the controllability of the mechanism.

**3.1 Displacement Analysis.** To analytically model a 6-SPS platform (Fig. 2), we shall at the beginning define the controllable elements and the desired outputs of the mechanism. First, let the controlling of the position of the center point, $p$, of the top plate be the desired objective, i.e., the point represents the hand (or the end effector) of the manipulator. Second, let each of the legs of the platform be adjustable and individually controllable, i.e., for each prismatic joint (or cylindrical joint), there associates with it a servomotor (or the like). Third, for simplicity and without losing generality, let both the top and the bottom plates be circular in shape with the top one assumed to be movable and the bottom one fixed and having its center at $B$. Furthermore, let the distribution of each pair of ball joints on the bottom plate be symmetrical with respect to each of the three radii located at 120 deg apart from one another on the plate. The ball joints on the top plate have similar arrangements. The platform mechanism is then an octahedron. Denoting $R$ and $r$ as the radii of the bottom and the top plates, respectively; $l_1$ through $l_6$ as the leg lengths; $l_0$ as the nominal length for all legs; and $h$ as the distance between the two plates when all leg lengths are equal to the nominal length $l_0$.

To give an analytical representation of the kinematics of the 6-SPS mechanism, the fixed Cartesian coordinate frame is selected at point $B$ with the $Z$ axis pointing vertically upward and the X axis passing through point $B_1$. The locations of the ball joints on the fixed bottom plate can then be established.

$$\begin{aligned}
B_1 &= [R,0,0]^t \\
B_2 &= [RC_{\theta_1}, RS_{\theta_1}, 0]^t \\
B_3 &= [RC_{120-\theta_1}, RS_{120-\theta_1}, 0]^t \\
B_4 &= [RC_{120+\theta_2}, RS_{120+\theta_2}, 0]^t \\
B_5 &= [RC_{240-\theta_2}, RS_{240-\theta_2}, 0]^t \\
B_6 &= [RC_{240+\theta_3}, RS_{240+\theta_3}, 0]^t
\end{aligned} \tag{4}$$

where $\theta$ represents the angle between ball joints $B_1$ and $B_2$, $B_3$ and $B_4$, and $B_5$ and $B_6$; and $C_{\theta_i}$ and $S_{\theta_i}$ represent the cos $\theta_i$ and sin $\theta_i$, respectively.

Similarly, let a moving Cartesian coordinate frame $[T]$ be associated with the top plate, having its origin at the point $p$, its $z$ axis normal to the plate, and the $x$ axis passing through the point $b_1$. Therefore, the relative locations of the ball joints, $b_i$'s, with respect to the moving frame are

$$\begin{aligned}
b_1 &= [r,0,0]^t \\
b_2 &= [rC_{\theta_1}, rS_{\theta_1}, 0]^t \\
b_3 &= [rC_{120-\theta_1}, rS_{120-\theta_1}, 0]^t \\
b_4 &= [rC_{120+\theta_2}, rS_{120+\theta_2}, 0]^t \\
b_5 &= [rC_{240-\theta_2}, rS_{240-\theta_2}, 0]^t \\
b_6 &= [rC_{240+\theta_3}, rS_{240+\theta_3}, 0]^t
\end{aligned} \tag{5}$$

where $\theta$ denotes the angle between ball joints $b_1$ and $b_2$, $b_3$ and $b_4$, and $b_5$ and $b_6$.

Let the point $p_0$ and the Cartesian coordinate $[T]_{p_0}$ be the position of $p$ when the top plate is at its original (the nominal) position as shown in Fig. 4. The geometrical relationship between the coordinate frame $[T]$ and the fixed coordinate frame $[B]$ can be represented by a $4 \times 4$ homogeneous transformation, and it is as follows:

$$[T]_{p_0} = \begin{bmatrix} \cos\gamma & \sin\gamma & 0 & 0 \\ \sin\gamma & \cos\gamma & 0 & 0 \\ 0 & 0 & 1 & h \\ 0 & 0 & 0 & 1 \end{bmatrix} \tag{6}$$

where $\gamma = \theta_1 - \theta_2$.

Now assume the center of the top plate moves away from its nominal position $p_0$ to a new desired position $p$ and have the transformation $[T]_p$ with respect to the fixed coordinate system $[B]$. Let

$$[T]_p = \begin{bmatrix} d_{11} & d_{12} & d_{13} & x_p \\ d_{21} & d_{22} & d_{23} & y_p \\ d_{31} & d_{32} & d_{33} & z_p \\ 0 & 0 & 0 & 1 \end{bmatrix} \tag{7}$$

Where the $(x_p, y_p, z_p)$ are the Cartesian locations of the point $p$, and $(d_{11}, d_{21}, d_{31})$, $(d_{12}, d_{22}, d_{32})$, and $(d_{13}, d_{23}, d_{33})$ are direction cosines of the axes $x$, $y$, and $z$ with respect to the fixed coordinate $[B]$, correspondingly. Therefore, the location of each ball joint on the moving top plate with respect to the coordinate frame $[B]$ can be obtained from equations (5) and (7), and they are

$$\begin{bmatrix} x \\ y \\ z \\ 1 \end{bmatrix}_{b_i} = [T]_p \begin{bmatrix} r \\ 0 \\ 0 \\ 1 \end{bmatrix} = \begin{bmatrix} d_{11}r + x_p \\ d_{21}r + y_p \\ d_{31}r + z_p \\ 1 \end{bmatrix} \tag{8a}$$

$$\begin{bmatrix} x \\ y \\ z \\ 1 \end{bmatrix} = [T]_p \begin{bmatrix} rC_{\theta} \\ rS_{\theta} \\ 0 \\ 1 \end{bmatrix} = \begin{bmatrix} d_{11}rC_{\theta} + d_{12}rS_{\theta} + x_p \\ d_{21}rC_{\theta} + d_{22}rS_{\theta} + y_p \\ d_{31}rC_{\theta} + d_{32}rS_{\theta} + z_p \\ 1 \end{bmatrix} \quad (8b)$$

$$\begin{bmatrix} x \\ y \\ z \\ 1 \end{bmatrix} = [T]_p \begin{bmatrix} rC_{120} \\ rS_{120} \\ 0 \\ 1 \end{bmatrix} = \begin{bmatrix} d_{11}rC_{120} + d_{12}rS_{120} + x_p \\ d_{21}rC_{120} + d_{22}rS_{120} + y_p \\ d_{31}rC_{120} + d_{32}rS_{120} + z_p \\ 1 \end{bmatrix} \quad (8c)$$

$$\begin{bmatrix} x \\ y \\ z \\ 1 \end{bmatrix} = [T]_p \begin{bmatrix} rC_{120+\theta} \\ rC_{120+\theta} \\ 0 \\ 1 \end{bmatrix} = \begin{bmatrix} d_{11}rC_{120+\theta} + d_{12}rS_{120+\theta} + x_p \\ d_{21}rC_{120+\theta} + d_{22}rS_{120+\theta} + y_p \\ d_{31}rC_{120+\theta} + d_{32}rS_{120+\theta} + z_p \\ 1 \end{bmatrix} \quad (8d)$$

$$\begin{bmatrix} x \\ y \\ z \\ 1 \end{bmatrix} = [T]_p \begin{bmatrix} rC_{240} \\ rS_{240} \\ 0 \\ 1 \end{bmatrix} = \begin{bmatrix} d_{11}rC_{240} + d_{12}rS_{240} + x_p \\ d_{21}rC_{240} + d_{22}rS_{240} + y_p \\ d_{31}rC_{240} + d_{32}rS_{240} + z_p \\ 1 \end{bmatrix} \quad (8e)$$

$$\begin{bmatrix} x \\ y \\ z \\ 1 \end{bmatrix} = [T]_p \begin{bmatrix} rC_{240+\theta} \\ rS_{240+\theta} \\ 0 \\ 1 \end{bmatrix} = \begin{bmatrix} d_{11}rC_{240+\theta} + d_{12}rS_{240+\theta} + x_p \\ d_{21}rC_{240+\theta} + d_{22}rS_{240+\theta} + y_p \\ d_{31}rC_{240+\theta} + d_{32}rS_{240+\theta} + z_p \\ 1 \end{bmatrix} \quad (8f)$$

**3.2 Controllability.** The controllability of a manipulator could be qualitatively assessed by the degree of difficulty involved in the solution of the inverse kinematic problem which is the determination of the corresponding coordinates of the manipulator by prescribing the desired position of the end-effector in the fixed Cartesian coordinate frame. For manipulators with articulated configuration, the corresponding coordinates are the rotational angles of the revolute joints. For manipulators with platform configuration, they are the corresponding leg lengths.

Let the desired position of the end-effector of a platform manipulator be $[T]_p$. The absolute locations of the ball joint $b_i$'s on the top plate can be derived from equation (8). The required leg lengths can be obtained by calculating the distance between each corresponding pair of ball joints, $b_i$'s and $B_i$'s. From equations (4) and (8), we have

$$l_1^2 = (d_{11}r + x_p - k)^2 + (d_{21}r + y_p)^2 + (d_{31}r + z_p)^2 \quad (9a)$$

$$l_2^2 = (d_{11}rC_{\theta} + d_{12}rS_{\theta} + x_p - RC_{\theta})^2 + (d_{21}rC_{\theta} + d_{22}rS_{\theta} + y_p - RS_{\theta})^2 + (d_{31}rC_{\theta} + d_{32}rS_{\theta} + z_p)^2 \quad (9b)$$

$$l_3^2 = (d_{11}rC_{120+\theta} + d_{12}rS_{120} + x_p - RC_{120})^2 + (d_{21}rC_{120+\theta} + d_{22}rS_{120+\theta} + y_p - RS_{120+\theta})^2 + (d_{31}rC_{120+\theta} + d_{32}rS_{120+\theta} + z_p)^2 \quad (9c)$$

$$l_4^2 = (d_{11}rC_{120+\theta} + d_{12}rS_{120+\theta} + x_p - RC_{120+\theta})^2 + (d_{21}rC_{120+\theta} + d_{22}rS_{120+\theta} + y_p - RS_{240+\theta})^2 + (d_{31}rC_{120+\theta} + d_{32}rS_{240+\theta} + z_p)^2 \quad (9d)$$

$$l_5^2 = (d_{11}rC_{240} + d_{12}rS_{240} + x_p - RC_{240})^2 + (d_{21}rC_{240} + d_{22}rS_{240} + y_p - RS_{240})^2 + (d_{31}rC_{240} + d_{32}rS_{240} + z_p)^2 \quad (9e)$$

$$l_6^2 = (d_{11}rC_{240+\theta} + d_{12}rS_{240+\theta} + x_p - RC_{240+\theta})^2 + (d_{21}rC_{240+\theta} + d_{22}rS_{240+\theta} + y_p - RS_{240+\theta})^2 + (d_{31}rC_{240+\theta} + d_{32}rS_{240+\theta} + z_p)^2 \quad (9f)$$

Equation (9) represents a set of explicit input-output equations of the 6-SPS platform mechanism. For a prescribed end-effector position, the corresponding leg lengths can be readily obtained; however, the direct kinematic control problem is a rather difficult task since it involves the solution of a set of highly nonlinear simultaneous equations. The situation is found to be exactly contrary to the case of a robot with open kinematic chain.

## 4 Rotability of Ball-and-Socket Joints

A ball joint, theoretically, can move freely with respect to all three Cartesian axes. In practice, however, this is not true. The motion of the ball joint is always restricted because of its physical dimensions. A ball joint usually includes three parts: the ball head, socket, and the connecting leg. Referring to Fig. 3, let the radii of the ball head and the connecting leg be $R$ and $d/2$, respectively. To physically hold the ball head in the socket, the holding width $e$, as shown in the figure, must be greater than zero. Let $\alpha$ denote the rotation angle of the joint on the $XZ$ plane, the rotational limits of the angle $\alpha$ can be determined as follows:

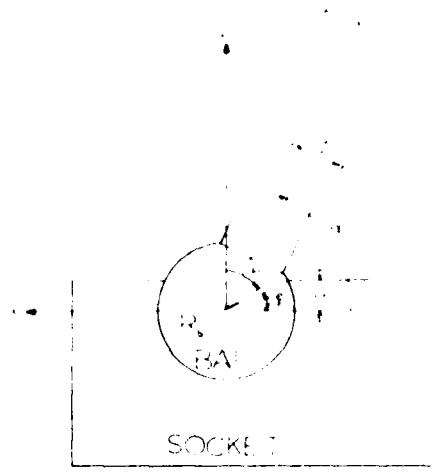


Fig. 3 *The principal cross-section of a ball-and-socket joint*

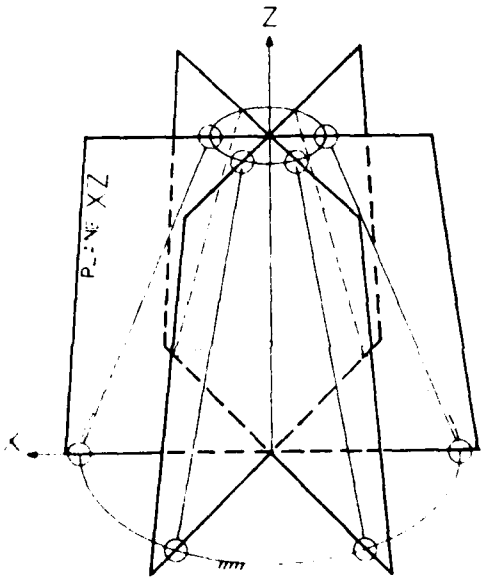


Fig. 4 A 6-SPS platform mechanism with ball joints evenly distributed

$$\xi = \sin^{-1}\frac{e}{R_b} \tag{10}$$

$$\rho = \left(\frac{\pi}{2} - \alpha\right) + \sin^{-1}\frac{\frac{d}{2}}{R_b} \tag{11}$$

For free rotation, $\rho$ should be less than or equal to $\pi/2 - \xi$; from equations (10) and (11), we have

$$\left(\frac{\pi}{2} - \alpha\right) + \sin^{-1}\frac{\frac{d}{2}}{R_b} \le \frac{\pi}{2} - \sin^{-1}\frac{e}{R_b}$$

or

$$\alpha \ge \sin^{-1}\frac{d}{2R_b} + \sin^{-1}\frac{e}{R_b} \tag{12}$$

The complete rotational range of $\alpha$ on the $XZ$ plane is, therefore,

$$\pi - \left(\sin^{-1}\frac{d}{2R_b} + \sin^{-1}\frac{e}{R_b}\right) \ge \alpha \ge \sin^{-1}\frac{d}{2R_b} + \sin^{-1}\frac{e}{R_b} \tag{13}$$

Equation (13) is useful. It represents the physical constraints of ball joints and provides the practical design guidelines for these joints.

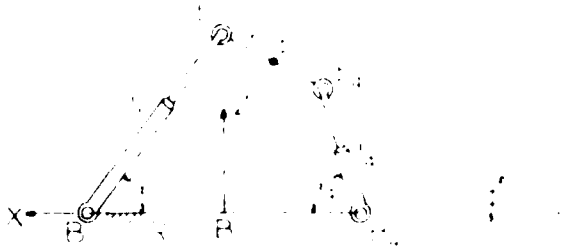

Fig. 5 A planar four-bar mechanism with two adjustable links

## 5 Workspace and Maneuverability

The problem of analyzing the shape of the workspace of a 6-SPS platform manipulator is a rather difficult one. In addition to the inherent complexity in dealing with spatial geometry, the mechanism is characterized by its multiloop structure and its displacement behavior which involves a set of highly nonlinear simultaneous equations. For simplicity, consider, therefore, a special case[2] in which all ball joints are evenly distributed along the peripheries of both the bottom and the top plates (i.e., both angles $\Omega$ and $\theta$ are of 60 deg) as shown in Fig. 4. The basic approach employed is to investigate the workspace of this mechanism from its cross section on three particular planes. Referring to Fig. 4, these are the $XZ$ plane which contain the ball joints $B_1b_1b_2B_2$ and the planes formed by turning the $XZ$ plane with respect to the $Z$ axis with an angle of 60 and 120 deg, respectively. To further simplify the problem we consider a special case wherein the motion of the top plate of the mechanism is allowed only to rotate with respect to the $Y$ axis, i.e., the rotatability with both $X$ and $Z$ axes is restricted. The problem, therefore, is reduced to finding the reachable space of the center point, $p$, on the coupler of a planar 4-bar mechanism (as shown in Fig. 5) with adjustable link lengths, $l_3$ and $l_4$, subjected to various constraints such as the extreme limits of all legs and the rotatability of all joints. In the following the displacement equation of this planar adjustable 4-bar mechanism is first derived. The interference conditions are then considered.

**5.1 Displacement Analysis of A Planar 4-Bar With Adjustable Links.** Figure 5 shows a planar 4-bar mechanism with adjustable link lengths, $l_3$ and $l_4$. A coordinate frame, $[B]$, is located at the point $B$ with $Z$ axis pointing vertically upward and the $X$ axis pointing horizontally left. $B_1$, $b_1$, $b_2$ and $B_2$ represent four ball joints. The link lengths of the coupler and the fixed link are the diameters of the top and the bottom plates, i.e., $2r$ and $2R$, respectively. The coordinates of the fixed ball joints, $B_1$ and $B_2$, on the bottom plate are $(R,0)$ and $(-R,0)$, respectively, and coordinate of the moving ball joint $b_1$ on the top plate is $(R - l_1\cos\alpha_1, l_1\sin\alpha_1)$. Specifying values of the input parameters $\alpha_1$, $l_3$, and $l_4$, then the outputs which are the corresponding coordinates of points $b_4$ and $p$, and the corresponding angles of $\varphi$ and $\alpha_4$ can be found. It is our purpose to derive the closed form input-output displacement relationship.

Equating the distance between the two ball joints, $b_2$ and $b_4$, to the length of the coupler, $2r$, we have

[2] It is worth noting here that there exists a special singularity condition for this evenly distributed case, for which the degrees-of-freedom analysis presented in Section 2 is not applicable. It is the position that all legs are equal and both the bottom and the top plates are parallel. This condition is similar to the well-known case of the 4-bar parallelogram with an additional link of equal crank length connecting the middle points of the coupler and the frame. In this case of special proportions of links, the general degrees-of-freedom equation usually does not apply.

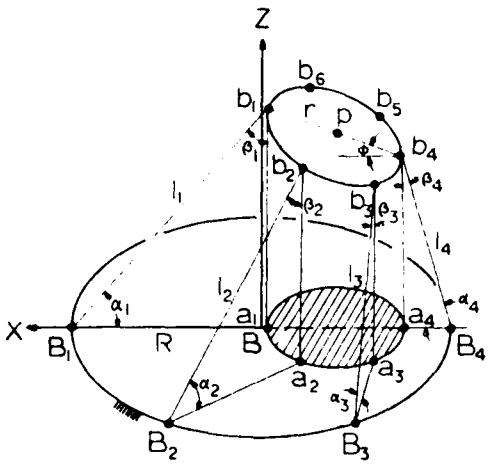


Fig. 6 Geometrical parameters of the platform mechanism

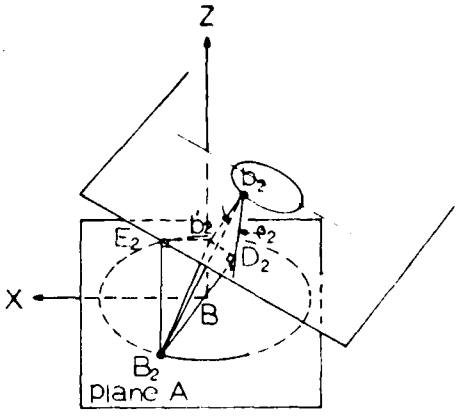


Fig. 7 A method to determine the distance $B_2D_2$

$$\bar{b}_4b_1^2 = (x_4 - R + l_1C_{\alpha_1})^2 + (z_4 - l_1S_{\alpha_1})^2 = 4r^2 \quad (14)$$

Equating the distance between the ball joints $b_4$ and $B_4$ to link length $l_4$, we obtain

$$(x_4 + R)^2 + (z_4)^2 = l_4^2 \quad (15)$$

Subtracting equation (14) from equation (15), we have

$$z_4 = \frac{l_1^2 + l_4^2 - 4r^2 - 2R_1C_{\alpha_1}}{2l_1S_{\alpha_1}} - \frac{2R - l_1C_{\alpha_1}}{l_1S_{\alpha_1}}x_4 \quad (16)$$

Let

$$P = \frac{l_1^2 + l_4^2 - 4r^2 - 2Rl_1C_{\alpha_1}}{2l_1S_{\alpha_1}} \quad (17)$$

and

$$Q = \frac{2R - l_1C_{\alpha_1}}{l_1S_{\alpha_1}} \quad (18)$$

then we have

$$z_4 = P - Qx_4 \quad (19)$$

the coordinates of point $b_4(x_4,z_4)$ can be solved explicitly and

$$x_4 = \frac{-(R - PQ) \pm \sqrt{(R - PQ)^2 - (1 + Q^2)(P^2 + R^2 - l_4^2)}}{(1 + Q^2)} \quad (20)$$

Subsequently, the coordinate of the point $p(x_p,z_p)$ is given by

$$\left.\begin{aligned} x_p &= \frac{x_4 + R - l_1C_{\alpha_1}}{2} \\ &\text{and} \\ z_p &= \frac{z_4 + l_1S_{\alpha_1}}{2} \end{aligned}\right\} \quad (21)$$

The corresponding angle $\alpha_4$ can be obtained from

$$\alpha_4 = \tan^{-1}\frac{z_4}{x_4 + R} \quad (22)$$

The corresponding tilt angle of the top plate, $\phi$, is given by

$$\phi = \tan^{-1}\frac{l_1S_{\alpha_1} - z_4}{R - l_1C_{\alpha_1} - x_4} \quad (23)$$

Equations (19)-(23) represent a set of explicit equations defining the displacement of a planar 4-bar with adjustable link lengths $l_1$ and $l_4$.

**5.2 Motion of the Top Plate With Constraints on the Extensibility of Legs.** For a 6-SPS mechanism, each leg is limited by its extreme extensible length, i.e., $l_{i,\min} \le l_i \le l_{i,\max}$. Assuming all legs have the same limits of length, the motion of the point $p$ (equation (21)) is then constrained by the extreme lengths of the legs, $b_1B_1$,$b_2B_2$,$b_3B_3$ and $b_4B_4$, i.e.,

$$l_{\min} \le l_1, l_2, l_3, l_4 \le l_{\max} \quad (24)$$

Since the top plate is symmetric with respect to the $XZ$ plane, the legs $b_5B_5$ and $b_6B_6$ are mirror images of the legs $b_3B_3$ and $b_2B_2$, respectively. Therefore they are not included in this discussion.

For a given leg length $l_1$ and $l_4$, it is necessary to know whether the corresponding leg lengths $l_2$ and $l_3$ are within the extensible limits. Referring to Fig. 6 we have,

$$l_i^2 = \bar{B}_ia_i^2 + b_ia_i^2 \quad (25)$$

where the $a$ points represent the projections of the $b$ points on the $XY$ plane. The distances $B_ia_i^2$ and $B_ia_i^2$ are given as follows:

$$\begin{aligned} \bar{B}_1a_1^2 &= (R - 2rC_\phi - x_4)^2 \\ \bar{B}_2a_2^2 &= (0.5R - 1.5rC_\phi - x_4)^2 + (RS_{60} - rS_{60})^2 \\ \bar{B}_3a_3^2 &= (-0.5 - 0.5rC_\phi - x_4)^2 + (RS_{60} - rS_{60})^2 \\ \bar{B}_4a_4^2 &= (-R - x_4)^2 \end{aligned} \quad (26)$$

and

$$\begin{aligned} b_1a_1 &= z_4 + 2rS_\phi \\ b_2a_2 &= z_4 + 1.5rS_\phi \\ b_3a_3 &= z_4 + 0.5rS_\phi \\ \bar{b}_4a_4 &= z_4 \end{aligned} \quad (27)$$

where the tilt angle, $\phi$, of the top plate is given by equation (23). The desired corresponding leg lengths, $l_2$ and $l_3$, can then be calculated from equations (25)-(27).

**5.3 Rotatability of the Ball Joint on the Bottom Plate.** The workspace of the center point, $p$, of the top plate (equation (21)) is the space bounded by all the constraints attributed to the ball joints, as given by equation (13), in addition to the constraints due to the interferences of links. The corresponding angles of the ball joints on the bottom plate can easily be derived in terms of the known parameters, $\alpha_1$, $l_1$, and $l_4$. Referring to Fig. 6,

$$\alpha_i = \tan^{-1}\frac{b_ia_i}{B_ia_i} \quad (28)$$

where the angle $\alpha_4$ can be calculated from equation (22).

**5.4 Rotatability of the Ball Joint on the Top Plate.**

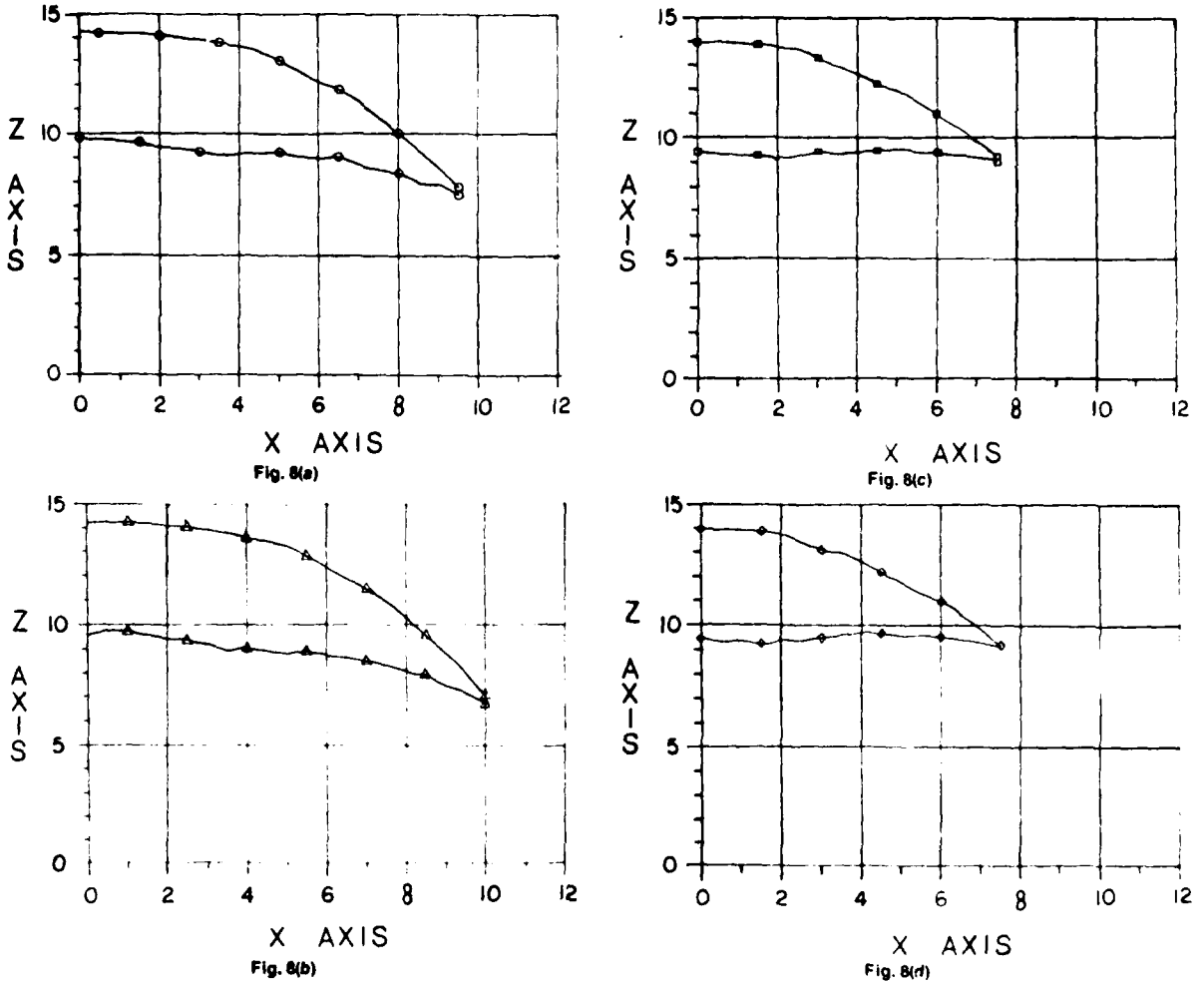


Fig. 8(a) Fig. 8(c)

Fig. 8(b) Fig. 8(d)

Fig. 8 The boundaries of workspace on the XZ plane

Referring to Fig. 6, the position angles of the ball joints on the top plate, i.e., the $\beta$'s, are the angles formed by each of the legs with the top plate. We have

$$\beta_1 = \alpha_1 + \phi$$

$$\beta_4 = ABS(\alpha_4 - \phi) \tag{29}$$

where $\phi$ is the tilt angle of the top plate. The position angles $\beta_2$ and $\beta_3$, however, do not have a simple relationship. The derivation of them first requires determining the distance between the ball joint $B_2$ (or $B_3$) and the plane containing the top plate, i.e., $B_2D_2$ (or $B_3D_3$) (Fig. 7). One way to find the distance $B_2D_2$ is to analyze the geometrical relationship of the project of the triangle $B_2b_2D_2$ on the plane, denoted as plane $A$, which is parallel to the $XZ$ plane and contains the line $B_2D_2$. The distance $B_2D_2$ can therefore be obtained from

$$B_2D_2 = B_2b_2' \sin\lambda \tag{30}$$

where

$$\bar{B}_2b_2' = \sqrt{\bar{B}_2'E_2^2 + \bar{b}_2E_2^2} = \sqrt{(z_4 + 1.5rS)^2 + (1.5rC + x_4 - 0.5R)^2}$$

and

$$\lambda = \pi - ABS\left[\tan^{-1}\frac{\bar{B}_2E_2}{\bar{b}_2'E_2}\right] + \pi$$

The position angle of the ball joint $b_2$ can then be calculated from

$$\beta_2 = \sin^{-1}\frac{B_2D_2}{l_2} \tag{31}$$

Similarly, the equation of the position angle of the ball joint $b_3$ can be obtained as follows:

$$\beta_3 = \sin^{-1}\frac{B_3D_3}{l_3} \tag{32}$$

where

$$\bar{B}_3D_3 = \sqrt{(z_4 + 0.5rS_\phi)^2 + (0.5rC_\phi + x_4 + 0.5R)^2}\sin\lambda$$

Having analytically developed the necessary kinematic relationship of this special 6-SPS mechanism, we are now in a position to develop an algorithm to numerically outline the reachable boundary of the mechanism on the $XZ$ plane.

## 6 A Numerical Algorithm

An algorithm for detecting the reachable boundary of the 6-SPS mechanism on the $XZ$ plane is presented as follows:

1. (*a*) Scan the angle $\alpha_1$ within the physical rotational limits of the given ball joint.
   (*b*) Scan the lengths $l_1$ and $l_4$ within the specified extensible limits of the legs.

2. For a particular set of $\alpha_1$, $l_1$, and $l_4$:
   (*a*) – Check the limits of the corresponding leg lengths $l_2$ and $l_3$,
   (*b*) – Check the limits of the corresponding ball joint angles, i.e., $\alpha$'s and $\beta$'s.

   If out of the range then go to Step 1, otherwise continue.
3. Calculate the desired position of the center of the top plate, i.e., $p(x_p, z_p)$ and record the extremes on a data base. Go to Step 1 until all scanning processes are complete.
4. Outline the workspace boundary from the recorded extremes.

A computer program which is based on the analytical formulations and criteria derived in this investigation, and which is written in FORTRAN, is developed. Given a 6-SPS platform with evenly distributed ball joints, the program outlines the boundary of the workspace on the $XZ$ plane of the center point of the top plate. Inputs of this program are: the width of the hold of the ball joints ($e$), the radius of the ball head ($R_h$), the diameter of the connecting legs ($d$), the extensible limits of the connecting legs ($l_{max}$ and $l_{min}$), the radii of the top and the bottom plates ($r$ and $R$), and the leg lengths $l_1$, $l_4$. The scanning interval of the joint angle $\alpha_i$ needs to be specified.

Four practical examples are given to demonstrate the range of the workspace and the maneuverability of this type of mechanisms.

*Case 1*: A platform mechanism has the following design parameters: $l_{max} = 15''$, $l_{min} = 10''$, $r = 2$, $R = 5''$, and the ball joint dimensions are $e = 0.1''$, $R_h = 0.5''$, and $d = 0.2''$. Using the algorithm, the cross section of the workspace on the $XZ$ plane is shown in Fig. 8(*a*).

*Case 2*: All design parameters remain the same as Case 1 except the width of the hold and the diameter of the connecting leg of the ball joint are reduced to half of the original values, i.e., $e = 0.05''$ and $d = 0.1''$. The cross section of the workspace on the $XZ$ plane is given in Fig. 8(*b*).

*Case 3*: All design parameters are the same as Case 2 except the radius of the top plate is reduced to half of its original value, i.e., $r = 1''$. The cross section of the workspace on the $XZ$ plane is given in Fig. 8(*c*).

*Case 4*: Repeat the same design parameters as Case 1 except the radius of the top plate is now reduced to half of its original size, i.e., $r = 1''$. The cross-section of the workspace on the $XZ$ plane is given in Fig. 8(*d*).

## 7 Conclusion

This paper provides a basic kinematic investigation on platform type manipulators. It is found that the 6-SPS, or the Steward platform appears to be the only mechanism of its type that can possibly be adopted as a general maneuverable device. The analytical model and inverse control equations are derived. Although the complexity of the model, and the solvability of the inverse equations are more favorable as compared to a six-joint articulated robot, the workspace and the maneuverability seem to be relatively restricted. This is expected and due mainly to the multiloop structure and the interference between the ball joints, legs, and plates. Unlike some previous studies [5, 6] in which ball-and-socket joints of the platform mechanism were replaced by two revolute joints in their analytical model, this investigation considers the rotatability of the ball joints and its formulation is believed to be of new and practical significance. The result of the investigation on workspace, performed in a special case, represents an upper bound for our design considerations.

It should be noted, however, that this investigation only concerns a kinematic viewpoint. An investigation of the statics and dynamics of this mechanism, which are currently underway, is essential for the practical application of this platform. The result of this research, it is hoped, will contribute toward a basic understanding of the limitations as well as the potential usefulness of this type of manipulator.

## 8 Acknowledgments

The authors are grateful to the Army Research Office and the National Science Foundation for the support of this research through contract DAAG29-81-K-0016 and grant MEA-80-06783, respectively, to Rutgers University.

## References

1 Pieper, D. L., "The Kinematics of Manipulators Under Computer Control," *Stanford Artificial Intelligence Laboratory*, Stanford University, AIM 72, Oct. 1968.

2 Stewart, D., "A Platform with Six Degrees of Freedom," *Proceedings of the Institution of Mechanical Engineers*, Vol. 180, Part 1, No. 15, 1965-66, pp. 371-386.

3 Hunt, K. H., *Kinematic Geometry of Mechanisms*, Oxford University Press, London, 1978.

4 Hoffman, R., and McKinnon, M. C., "Vibration Modes of an Aircraft Simulator Motion System," *Proceedings of the Fifth World Congress for the Theory of Machines and Mechanisms*, an ASME Publication, 1979, pp. 603-606.

5 McCallion, H., and Truong, P. D., "The Analysis of a Six-Degree-of-Freedom Work Station for Mechanised Assembly," *Proceedings of the Fifth World Congress for the Theory of Machines and Mechanisms*, an ASME Publication, 1979, pp. 611-616.

6 Fichter, E. F., and McDowell, E. D., "A Novel Design for a Robot Arm," *Advances in Computer Technology*, an ASME Publication, 1980, pp. 250-256.

7 Hunt, K. H., "Structural Kinematics of In-Parallel-Actuated Robot Arms," ASME Paper 82-DET-105, 1982.

8 Freudenstein, F., and Maki, E. R., "The Creation of Mechanisms According to Kinematic Structure and Function," *Environment and Planning B*, Vol. 6, 1979, pp. 375-391.


F
3